



THE HONG KONG  
POLYTECHNIC UNIVERSITY

香港理工大學

Pao Yue-kong Library

包玉剛圖書館

---

## Copyright Undertaking

This thesis is protected by copyright, with all rights reserved.

**By reading and using the thesis, the reader understands and agrees to the following terms:**

1. The reader will abide by the rules and legal ordinances governing copyright regarding the use of the thesis.
2. The reader will use the thesis for the purpose of research or private study only and not for distribution or further reproduction or any other purpose.
3. The reader agrees to indemnify and hold the University harmless from and against any loss, damage, cost, liability or expenses arising from copyright infringement or unauthorized usage.

If you have reasons to believe that any materials in this thesis are deemed not suitable to be distributed in this form, or a copyright owner having difficulty with the material being included in our database, please contact [lbsys@polyu.edu.hk](mailto:lbsys@polyu.edu.hk) providing details. The Library will look into your claim and consider taking remedial action upon receipt of the written requests.

*The Hong Kong Polytechnic University*  
*Department of Electronic and Information Engineering*

**Analysis and Processing of Nonlinear Time Series**  
**— from Speech to Neurophysiological Signals**

Junfeng Sun

A thesis submitted in partial fulfillment of the requirements for  
the degree of Doctor of Philosophy

September 2008

## CERTIFICATE OF ORIGINALITY

I hereby declare that this thesis is my own work and that, to the best of my knowledge and belief, it reproduces no material previously published or written, nor material that has been accepted for the award of any other degree of diploma, except where due acknowledgement has been made in the text.

\_\_\_\_\_ (Signed)

Junfeng Sun (Name of Student)

To my parents

# Abstract

*Abstract of the thesis entitled “Analysis and processing of nonlinear time series — from speech to neurophysiological signals”*

submitted by Mr. Junfeng Sun for *the degree of Doctor of Philosophy at The Hong Kong Polytechnic University in September 2008*

Chief supervisor: Dr Michael Small

This thesis presents new methods of nonlinear signal analysis and processing and their applications. In particular, these methods are inspired by multiple disciplines (nonlinear time series analysis, signal processing, chaos theory, and circular statistics), and applied to analyze, characterize, and process complicated observed signals such as speech signals, laser data, EEG data, and those measured from coupled chaotic systems. Three topics, which are different but related to each other, have been studied.

The first topic is noise reduction for chaotic time series and its application in speech enhancement. The local projection (LP) method is powerful in reducing white noise for chaotic time series. But for the case with coloured noise, LP is no longer effective. By investigating the energy distributions of coloured noise and chaotic time series in the local phase space reconstructed by time delay embedding, a two-step extension of the LP method is proposed. Experimental results show that this extension can reduce coloured noise for chaotic time series effectively. Further, this extension is adapted to enhance speech signals which are contaminated by environmental noise. Comparison shows that this scheme is

comparable to the state-of-art algorithms of speech enhancement.

The second topic is time-frequency analysis. First, the reference phase point and its neighbours in the phase space reconstructed by time delay embedding are shown to cover data segments with similar waveform. To exploit the redundant information possessed by the neighbors, a neighbourhood-based spectral estimator is proposed for chaotic flow. With this estimator, the theory of time delay embedding is bridged to the frequency domain. Then time-frequency analysis with the spectral estimator is performed for chaotic time series. It is shown that the hidden frequency of chaotic systems can be detected by this method reliably and noisy chaotic time series can be distinguished from colored noise which has similar spectra by their different ridge patterns in the time-frequency plane.

The last topic is synchronization analysis. Synchronization is a cooperative behaviour by which coupled systems evolve with the same rhythm. It can help to understand the underlying mechanism and gain new applications such as providing clinical evidence. Our contributions include four aspects. First, a neighbourhood-based method is proposed to estimate instantaneous phase (IP) in the phase space reconstructed by time delay embedding. Simulations show that this method is robust to noise and can avoid overestimation of the degree of phase synchronization (PS). Second, several definitions of IP are revisited and further unified into a framework which defines IP by combining the Hilbert transform with specific filter. Third, an analytical study of the effect of noise in IP estimation and PS detection is performed. The distribution of IP error induced by noise is shown to be a scale mixture of normal distribution. Fourth, a band-weighted synchronization index is proposed based on the PS index in each frequency band specified by a bank of filter. It is tested by toy models and further applied to EEG signals, yielding positive results

# Publications

## Journal papers

1. J. Zhou, X. Xu, J. Zhang, **J. Sun**, M. Small, and J. Lu, “Generating an assortative network with a given degree distribution,” *International Journal of Bifurcations and Chaos* (2008), *in press*.
2. J. Zhang, **J. Sun**, X. Luo, K. Zhang, T. Nakamura, and M. Small, “Characterizing pseudoperiodic time series through complex network approach,” *Physica D* 237 (2008) 2856-2865.
3. M. Small, X. Xu, J. Zhou, J. Zhang, **J. Sun**, and J. Lu, “Generating scale-free networks with high assortativity but are not small world,” *Physical Review E* 77 (2008) 066112.
4. **J. Sun**, J. Zhang, J. Zhou, X. Xu, and M. Small, “Detecting phase synchronization in noisy data from coupled chaotic oscillators,” *Physical Review E* 77 (2008) 046213.
5. **J. Sun**, J. Zhang, and M. Small, “Extension of the local subspace method to enhancement of speech with colored noise,” *Signal Processing* 88 (2008) 1881-1888.
6. Y. Zhao, **J. Sun**, and M. Small, “Evidence consistent with deterministic chaos in human cardiac data,” *International Journal of Bifurcations and Chaos* 18 (1) (2008) 141-160.
7. **J. Sun**, Y. Zhao, J. Zhang, X. Luo, and M. Small, “Reducing coloured noise for chaotic time series in the local phase space,” *Physical Review E*

76 (2007) 026211.

8. **J. Sun**, Y. Zhao, T. Nakamura, and M. Small, “From phase space to frequency domain: A time-frequency analysis for chaotic time series,” *Physical Review E* 76 (2007) 016220.
9. J. Zhang, X.D. Luo, T. Nakamura, **J. Sun**, M. Small, “Detecting temporal and spatial correlations in pseudo-periodic time series,” *Physical Review E* 75 (2007) 016218

## Papers submitted

1. **J. Sun**, N. Zheng, and M. Small, “On relationship between instantaneous frequency and Time-frequency Analysis,” (2008) *submitted*.
2. J. Zhang, K. Zhang, J. Feng, **J. Sun**, X. Xu, M. Small, “Pseudoperiodic time series: dynamics and synchrony through dimension reduction,” (2008) *submitted*.
3. Y. Zhao, G. Zhang, **J. Sun**, and M. Small, “Distribution Criterion for Large Multilayer Neural Networks with Application of Chaotic Attractors Modeling,” (2007) *submitted*.
4. Two papers about the results presented in Chapter 6 are *in preparation*.

## Conference papers

1. **J. Sun**, J. Zhang and M. Small, “A band-weighted method to detect phase synchronization in EEG,” (abstract) *10th Experimental Chaos Conference*, (Catania, Italy, 3-6 June 2008).
2. **J. Sun** and M. Small, “A Time-Frequency method for Chaotic Flow,” *International Symposium on Nonlinear Theory and its Applications* (Institute of Electronics, Information and Communication Engineers; Vancouver, Canada, 16-19 September 2007).

3. J. Zhang, **J. Sun**, and M. Small, “Nonlinear Time Series Analysis of Single-scroll Chua circuit,” *2007 China symposium on circuits and systems (CSCAS2007)*, Guang Zhou, China, 15-17 June 2007 (in Chinese).
4. **J. Sun** and M. Small, “A local subspace method to reduce colored noise for chaotic time series,” (detailed abstract) *The Third Shanghai International Symposium on Nonlinear Sciences and Applications (Shanghai NSA’07)*, (Shanghai Society for Nonlinear Science, Shanghai, China, 6-10 June 2007).



# Acknowledgements

My sincere appreciation goes to my chief supervisor Michael Small for his valuable advice, patient guidance, and generous support which made this study possible. He has frequently given me insightful suggestions, stimulated my research interesting, and inspired me with new ideas. He has arranged weekly meeting and built a comfortable and harmonious atmosphere in our lab. All these let me can advance my research with pleasure. I would also like to thank my Co-supervisor Chi Kong Tse, who has made great efforts in providing various chances for us to communicate and exchange ideas with researchers outside. He has also arranged outings for us, which made our life colorful. I must say that I really enjoyed my research life in the past three years.

I own multiple thanks to Jie Zhang for the cooperation and valuable discussions on research, for his help and the happiness he ever brought to me (playing badminton together, humor in talking, and so on). I thank Qingfeng Zhou for his kind help in my living and valuable discussions on my research. He is such a warmhearted person who is always ready to help others. I thank Tomomichi Nakanura for his suggestions which help me much in revising my research papers. I give my thanks to Xiaodong Luo, Yi Zhao, and Xiaoke Xu for their cooperation and valuable discussions on research. I would like to thank Rongtao Xu, David Walker, Cristian Carmeli, Jin Zhou, Xiumin Li, Xia Zheng, Sufen Chen, Xi Chen, Yuehui Huang, Xiaohui Qu, and Alan Lun who are in our research group for their support in the past years.

I give my special thanks to Yi Yun and Qiongyan Wang. Yi Yun, my old classmate and my present roommate, helped me much at the begging I arrived

in Hong Kong and is always ready to give me help whenever I need. Qiongyan Wang, my old classmate, has generously offered me her warmhearted help and given me courage when I was involved in a tough situation. Without her encouragement, I cannot overcome the difficulty so quickly. Wenfeng Guo, Delong Huang, Guixiang Lei, Jie Zhang and Qingfeng Zhou again, are all deserved my sincere appreciation for their special help in that difficult time.

I gratefully acknowledge the Research Committee of The Hong Kong Polytechnic University for the financial support during the entire period of my candidature.

Last, but far from least, I would like to thank my parents and my elder brother for their love and care over the years, for their persistent support, encouragement, and understanding. I would like to say that what I am doing means so much more because of you.

# Contents

<b>Abstract</b>	<b>i</b>
<b>List of Publications</b>	<b>iii</b>
<b>Acknowledgements</b>	<b>vii</b>
<b>Abbreviations</b>	<b>xx</b>
<b>1 Introduction</b>	<b>1</b>
1.1 Motivation and objectives . . . . .	1
1.2 Outline of the thesis . . . . .	5
<b>2 The background</b>	<b>9</b>
2.1 Nonlinear time series analysis . . . . .	9
2.1.1 Time delay embedding . . . . .	9
2.1.2 State recurrence . . . . .	11
2.2 Noise reduction for chaotic time series . . . . .	13
2.2.1 The locally linear model . . . . .	13
2.2.2 The local projection method . . . . .	14

2.3	Spectrum estimation and time-frequency analysis . . . . .	16
2.3.1	Spectrum estimation . . . . .	16
2.3.2	Time-frequency analysis . . . . .	19
2.4	Synchronization analysis . . . . .	20
2.4.1	Synchronization definition . . . . .	20
2.4.2	Phase synchronization . . . . .	21
2.4.3	Physical conditions for instantaneous phase definition . . . . .	23
<b>3</b>	<b>Reducing noise in the local phase space</b>	<b>25</b>
3.1	Introduction . . . . .	26
3.1.1	Noise reduction in the local phase space . . . . .	26
3.1.2	Speech enhancement with the local projection method . . . . .	27
3.2	A two-step extension of the local projection method . . . . .	28
3.3	Applications to noisy chaotic time series . . . . .	32
3.4	Applications to noisy speech signals . . . . .	36
3.4.1	Application to vowels . . . . .	36
3.4.2	Enhancement of continuous speech . . . . .	39
3.4.2.1	The speech database . . . . .	39
3.4.2.2	Implementation . . . . .	39
3.4.2.3	Results . . . . .	41
3.5	Discussion and conclusion . . . . .	44
<b>4</b>	<b>Neighborhood-based time-frequency analysis</b>	<b>49</b>
4.1	Introduction . . . . .	49

4.2	Neighborhood-based spectrum estimation . . . . .	51
4.2.1	State recurrences and nearest neighbors . . . . .	51
4.2.2	A neighborhood-based spectrum estimator . . . . .	54
4.3	Applications to chaotic time series . . . . .	56
4.4	Distinguishing noisy chaotic flow from colored noise . . . . .	64
4.5	Conclusion . . . . .	67
<b>5</b>	<b>Neighborhood-based phase synchronization detection</b>	<b>69</b>
5.1	Introduction . . . . .	69
5.2	Neighborhood-based phase estimation . . . . .	72
5.3	Phase synchronization of coupled Rössler systems . . . . .	75
5.4	Phase synchronization of coupled Lorenz systems . . . . .	80
5.5	Discussion and conclusion . . . . .	82
<b>6</b>	<b>On phase synchronization detection</b>	<b>85</b>
6.1	Introduction . . . . .	85
6.2	Revisit the definition of instantaneous phase . . . . .	87
6.3	A framework for instantaneous phase definition . . . . .	90
6.4	The effect of noise in phase synchronization detection . . . . .	95
6.5	A band-weighted synchronization index . . . . .	99
6.6	Numerical results . . . . .	100
6.6.1	Effect of noise in phase synchronization detection . . . . .	100
6.6.1.1	Test with sine waves . . . . .	100
6.6.1.2	Test with coupled Rössler systems . . . . .	102

6.6.2	Detecting synchronization with the band-weighted index	109
6.7	Synchronization in EEG signals	112
6.8	Discussion and conclusion	114
<b>7</b>	<b>Conclusion and future work</b>	<b>117</b>
7.1	Contributions of the thesis	117
7.2	Future work	119
	<b>Bibliography</b>	<b>121</b>
	<b>Index</b>	<b>134</b>

# List of Figures

1.1	Structure of this thesis. . . . .	7
2.1	Schematic diagram of time delay embedding and state recurrence. . . . .	11
2.2	Schematic diagram of phase synchronization of coupled chaotic systems. . . . .	22
3.1	Energy of the projection of clean signal vector and noise vector in the local phase space. . . . .	30
3.2	Wave forms of (noisy) Lorenz time series. . . . .	33
3.3	Attractors reconstructed by time delay embedding. . . . .	34
3.4	The power spectra of a Lorenz time series, the phase shuffled surrogate of the Lorenz times series, AR(3), pink noise, and white Gaussian noise. . . . .	35
3.5	Energy distribution of vowel /a/ and car noise (10 dB) in the local phase space. . . . .	38
3.6	Overlap-adding reconstruction of enhanced speech. . . . .	40
3.7	The wave forms of clean speech, noisy speech, and enhanced speech. . . . .	43
3.8	The segSNRs of different classes of sounds for speech with 5 dB car noise and with 5 dB street noise, respectively. . . . .	44

3.9	Evaluation of speech enhancement with four objective measures, i.e., PESQ, $C_{sig}$ , $C_{bak}$ , and $C_{ovl}$ , for speech with car noise and with street noise, respectively. . . . .	45
4.1	The relationship between the reference phase point and its nearest neighbors. . . . .	52
4.2	Schematic diagram of the neighborhood of type-II. . . . .	53
4.3	Histogram of the recurrence times of the neighbors of type-II. . . . .	54
4.4	Power spectra of the Lorenz system estimated by periodogram. . . . .	57
4.5	Histogram of spectral peaks and main frequencies. . . . .	58
4.6	Spectrogram of a clean Lorenz time series by NSE. . . . .	59
4.7	Hidden frequency of the Lorenz time series. . . . .	60
4.8	Energy distribution versus frequency of the Lorenz time series measured from the $x$ component. . . . .	61
4.9	Spectrogram of the Rössler time series by NSE. . . . .	62
4.10	Spectrogram of a laser time series by NSE. . . . .	63
4.11	The power spectra of the clean Lorenz time series, the noisy Lorenz time series, a phase shuffled surrogate data of the noisy Lorenz time series, and the pink noise generated by AR(1), respectively. They are estimated by periodogram. . . . .	65
4.12	The spectrogram (by NSE) of pink noise and the surrogate data, respectively. . . . .	66
4.13	Histogram of the main frequencies. . . . .	67
5.1	The relation between the reference vector and its neighbors in the time domain and in the $(s, \tilde{s})$ -plane. . . . .	74
5.2	Phase synchronization of synchronous Rössler systems ( $\xi = 0.035$ ). . . . .	76

5.3	The estimated synchronization index $\rho$ with respect to embedding dimension and the number of neighbors for synchronous Rössler systems ( $\xi = 0.035$ ). . . . .	77
5.4	The estimated synchronization index $\rho$ with respect to the level of measurement noise. . . . .	78
5.5	The reconstructed attractors of the Lorenz system. . . . .	81
5.6	The unwrapped phase difference of coupled Lorenz systems, and their synchronization index $\rho$ with respect to the level of measurement noise. . . . .	82
5.7	The synchronization index $\rho$ with respect to the band width $\Delta f$ of the linear bandpass filter. . . . .	83
6.1	The pdf's of phase error for a sine wave and an amplitude-modulated sine wave, respectively. The noise level is $\eta = 0.2$ . . . . .	101
6.2	The pdf's of phase error for a sine wave and an amplitude-modulated sine wave, respectively. The noise level is $\eta = 1$ . . . . .	102
6.3	The pdf's of phase error and phase error difference for the coherent Rössler time series with bandpass filter. The noise level is $\eta = 0.2$ . . . . .	103
6.4	The pdf's of phase error and phase error difference for the coherent Rössler time series with bandpass filter. The noise level is $\eta = 1$ . . . . .	104
6.5	The IA $A_x(n)$ and iSNR $r^{(b)}(n)$ of the coherent Rössler time series with bandpass filter, $\eta = 0.2$ . . . . .	105
6.6	The IA $A_x(n)$ and iSNR $r^{(b)}(n)$ of the coherent Rössler time series with bandpass filter, $\eta = 1$ . . . . .	106
6.7	The PS index of numerical estimate and its corresponding theoretical prediction for the coupled coherent Rössler systems with respect to the noise level $\eta$ . The coupling strength is $\xi = 0.035$ . . . . .	107

6.8	The PS index of numerical estimate and its corresponding theoretical prediction for the coupled coherent Rössler systems with respect to the noise level $\eta$ . The coupling strength is $\xi = 0.027$ . . . . .	107
6.9	The PS index of numerical estimate and its corresponding theoretical prediction for the coupled coherent Rössler systems with respect to the noise level $\eta$ . The coupling strength is $\xi = 0.01$ . . . . .	108
6.10	The PS index of numerical estimate and its corresponding theoretical prediction for the coupled coherent Rössler systems with respect to the noise level $\eta$ . The coupling strength is $\xi = 0$ . . . . .	108
6.11	The PS index of numerical estimate and its corresponding theoretical prediction for the coupled noncoherent Rössler systems with respect to the noise level $\eta$ . The coupling strength is $\xi = 0.2$ . . . . .	109
6.12	The band-weighted synchronization index for coupled coherent Rössler systems with respect to the coupling strength $\xi$ and the band-width $\Delta f$ of filter. . . . .	111
6.13	The band-weighted synchronization index for coupled noncoherent Rössler systems with respect to the coupling strength $\xi$ and the band-width $\Delta f$ of filter. . . . .	111
6.14	The synchronization index $\rho_i$ for components of clean data (a) and the noisy version of the clean data (b) in each frequency band with band-width $\Delta f = 0.128$ Hz. The coupled Rössler systems are coherent and the noise level is $\eta = 0.2$ . . . . .	112
6.15	Three pairs of EEG signals measured from the electrodes placed on the right (R) and the left (L) cortical cortex of rats. . . . .	113
6.16	Synchronization analysis for EEG signals in different frequency bands. . . . .	113
6.17	Synchronization analysis for EEG signals with the band-weighted index. . . . .	115

# List of Tables

3.1	Results of noise reduction for the Lorenz time series contaminated by colored noise generated by AR(3). . . . .	34
3.2	Results of noise reduction for the Lorenz time series contaminated by pink noise. . . . .	35
3.3	Results of noise reduction for the Lorenz time series contaminated by its phase shuffled surrogate data. . . . .	36
3.4	Results of noise reduction for the speech corrupted by environmental noise measured in running car. . . . .	39
3.5	Results of speech enhancement for ten speech sentences corrupted by car noise. . . . .	42
3.6	Results of speech enhancement for ten speech sentences corrupted by street noise. . . . .	43



# Abbreviations

AR( $p$ )  $p$ th-order autoregressive process

BT the Blackman-Tukey spectrum estimator

ch.f. characteristic function

CS complete synchronization

DFT discrete Fourier transform

ECG electrocardiograph

EEG electroencephalographic

FFT fast Fourier transform

GS generalized synchronization

i.i.d. independent and identically distributed

IA instantaneous amplitude

IP instantaneous phase

iSNR instantaneous signal-to-noise ratio

linSS linear subspace method

logMMSE log-spectral amplitude minimum mean square error estimator

LP the local projection method

LS lag synchronization

LSS the local subspace method

MPC mean phase coherence

NSE neighborhood-based spectrum estimator

P-BP the scheme that estimates IP with band pass filter

P-HT the scheme that estimates IP with the Hilbert transform directly

P-LP the scheme that estimates IP with LP as preprocessing filter

P-PP the scheme that defines IP in the two-dimensional projection plane

pdf probability density function

PS phase synchronization

rms root-mean-square

segSNR segmental signal-to-noise ratio

SI synchronization index

SMN scale mixture of normal distributions

SNR signal-to-noise ratio

STFT the short-time Fourier transform

TFR time-frequency representation

WN wrapped normal distribution

# Chapter 1

## Introduction

### 1.1 Motivation and objectives

Since Edward N. Lorenz reported the Lorenz system in his paper entitled “Deterministic nonperiodic flow” in 1963 [1], chaos has drawn great attention for it is ubiquitous in both nature (e.g., species interactions in food webs [2]) and man-made systems (e.g., the Lorenz system), and also has many applications (e.g., chaos-based communication). A fundamental characteristic of chaotic system is that it is sensitive to initial conditions, which means that its phase trajectories with almost the same initial conditions diverge exponentially with respect to time as they evolve. This characteristic is also referred to as the “butterfly effect”, and the divergence rate can be quantified by *Lyapunov exponents* [3]. As a result of this effect, the chaotic system appears to be random and can only be predicted for a short time, even though it is well defined and contains no random parameters. Another important characteristic of chaotic system is state recurrence. This concept goes back to Poincaré who stated that the phase trajectory of certain systems will, after a sufficiently long time, returns arbitrarily close to any former phase state. State recurrence of chaotic system can be characterized by recurrence plot [4, 5] and recurrence time statistics [6].

Usually, the chaotic systems are not clearly known in advance, and only scalar time series observed from them are available. Takens’ embedding theorem

provides a framework to investigate the underlying dynamics with only the observed time series [7, 8]. State vectors are first appropriately reconstructed with the scalar time series by time delay embedding. Then this sequence of vectors can be considered as a sample of a phase trajectory of the underlying dynamics in the reconstructed (artificial) phase space, which is topologically equivalent to the evolution of the dynamical system, if the observation function are smooth. Hence, the invariants, such as Lyapunov exponents and *correlation dimension* [9], can be calculated in the phase space reconstructed with the scalar time series. A variety of techniques, such as recurrence plot, recurrence statistics, Poincaré section, and nonlinear autoregressive modeling, have been proposed to explore the underlying dynamics in the reconstructed phase space and can reveal inherent information beyond traditional statistics [10–12]. In the reconstructed phase space, the state recurrences of a reference phase point turn out to be its nearest neighbors, which can provide redundant information but recur with no obvious temporal regularity [13]. The redundant information possessed by state recurrences has been utilized by techniques such as the local projection method (LP) [14], nonlinear prediction [15, 16], and nonlinear autoregressive modeling [12], resulting in better performances than the traditional techniques (e.g., linear autoregression) which are based on linear models and neglect state recurrences.

One difficulty in analyzing chaotic time series is that noise is, more or less, present in the observed data, especially when they are measured from real systems<sup>1</sup>. Chaotic time series usually have broad spectra, which overlap with those of noise in a large range in the frequency domain. As a result, it is difficult to eliminate the noise in contaminated chaotic time series by traditional noise reduction methods which are based on linear models. In the early 1990s, the LP method, which is based on the theory of time delay embedding, has been proposed and further shown to be a promising way to reduce noise for chaotic time series [14, 18–26]. This method has yielded encouraging results for both noisy artificial data (e.g., measured from the Lorenz system) and chaotic experimental data (e.g., NMR-laser data) [22]. Moreover, the LP method also has successful

---

<sup>1</sup>The noise may come from other sources (i.e., environmental noise) or be induced by observation instruments (i.e., measurement noise). These examples are additive noise and treated as measurement noise in this thesis. Another kind of noise is dynamic noise, which not only affects observation of the present state but also enters into the system and thus affects the future evolution of the dynamical system [17].

applications to signals which are not really chaotic but show chaotic-like features, for examples, fetal electrocardiograph (ECG) extraction [27] and speech enhancement [25, 28]. However, these studies almost all assume the noise is white, and the case of chaotic data with colored noise has not yet been tackled.

Spectral analysis provides another framework for chaotic time series analysis [29–33]. However, the traditional spectral analysis, which is usually based on the Fourier transform or other linear models, often fails when applied to chaotic data which have broad spectra. For a chaotic signal with complicated evolution, the simple frequency domain representation may obscure information related to timing, and a time-frequency joint analysis is therefore desirable. However, few studies of time-frequency analysis for chaotic time series have been reported. Chandre *et al.* have performed a time-frequency analysis of Hamiltonian systems [34]. It has been shown that the ridge pattern, extracted from a wavelet decomposition of the time series observed from the Hamiltonian systems, can reveal the phase-space structures (resonance transitions, trappings, etc.). What's more, the relationship between the theory of time delay embedding and spectral analysis has not been discussed yet.

Most of the techniques mentioned above are designed for data measured from a single chaotic system. However, the systems in real life often interact with each other. Then how can we characterize the dynamics of coupled systems? Synchronization analysis addresses the problem. Synchronization is a cooperative behavior which occurs in the coupled systems when they evolve with the same rhythm [35]. The concept of synchronization goes back to Huygens who observed the synchronous behavior of two pendulum clocks suspended on one wooden beam in the 1660s. Research of chaos synchronization starts from the 1980s [36]. For a chaotic system, phase trajectories that start from nearly the same initial conditions diverge exponentially. It therefore seems quite surprising that coupled chaotic systems can become completely synchronized, but this is indeed the case. Chaos synchronization has been realized in physical systems and applied in secure communication [37]. In the 1990s, the concept of phase synchronization (PS), a weak form of synchronization, is proposed to characterize the coupled chaotic oscillators whose instantaneous phases (IP) are locked while their corresponding instantaneous amplitudes are uncorrelated [38, 39]. A

variety of synchronization measures have been proposed to quantify the degree of synchronization with observed chaotic time series [35, 38, 40–51]. Several of them, including nonlinear interdependence, mutual information, and two PS indexes, have been compared with both real electroencephalographic (EEG) signals [49] and artificial data measured from typical coupled chaotic systems. The results show that these measures can give a similar tendency in the degree of synchronization [49], but can be greatly degraded when the noise level is relatively high [50]. It is difficult to say which measure is the best in general, and it is not easy to gain reliable detection, especially for the case with only noisy noncoherent time series.

PS has many applications in both natural (e.g., neuronal oscillations [52,53]) and engineering systems (e.g., chaotic laser array [41]), especially in investigating biomedical signals, for example, brain oscillations [53–55]. However, there are still several open problems of PS detection to be addressed. First, how to treat noncoherent data. For noncoherent data, the IP, defined by the Hilbert transform directly, is no longer monotonic. This results in negative instantaneous frequency which is physically meaningless<sup>2</sup>. Usually, a narrow bandpass filter is applied as preprocessing. Then the problem turns out to be what kind of filter should be used. Second, quantitatively, how the noise will affect the detection of PS from noisy data. For contaminated data, artificial phase slips, introduced by noise, will reduce the reliability of the estimated synchronization index (SI). A band-pass pre-filtering may suppress the effect of noise, but may introduce spurious overestimation of SI as well [56]. Third, how to quantify the degree of PS on the whole. With pre-filtering, only PS between inband components are considered and the components outside the passband are neglected, though these neglected components may be synchronous and make contribution to the interaction of the whole systems as well.

In this thesis, we aim to develop robust methods for noisy chaotic or chaotic-like time series based on two points: 1) combining the theory of time delay embedding with the techniques of signal processing; 2) utilizing the redundant information possessed by state recurrences. As far as we know, few studies have been

---

<sup>2</sup>Instantaneous frequency is defined as the derivative of IP. If IP does not increase monotonously with respect to time, instantaneous frequency will be negative when IP turns to decrease.

reported from these two viewpoints. In this thesis, we present our solutions to the problems mentioned above. In particular, three new methods, i.e., an extension of the LP method for chaotic data contaminated by colored noise, a neighborhood-based time-frequency analysis for chaotic flow, and a neighborhood-based SI, are proposed, utilizing the state recurrences. An analytical study on the effect of noise in IP estimation and PS detection is performed, and a band-weighted SI is further proposed. All these proposed methods are first tested by toy models (e.g., the Lorenz system) and further applied to various real data such as speech and EEG signals.

## 1.2 Outline of the thesis

This thesis includes seven chapters, and presents three main topics. The structure of this thesis and the relationship between each topic are illustrated in Fig. 1.1. In particular, they are organized as follows.

In Chapter 2, the background, including the theory of time delay embedding, the state recurrences of chaotic systems, the LP method, the Blackman-Tukey spectrum estimator, time-frequency analysis, and synchronization analysis, are introduced.

In Chapter 3, an extension of the LP method is proposed and further applied to chaotic time series and speech data. The energy of chaotic data and colored noise is first shown to distribute in a different way in the local phase space. With this observation, a two-step extension of the LP method is proposed to deal with the case with colored noise. Further, applications of this extension to both chaotic data with colored noise and speech contaminated by real environmental noise are given.

In Chapter 4, a time-frequency analysis is performed for chaotic flow (including the Lorenz time series, the Rössler time series, and experimental laser data) with a neighborhood-based spectrum estimator, which utilizes state recurrences. Noisy chaotic flow is distinguished from colored noise according to their different ridge patterns in the time-frequency plane. Moreover, the relationship between the theory of time delay embedding and the frequency domain is prop-

erly explained with the proposed spectrum estimator.

In Chapter 5, a neighborhood-based method is proposed to detect PS, combining the theory of time delay embedding with the Hilbert transform. Simulations with toy models show that this method can avoid the overestimation induced by narrow bandpass filter.

In Chapter 6, PS detection is examined from the viewpoint of signal processing. First, several definitions of IP are revisited and further unified into a framework of IP definition. Second, the effect of noise in IP estimation and PS detection is study analytically. The distribution of the IP error induced by noise is shown to be a scale mixture of normal distribution. Under certain assumption, the estimated PS index is degraded by a factor, which is determined only by the noise level in the pass band. Third, a band-weighted SI is proposed to quantify the degree of synchronization on the whole, and further applied to chaotic time series and EEG signals.

In Chapter 7, contributions of this thesis are summarized and possible directions of future research are given.

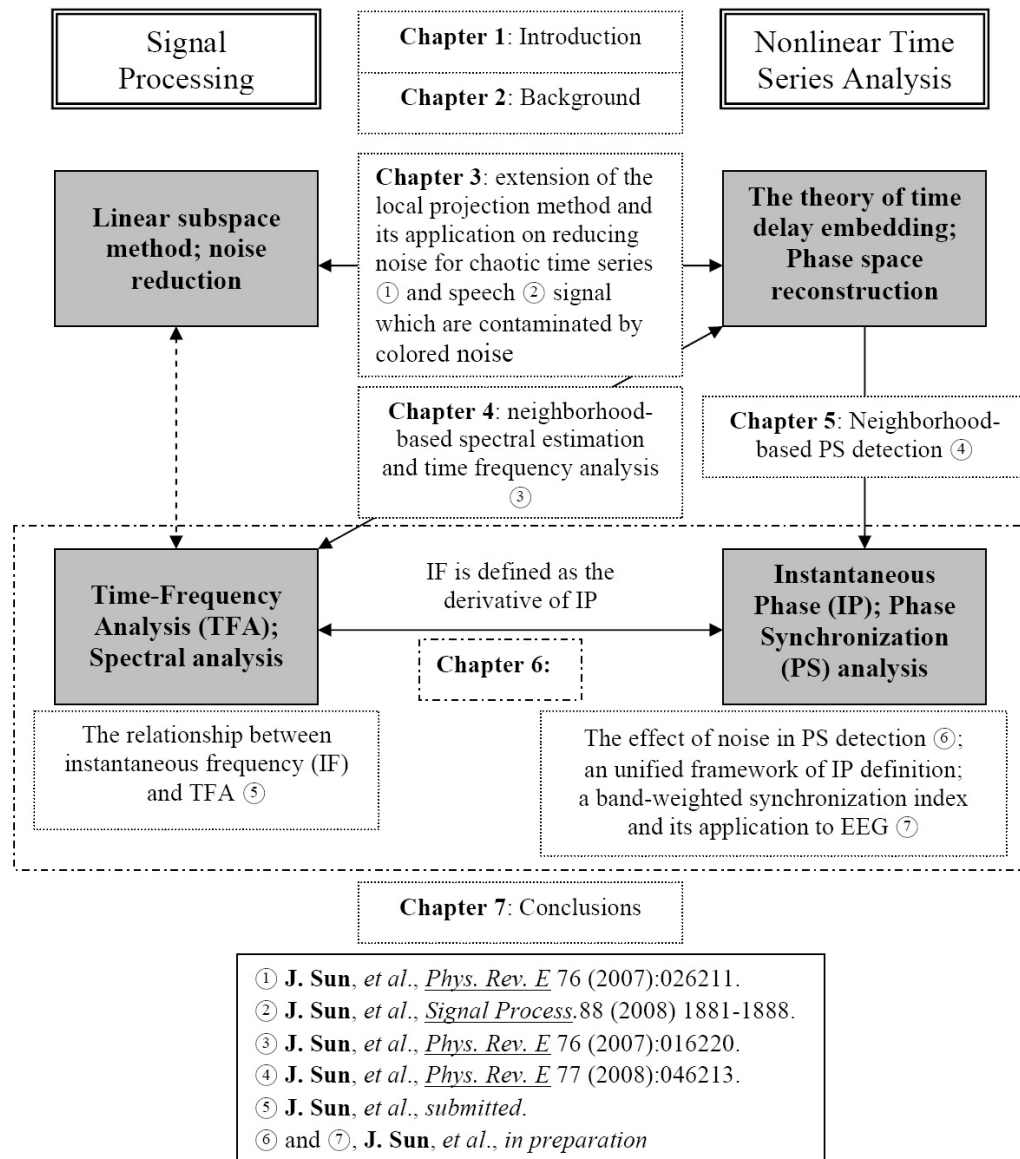


Figure 1.1: Structure of this thesis.



# Chapter 2

## The background of nonlinear time series analysis and processing

This chapter introduces the background of nonlinear time series analysis and processing. In particular, the theory of time delay embedding, the local projection method, the Blackman-Tukey spectrum estimator, time-frequency analysis, and synchronization analysis, are reviewed.

### 2.1 Nonlinear time series analysis

The theory of time delay embedding may be the most popular framework for chaotic time series. In this section, this theory is first reviewed, and further state recurrence, an important feature of chaotic systems, is introduced. Note that other aspects (e.g., Lyapunov exponents [3]) of chaotic systems are not reviewed here because they are not relevant to the focus of this thesis.

#### 2.1.1 Time delay embedding

Let  $\{s(n)\}_{n=0}^{L-1}$  denote a  $L$ -sample time series, which is measured from a dynamical system with sampling interval  $\Delta t$ . To disclose the underlying dynamical

ics, one can embed  $\{s(n)\}$  into a  $d$ -dimensional phase space by constructing the so called *delay coordinate vectors* (also called *phase vectors* and *phase points*)  $\{\mathbf{s}(n)\}_{n=(d-1)\kappa}^{L-1}$ ,

$$\mathbf{s}(n) = [s(n - (d - 1)\kappa), s(n - (d - 2)\kappa), \dots, s(n - \kappa), s(n)]^T, \quad (2.1)$$

where  $d$  is *embedding dimension*,  $\kappa$  is an integer number which indicates the amount of *time delay* (i.e.,  $\kappa\Delta t$  in time units), and superscript  $(\cdot)^T$  denotes vector transpose. According to the embedding theorem which was first presented by Takens [7] and further generalized by Sauer *et al.* [8], the reconstructed attractor formed by the phase vectors  $\{\mathbf{s}(n)\}$  is topologically equivalent to the evolution of the corresponding dynamical system when  $d > 2D_2$ , where  $D_2$  is the *correlation dimension* [9] of the system. The correlation dimension is a metric which quantifies the fractal geometry of the attractor [11]. It can also be considered as the number of freedom degrees of the dynamical system. A schematic diagram of phase space reconstructed by time delay embedding is as Fig. 2.1, in which the *phase portrait* [Fig. 2.1(b)] of a Lorenz time series [Fig. 2.1(a)] is plotted.

The validity of Takens' embedding theorem requires, however, that the system is autonomous and stationary. For a nonstationary time series, the embedding theorem is not directly applicable. But the non-stationarity could potentially be overcome by the technique of *over-embedding*, which states that the dynamics of a  $D_2$ -dimensional deterministic system driven by  $D_p$  slowly varying parameters can be faithfully reconstructed by embedding the observation into a  $d > 2(D_2 + D_p)$  dimensional phase space [57]. Theoretically, if a  $d$ -dimensional embedding makes a faithful representation of the dynamics, the embedding of a greater dimension does well too [11]. However, a greater embedding dimension requires additional computation cost. It is therefore necessary to find the *minimum embedding dimension*  $d_m$ , which is less than  $2D_2$  in general. In nonlinear time series analysis,  $d_m$  is a useful measure to quantify a nonlinear process, and can be effectively determined by the *false-nearest neighbors* (FNN) algorithm [58].

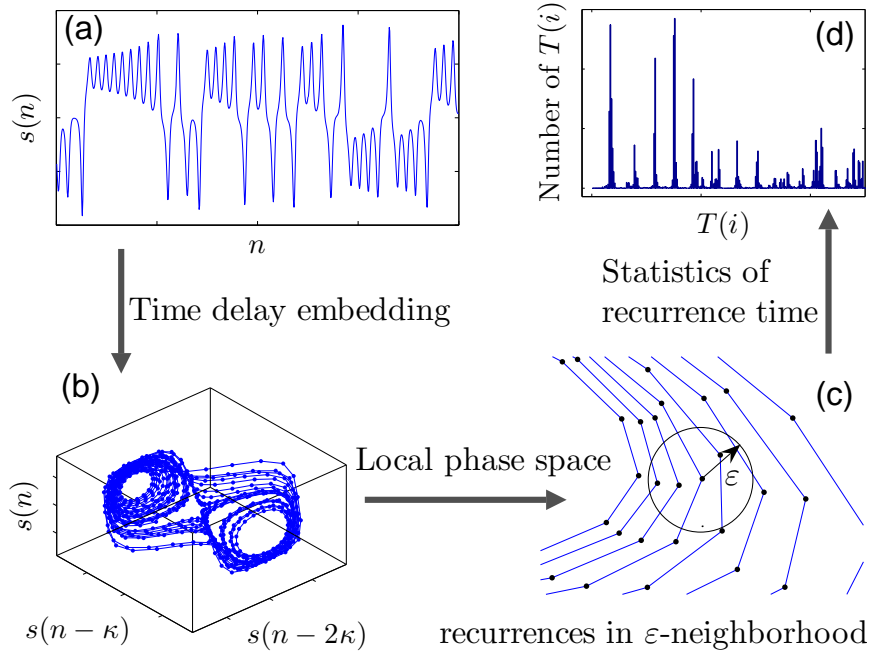


Figure 2.1: Schematic diagram of time delay embedding and state recurrence. (a) a segment of Lorenz time series; (b) the phase portrait of the data in (a), reconstructed by time delay embedding; (c) a local blowup of the phase portrait in (b), the circle with radius  $\varepsilon$  denotes the  $\varepsilon$ -neighborhood of the reference phase point which is located at the center of the circle, other points in this circle denote the neighbors, i.e., the state recurrences, of the reference phase point; (d) statistics of the recurrence time of all the phase points.

### 2.1.2 State recurrence

Besides the sensitivity to initials, state recurrence is another important characteristic of chaotic systems. The concept of state recurrence goes back to Poincaré's recurrence theorem which states that certain systems can, after a sufficiently long time, return arbitrarily close to any former state. Given a time series  $\{s(n)\}_{n=0}^{L-1}$ , its phase portrait can be obtained by time delay embedding. In the reconstructed phase space, the state recurrences of reference phase point  $\mathbf{s}(n)$  turn out to be its neighbors in the  $\varepsilon$ -neighborhood, which is defined as

$$\mathcal{N}_n \triangleq \{\mathbf{s}(k) : \|\mathbf{s}(k) - \mathbf{s}(n)\| < \varepsilon, (d-1)\kappa \leq k \leq L-1\}. \quad (2.2)$$

The  $\varepsilon$ -neighborhood can be further arranged as  $\mathcal{N}_n = \{\mathbf{s}(k_1), \mathbf{s}(k_2), \dots, \mathbf{s}(k_N)\}$ ,  $k_1 < k_2 < \dots < k_N$ , where  $N = |\mathcal{N}_n|$  is the number of neighbors in  $\mathcal{N}_n$ . A schematic diagram of  $\varepsilon$ -neighborhood is shown in Fig. 2.1(c). The  $\varepsilon$ -neighborhood is a collection of phase points whose distances to the reference phase point are smaller than  $\varepsilon$ . The neighbors, i.e., the state recurrences, of the reference phase point can provide redundant information for the reference phase point but recur with no obvious temporal regularity, as will be demonstrated in detail in Chapter 4.

The recurrence time for reference point  $\mathbf{s}(n)$  is defined as the time intervals between temporally consecutive neighbors [6], i.e.,

$$T_n(i) = k_{i+1} - k_i, \quad i = 1, \dots, N - 1. \quad (2.3)$$

The recurrence time of each neighbor appears to be irregular [see Fig. 2.1(d)]; nonetheless, the mean recurrence time obeys a scaling law [6]. Techniques based on state recurrence have been proposed [4, 5, 59, 60]. For example, the statistics of recurrence time has been applied to detect nonstationarity and state transitions [59]. Another technique based on state recurrence is the recurrence plot, which can visualize the times at which a phase trajectory visits roughly the same area in the phase space [4, 5]. Moreover, the pattern of the recurrence plot can be quantified by recurrence quantification analysis based on its small-scale structures which can reflect the number and duration of recurrences of a dynamical system [5].

In chaotic signal processing, on the one hand, techniques, such as the LP method [18, 25] and nonlinear prediction [16], can obtain positive results by utilizing the redundant information possessed by state recurrences; on the other hand, the conventional techniques, such as linear autoregression and wavelet analysis, often fail in studying chaotic time series because they neglect the scattered state recurrences. So techniques, which can utilize the long-term state recurrences in chaotic time series, are expected to perform better and gain further insights beyond those traditional techniques.

## 2.2 Noise reduction for chaotic time series

Noise is unavoidable in observed time series. The presence of noise may obscure or even destroy the fractal structure of a chaotic attractor, and may corrupt the calculation of invariants such as correlation dimension and Lyapunov exponents [21]. Therefore, it is highly desirable to reduce the noise level. However, the conventional noise reduction methods are designed for signals that can be treated by certain linear models and often fail to eliminate noise from a contaminated chaotic time series [11]. Noise reduction based on the theory of time delay embedding has been widely studied, and may be the most promising way to reduce noise for chaotic time series [14, 18–20, 22–24]. Several methods have been proposed independently to achieve this in the local phase space [18–20], and further proved to be special cases of an optimal one [14], which is named the *local projection* (LP) method. The LP method has been successfully applied to both artificial data (e.g., data measured from the Lorenz system) and real data such as NMR-laser data [22], ECG signals [61], and speech signals [25, 28].

Recently, the *local subspace* (LSS) method was proposed using weighted projection in the local phase space, and the LP method [25] is proved to be its least-square case [26, 62]. The LSS method, actually an extension of the *linear subspace* technique [63] to the local phase space, utilizes the redundant information of state recurrences appropriately and thus can reduce noise for chaotic data effectively. Nevertheless, both the LP method and the LSS method assume the noise is additive white noise. A more general phase space projector has been further deduced with no assumption of independence between noise and clean signal [64]. However, this generalization seems impossible to be implemented numerically, and only a reduced case with an additional independence assumption was implemented.

### 2.2.1 The locally linear model

Given a  $d$ -dimensional vector sequence  $\{\mathbf{s}(n)\}_{n=(d-1)\kappa}^{L-1}$ , the trajectory formed by it in the reconstructed phase space represents the evolution of the correspond-

ing dynamical flow,

$$\mathbf{s}(n+1) = F[\mathbf{s}(n)], \quad (2.4)$$

however, the mapping function  $F(\cdot)$  is usually unknown in advance. Since  $F(\cdot)$  may be highly nonlinear, it is difficult, if not impossible, to estimate its exact global form directly from the vector sequence  $\{\mathbf{s}(n)\}$ . A way to treat this problem is to approximate the globally nonlinear function  $F(\cdot)$  in the local phase space, i.e., the  $\varepsilon$ -neighborhood  $\mathcal{N}_n$  [Eq. (2.2)], by a locally linear function  $\hat{F}_n$ . Then, the collection of all these locally linear models, i.e.,  $\{\hat{F}_n\}_{n=(d-1)\kappa}^{L-1}$ , can approximate the global modeling function  $F(\cdot)$  reasonably. Although locally linear, this approximation is still globally nonlinear. As long as the local mapping functions are properly designed, they are expected to give a better modeling for the underlying dynamics than a globally linear approximation.

## 2.2.2 The local projection method

Let  $s(n) = x(n) + w(n)$  denote the time series contaminated by noise, where  $x(n)$  is the original clean data and  $w(n)$  is the additive white noise with zero mean. By embedding the noisy time series  $\{s(n)\}_{n=0}^{L-1}$  in a  $d$ -dimensional phase space, a simple estimation of  $\mathbf{x}(n)$  can be obtained as  $\hat{\mathbf{x}}(n) = \bar{\mathbf{s}}(n)$ , where

$$\bar{\mathbf{s}}(n) \triangleq \frac{1}{N} \sum_{\mathbf{s}(k) \in \mathcal{N}_n} \mathbf{s}(k), \quad (2.5)$$

is the geometric mean of the neighbors in the  $\varepsilon$ -neighborhood of reference point  $\mathbf{s}(n)$  [20].

The LP method assumes that the noise is white and the local phase space, i.e., the  $\varepsilon$ -neighborhood  $\mathcal{N}_n$ , of reference point  $\mathbf{s}(n)$ , can be divided into an  $M$ -dimensional *signal subspace* and a  $(d - M)$ -dimensional *noise subspace* [14, 25], where  $M$  is the minimum embedding dimension of the dynamical system [58]. The signal subspace contains most of the clean signal plus a certain amount of the noise components, while the noise subspace contains most of the noise components and a certain, small, amount of the signal components. The energy of white noise is almost uniformly distributed on each direction of the local phase space. For a preset  $M$ , the noise subspace can be estimated by minimizing the

total energy that is distributed in it. The minimization turns out to be the standard eigenvalue decomposition for the covariance matrix  $\hat{\mathbf{C}}_n$  of the neighborhood  $\mathcal{N}_n$ , i.e.,

$$\hat{\mathbf{C}}_n \mathbf{u}_i - \lambda_i \mathbf{u}_i = 0, \quad (2.6)$$

where matrix  $\hat{\mathbf{C}}_n$  is defined as

$$\hat{\mathbf{C}}_n = \frac{1}{N} \sum_{\mathbf{s}(k) \in \mathcal{N}_n} [\mathbf{s}(k) - \bar{\mathbf{s}}(n)][\mathbf{s}(k) - \bar{\mathbf{s}}(n)]^T. \quad (2.7)$$

Sorting the eigenvalues  $\Lambda = \text{diag}(\lambda_1, \lambda_2, \dots, \lambda_d)$  in descending order, the eigenvectors  $\mathbf{U}_1 = [\mathbf{u}_1, \dots, \mathbf{u}_M]$ , associated with the  $M$  largest eigenvalues, span the signal subspace, and the eigenvectors  $\mathbf{U}_2 = [\mathbf{u}_{M+1}, \dots, \mathbf{u}_d]$ , corresponding to the  $(d - M)$  smallest eigenvalues, span the noise subspace, respectively. Then the phase vector  $\mathbf{s}_n$  can be decomposed as

$$\mathbf{s}(n) = \bar{\mathbf{s}}(n) + \mathbf{U}_1 \mathbf{U}_1^T [\mathbf{s}(n) - \bar{\mathbf{s}}(n)] + \mathbf{U}_2 \mathbf{U}_2^T [\mathbf{s}(n) - \bar{\mathbf{s}}(n)] \quad (2.8)$$

in the local phase space, where  $\mathbf{U}_1 \mathbf{U}_1^T [\mathbf{s}(n) - \bar{\mathbf{s}}(n)]$  and  $\mathbf{U}_2 \mathbf{U}_2^T [\mathbf{s}(n) - \bar{\mathbf{s}}(n)]$  are the projections of  $[\mathbf{s}(n) - \bar{\mathbf{s}}(n)]$  in the signal subspace and the noise subspace, respectively. Eliminating  $\mathbf{U}_2 \mathbf{U}_2^T [\mathbf{s}(n) - \bar{\mathbf{s}}(n)]$ , we can obtain the enhanced signal vector,

$$\hat{\mathbf{x}}(n) = \bar{\mathbf{s}}(n) + \mathbf{U}_1 \mathbf{U}_1^T [\mathbf{s}(n) - \bar{\mathbf{s}}(n)]. \quad (2.9)$$

As each element of the time series  $\{s(n)\}$  appears as an entry of  $d$  successive time delay vectors,  $\mathbf{s}(l)$ ,  $l = n, \dots, n + (d - 1)\kappa$ , there are  $d$  enhancements for element  $s(n)$  which may be different in value. Then the arithmetic mean over these values is taken as the final enhancement of element  $x(n)$ . More details about the LP method and its generalization can be found in Refs. [25, 26, 62].

## 2.3 Spectrum estimation and time-frequency analysis

Spectral analysis and time-frequency analysis are two popular tools for time series [29–33]. Spectral analysis has been applied to chaotic time series [29, 31–33, 65]. For example, it has been used to distinguish chaotic sequence from colored noise [29]. However, it is not so easy [33, 65], especially for the case of chaotic data contaminated by observational noise. This is because the simple spectral analysis may obscure information related to timing. Time-frequency joint analysis is therefore desirable to unveil the features of dynamical systems [66]. However, few studies of time-frequency analysis for chaotic time series have been reported.

There are various methods to estimate spectra from a time series and different ways to implement time-frequency analysis. In this section, we only introduce the Blackman-Tukey (BT) spectrum estimator and the basic idea of time-frequency analysis [67–69], which are relevant to the neighborhood-based time-frequency analysis to be presented in Chapter 4.

### 2.3.1 Spectrum estimation

Given a signal  $s(t)$ , its Fourier transform is,

$$S(f) = \int_{-\infty}^{\infty} s(t)e^{-j2\pi ft} dt. \quad (2.10)$$

For a  $L$ -sample time series  $\{s(n)\}_{n=0}^{L-1}$  which are measured from  $s(t)$  with sampling interval  $\Delta t$ , its discrete-time Fourier transform (DTFT) is defined as,

$$S(\omega) = \sum_{n=0}^{L-1} s(n)e^{-j\omega n}, \quad (2.11)$$

in radians per sample. If the DTFT is defined in units of Hz, Eq. (2.11) turns out to be

$$S(f) = \sum_{n=0}^{L-1} s(n)e^{-j2\pi fn/f_s}, \quad (2.12)$$

where  $f_s = \frac{1}{\Delta t}$  is sampling frequency. Note that in Eq. (2.11),  $\omega$  denotes digital frequency in units of *radians/sample*; while in Eq. (2.12),  $f$  denotes physical frequency in units of Hz. The relationship between them are  $\omega = \frac{2\pi f}{f_s}$ . In this thesis, both denotations  $\omega$  and  $f$  are used for convenience. Denotation  $\omega$  is often adopted in the case of discrete time.

If  $s(n)$  is wide-sense stationary, its *autocorrelation* is defined as

$$r_s(k) = \lim_{L \rightarrow \infty} \frac{1}{2L+1} \sum_{n=-L}^L s(n+k)s^*(n), \quad (2.13)$$

where the superscript  $(\cdot)^*$  denotes the conjugate of  $(\cdot)$ . Given only a finite point sequence  $[s(0), s(1), \dots, s(L-1)]^T$ ,  $r_s(k)$ , defined by Eq. (2.13), can be estimated by

$$\hat{r}_s(k) = \frac{1}{L} \sum_{n=0}^{L-1-k} s(n+k)s^*(n), \quad k = 0, 1, \dots, L-1, \quad (2.14)$$

with  $\hat{r}_s(-k) = \hat{r}_s^*(k)$  for  $-L < k < 0$  and  $\hat{r}_s(k) = 0$  for  $|k| \geq L$ . Then the power spectra, known as *periodogram*, can be obtained by taking the DTFT to  $\hat{r}_s(k)$ , i.e.,

$$\hat{P}_{per}(\omega) = \sum_{k=-L+1}^{L-1} \hat{r}_s(k)e^{-j\omega k}. \quad (2.15)$$

There are two ways to reduce the variance of periodogram, one is to reduce the variance of the estimated autocorrelation by averaging, the other is to decrease the contribution of the unreliable estimates by applying a window to them. The BT spectrum estimator, given by

$$\hat{P}_{BT}(\omega) = \sum_{k=-L+1}^{L-1} \hat{r}_s(k)w(k)e^{-j\omega k}, \quad (2.16)$$

takes the latter strategy, where  $w(k)$  is a window that is applied to the autocorrelation estimates  $\hat{r}_s(k)$ . If  $w(k)$  is a rectangular window between  $[-L_w \ L_w]$  with

$L_w < L - 1$ , then the estimates of  $\hat{r}_s(k)$  at  $(L_w - L + 1]$ , which have the largest variance, are neglected in spectrum estimation. As a result, the estimated power spectra have a smaller variance, at the price of a reduction in frequency resolution, since a smaller number of autocorrelation estimates are used in spectrum estimation.

If  $w(k)$  is a Bartlett (triangular) window, i.e.,

$$w(k) = \begin{cases} \frac{L-|k|}{L} & ; |k| \leq L \\ 0 & ; |k| > L \end{cases}, \quad (2.17)$$

the BT spectrum estimator [Eq. (2.16)] can be written as

$$\hat{P}_{BT}(\omega) = \frac{1}{L} \sum_{k=-L}^L (L - |k|) \hat{r}_s(k) e^{-j\omega k} = \frac{1}{L} \mathbf{e}^H \hat{\mathbf{R}}_s \mathbf{e}, \quad (2.18)$$

where  $\mathbf{e} = [1, e^{j\omega}, e^{j2\omega}, \dots, e^{j(L-1)\omega}]^T$ ,  $\hat{\mathbf{R}}_s$  is the estimate of *autocorrelation matrix*, and the superscript  $(\cdot)^H$  denotes the Hermitian transpose of  $(\cdot)$ , i.e.,  $(\cdot)^H = [(\cdot)^T]^*$ . If  $s(n)$  is wide-sense stationary, its  $L \times L$  autocorrelation matrix is defined as  $\mathbf{R}_s = E\{\mathbf{s}\mathbf{s}^H\}$  with  $\mathbf{s} = [s(0), s(1), \dots, s(L-1)]^T$ . Given only a finite point sequence,  $\mathbf{R}_s$  can be estimated by

$$\hat{\mathbf{R}}_s = \begin{bmatrix} \hat{r}_s(0) & \hat{r}_s^*(1) & \hat{r}_s^*(2) & \dots & \hat{r}_s^*(L-1) \\ \hat{r}_s(1) & \hat{r}_s(0) & \hat{r}_s^*(1) & \dots & \hat{r}_s^*(L-2) \\ \hat{r}_s(2) & \hat{r}_s(1) & \hat{r}_s(0) & \dots & \hat{r}_s^*(L-3) \\ \vdots & \vdots & \vdots & \ddots & \vdots \\ \hat{r}_s(L-1) & \hat{r}_s(L-2) & \hat{r}_s(L-3) & \dots & \hat{r}_s(0) \end{bmatrix}, \quad (2.19)$$

where  $\hat{r}_s(k)$  is the autocorrelation estimates [Eq. (2.14)] and has property  $\hat{r}_s(k) = \hat{r}_s^*(-k)$ .

With eigenvalue decomposition of the  $L \times L$  matrix  $\hat{\mathbf{R}}_s$ , the BT spectrum estimator  $\hat{P}_{BT}(\omega)$  [Eq. (2.18)] can be expressed as

$$\hat{P}_{BT}(\omega) = \frac{1}{L} \sum_{i=1}^L \lambda_i |\mathbf{e}^H \mathbf{u}_i|^2, \quad (2.20)$$

where the eigenvalues of  $\hat{\mathbf{R}}_s$  are arranged in descending order,  $\lambda_1 \geq \lambda_2 \geq \dots \geq$

$\lambda_L$ , and  $\mathbf{u}_i$  is the eigenvector associated with  $\lambda_i$ . A principle component version of  $\hat{P}_{BT}(\omega)$  is

$$\hat{P}_{PC-BT}(\omega) = \frac{1}{L} \sum_{i=1}^K \lambda_i |\mathbf{e}^H \mathbf{u}_i|^2, \quad (2.21)$$

where  $K < L$ .

### 2.3.2 Time-frequency analysis

The straightforward representation of a signal is  $s(t)$ , i.e., as a function of time in the time domain. This representation has the highest time resolution but does not give any frequency information of the signal. With the Fourier transform of  $s(t)$ , the signal can be represented in the frequency domain, i.e.,  $S(f)$  [see Eq. (2.10)]. In contrast, the frequency domain representation has the highest frequency resolution but shows no time information. A tradeoff between these two representations is time-frequency representation (TFR) which provides some temporal information and some spectral information simultaneously. TFRs are useful in analyzing the signals which contain multiple time-varying frequencies [66, 69]. There are various TFRs, such as the short-time Fourier transform (STFT) and Wigner distribution. Here only STFT is introduced.

To study the properties of a signal at a particular time  $t$ , a small piece of signal around  $t$  is usually extracted by a window  $g(t)$ . The extracted signal,  $s_t(\tau) = s(\tau)g(\tau - t)$ , is a function of two times, i.e., the fixed time  $t$  which we are interested in, and the running time  $\tau$  which indicates the temporal distance to the fixed time. Then the Fourier transform to the short-time signal  $s_t(\tau)$  is

$$S_t(f) = \int_{-\infty}^{\infty} s(\tau)g(\tau - t)e^{-j2\pi f\tau} d\tau. \quad (2.22)$$

For each time  $t$ , a spectra can be obtained, and all the spectra of different time yield a time-frequency distribution of the energy of  $s(t)$ , i.e.,

$$P(t, f) = |S_t(f)|^2. \quad (2.23)$$

This time-frequency distribution is commonly named *spectrogram*. Here the power spectra of the windowed signal is obtained by the Fourier transform. In

Chapter 4, a neighborhood-based method is proposed to estimate the power spectra of the windowed chaotic time series.

## 2.4 Synchronization analysis

Synchronization can be considered as an “adjustment of rhythms of oscillating objects due to their weak interaction” [35]. This cooperative behavior exists in both natural and engineering systems, for examples, coupled chaotic oscillators [38, 44], chaotic laser array [41], biomedical signals [39], neuronal oscillations [52–54], electrochemical oscillations [70], and coupled nanomechanical oscillators [71]. This phenomenon can not only reveal the mechanism and function of the coupled systems (e.g., communication during cognitive processing in human brain [54]) but also help to gain new applications such as providing clinical evidence in Parkinson’s disease treatments [55]. Therefore, it has drawn increasing attention in recent years.

A variety of methods have been proposed to detect synchronization with observed time series [35, 38, 40–51]. Several synchronization measures, including nonlinear interdependence [46–48], mutual information, coherence function, and two PS indexes, have been compared with real EEG signals. We show that these measures can give a similar tendency in the degree of synchronization [49]. Further, these measures are tested with artificial data measured from typical coupled chaotic systems. Results show that these measures work effectively when the noise level is low, but can be greatly degraded when the noise level is relatively high [50]. It is difficult to say which measure is the best in general.

### 2.4.1 Synchronization definition

Let  $\mathbf{v}_{1,2}$  denote the set of dynamical variables which describe the state of two coupled self-sustained oscillators,  $\Sigma_{1,2}$ , respectively <sup>1</sup>. Synchronization has been found to present a variety of forms:

---

<sup>1</sup>For brevity, here  $\mathbf{v}_1$  and  $\mathbf{v}_2$  are denoted by  $\mathbf{v}_{1,2}$ , and system  $\Sigma_1$  and system  $\Sigma_2$  are denoted by  $\Sigma_{1,2}$ , respectively. In this thesis, this kind of abbreviation is adopted unless stated otherwise.

- *Complete synchronization (CS)*. For two identical oscillators which are coupled, CS occurs when their states become to be completely identical after an enough long time evolution. In other words, for different initials  $\mathbf{v}_1(0)$  and  $\mathbf{v}_2(0)$ , the difference of their states  $|\mathbf{v}_1(t) - \mathbf{v}_2(t)| \rightarrow 0$ , as  $t \rightarrow \infty$ .
- *Generalized synchronization (GS)*. GS occurs in coupled oscillators when there is a function  $\Psi(\cdot)$ , such that the relation  $\mathbf{v}_1(t) = \Psi(\mathbf{v}_2(t))$  holds after a transitory evolution from appropriate initials. It means that the dynamical state of one of the oscillators is completely determined by the state of the other. GS can occur in coupled oscillators which are different (e.g., there is mismatch between the parameters of the two oscillators). Actually, CS is a particular case of GS when the relation function is identity, i.e.,  $\Psi(\mathbf{v}_2) = \mathbf{v}_2$ .
- *Lag synchronization (LS)*. LS occurs when the relation  $\mathbf{v}_1(t) = \mathbf{v}_2(t + \tau)$  holds for two coupled oscillators, where  $\tau$  is time lag. This means that the dynamical state of one of the oscillator follows the state of the other.
- *Phase synchronization (PS)*. PS implies that the coupled oscillators are phase locked. More details will be introduced in the next section.

### 2.4.2 Phase synchronization

PS is a dynamical behavior of weakly coupled oscillators whose *instantaneous phase (IP)* are locked while their *instantaneous amplitudes (IA)* may be uncorrelated. Let  $\phi_{1,2}(t)$  denote the IPs of the coupled oscillators  $\Sigma_{1,2}$ , respectively.  $l:m$  PS occurs when the inequality  $|l\phi_1(t) - m\phi_2(t)| < \text{const.}$  holds, where *const.* is a constant, and  $l$  and  $m$  are positive integers. When  $l:m = 1$ , the  $l:m$  PS reduces to be the most straightforward PS, i.e., the 1:1 PS. A schematic diagram of 1:1 PS is given in Fig. 2.2, in which, the IP difference is smaller than a constant [Fig. 2.2(b)], while their IAs are uncorrelated [Fig. 2.2(e)].

Various IPs have been defined. One class of them is based on particular transforms, such as the Hilbert transform [38], the wavelet transform [40], and a generalized transform with a Gaussian filter [41], to the observable signal.

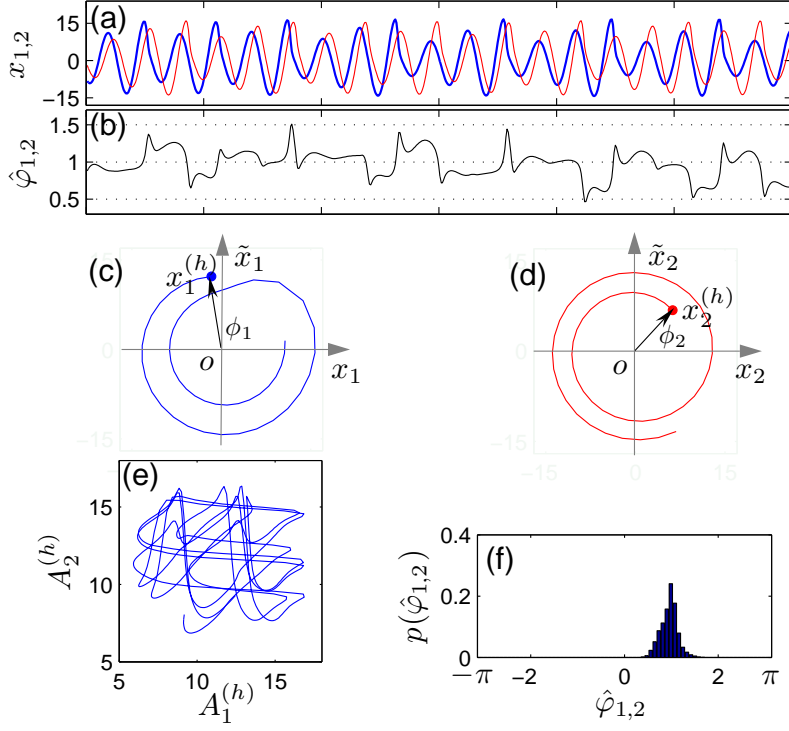


Figure 2.2: Schematic diagram of phase synchronization in coupled chaotic systems. (a) two time sequences which are measured from the variables  $x_{1,2}$  of coupled Lorenz systems; (b) the IP difference between  $\phi_1$  and  $\phi_2$  are smaller than a constant, which implies that the coupled systems are phase locked; (c) and (d) illustration of IP definition for  $x_{1,2}$  respectively; (e) the IAs of the coupled systems are uncorrelated; (f) the distribution of the IP difference which are wrapped into  $(-\pi, \pi]$ , the concentrated distribution implies that the coupled systems are phase synchronized.

Another class of IP is defined as the angle of evolving trajectory, which is reconstructed from the two-dimensional projection of the system [35, 42] or the time derivative of the projection [43, 44], around a fixed point. Among these IP definitions, the most popular one is based on the Hilbert transform. Given the observable signal  $s(t)$ , its analytic signal is defined as  $s^{(h)}(t) = s(t) + j\tilde{s}(t) = A^{(h)}(t)e^{j\phi^{(h)}(t)}$ , where  $A^{(h)}(t)$  is the IA,  $\phi^{(h)}(t)$ , given by

$$\phi^{(h)}(t) = \arg [s^{(h)}(t)] = \arctan \frac{\tilde{s}(t)}{s(t)}, \quad (2.24)$$

is the IP, and  $\tilde{s}(t) = \mathcal{H}[s(t)] = \frac{1}{\pi} \text{P.V.} \int_{-\infty}^{\infty} \frac{s(\tau)}{t-\tau} d\tau$  is the Hilbert transform of  $s(t)$  (here P.V. means that the integral is taken in the sense of Cauchy principal value),

in which  $\mathcal{H}(\cdot)$  denotes the operator of Hilbert transform. This IP definition is illustrated in Figs. 2.2(c) and 2.2(d), in which  $x_{1,2}^{(h)}$  evolve counterclockwise in the  $(x_{1,2}, \tilde{x}_{1,2})$ -plane, respectively. The IPs are defined as the angles between  $\vec{o}x_{1,2}$  and  $\vec{o}\tilde{x}_{1,2}^{(h)}$ , i.e.,  $\phi_{1,2} = \angle x_{1,2} o x_{1,2}^{(h)}$ , respectively, which increase as time going on.

Let  $\varphi = [l\phi_1(n) - m\phi_2(n)] \bmod(2\pi)$  denote the  $l:m$  IP deference between  $\Sigma_{1,2}$  which are wrapped into  $(-\pi \ \pi]$  by reducing its modulo  $2\pi$ . There are two popular PS indexes which both quantify how concentrated the distribution of phase difference is. These two indexes are based on entropy [39, 56] and circular statistics [72, 73], respectively, and defined as follows:

- The PS index based on entropy is defined as

$$\rho = (S_{\max} - S)/S_{\max}, \quad (2.25)$$

where  $S = -\sum_{i=1}^K p_i \ln p_i$  is the entropy of the distribution  $p(\varphi)$ ,  $S_{\max} = \ln K$ , and  $K$  is the number of bins of distribution [39, 56].

- The PS index based on circular statistics is *mean phase coherence* (MPC), which is defined as  $\rho = \|E[e^{j\varphi}]\|$  [72, 73]. Given estimates  $\{\hat{\varphi}(n)\}_{n=0}^{L-1}$ , MPC can be estimated by

$$\hat{\rho} = \left\{ \left[ \frac{1}{L} \sum_{n=0}^{L-1} \cos \hat{\varphi}(n) \right]^2 + \left[ \frac{1}{L} \sum_{n=0}^{L-1} \sin \hat{\varphi}(n) \right]^2 \right\}^{1/2}. \quad (2.26)$$

### 2.4.3 Physical conditions for instantaneous phase definition

Signal  $s(t)$  can be written as  $s(t) = \mathcal{R}[A(t)e^{j\phi(t)}]$ , where  $\mathcal{R}(\cdot)$  denotes the real part of complex variable  $(\cdot)$ . Usually, the corresponding imaginary counterpart  $\mathcal{I}[A(t)e^{j\phi(t)}]$  can not be observed and can only be assumed to relate to  $s(t)$  by a certain operation, i.e.,  $\mathcal{I}[A(t)e^{j\phi(t)}] = \tilde{\mathcal{H}}[s(t)]$ . To define IP, various operators  $\tilde{\mathcal{H}}(\cdot)$  have been proposed and the Hilbert transform  $\mathcal{H}(\cdot)$  is the most popular one. Three physical conditions have been proposed to confine the operator  $\tilde{\mathcal{H}}(\cdot)$ :

- **Condition I: amplitude continuity and differentiability.** This condition guarantees that the associated amplitude  $A(t)$  is continuous and differentiable.

- Condition II: *phase independence of scaling and homogeneity*. This condition means that the IPs of signal  $s(t)$  and  $c \cdot s(t)$  are the same. In other words, this condition requires the operator possesses the property  $\tilde{\mathcal{H}}[cs(t)] = c\tilde{\mathcal{H}}[s(t)]$ .
- Condition III: *harmonic correspondence*. This condition requires that for any constant amplitude  $A > 0$ , frequency  $\omega > 0$ , and phase  $\psi$ , the operator satisfies  $\tilde{\mathcal{H}}[A \cos(\omega t + \psi)] = A \sin(\omega t + \psi)$ .

The Hilbert transform  $\mathcal{H}(\cdot)$  has been proven to be the only one that satisfies these physical conditions [74]. Considering this, we only investigate the IP definition based on the Hilbert transform in this thesis. More discussions on these conditions and other IP definitions can be found in Ref. [74].

## Chapter 3

# Reducing noise in the local phase space

In this chapter, a two-step extension of the local projection (LP) method is proposed to reduce colored noise for chaotic time series in the local phase space. Furthermore, this extension is adapted to enhance speech signals which are contaminated by environmental noise.

With the observation that the energy of colored noise is mainly distributed in a particular low dimensional subspace, a noise dominated subspace is first estimated by the energy distribution of colored noise. At step one, for the reference phase point, the components projected into the noise dominated subspace are deleted and the enhanced phase point is reconstructed with the remaining components. The residual error of the output of step one tends to distribute on each direction uniformly. So at step two, the LP method is further applied to the output of step one, treating the residual error as white noise. Experiments show that this two-step extension of LP performs well in eliminating colored noise for both chaotic time series and speech signals.

## 3.1 Introduction

### 3.1.1 Noise reduction in the local phase space

As introduced in Sec. 2.2, the presence of noise can greatly affect the analysis of chaotic time series. However, the conventional techniques based linear models often fail to eliminate noise from contaminated chaotic time series [11]. The theory of time delay embedding provides a promising framework to reduce noise for chaotic time series. Methods based time delay embedding reduce noise in the local phase space by projection, and thus named the local projection (LP) method [13, 14, 18–20, 22–26, 28, 61, 64]. All these methods decompose the local phase space into two orthogonal subspaces, called the *signal subspace* which contains most of the pure signal components plus some noise components and the *noise subspace* that contains the remaining noise components and a small amount of signal components. Moreover, these methods almost all assume the noise is additive white noise. The case of chaotic time series contaminated by colored noise has not yet been tackled <sup>1</sup>. The LP method yields poor results for chaotic time series contaminated by colored noise, because its estimated signal subspace may include many large noise components.

To deal with the case with colored noise, a two-step extension of the LP method is proposed in this chapter. This extension assumes that the colored noise is stationary, and a segment of the colored noise or its covariance matrix can be obtained in advance <sup>2</sup>. At the first step, a *noise dominated subspace* can be estimated (spanned by the eigenvectors associated with the several largest eigenvalues) by performing eigenvalue decomposition to the covariance matrix of the colored noise. Then in each local phase space, the components of the reference phase point projected into the noise dominated subspace are deleted and the enhanced phase point are reconstructed with the remaining components. After the first step, most of the colored noise has been eliminated. The energy of residual

---

<sup>1</sup>In the frequency domain, a random sequence is called white noise if its spectra are flat, otherwise it is called colored noise. Correspondingly, in the local phase space, the energy of white noise distributes uniformly on each direction, while the energy of colored noise mainly distributes in a particular low dimensional subspace.

<sup>2</sup>Note that this assumption is widely adopted in signal processing, for example, in speech enhancement, a segment of pure noise can be obtained during a period of speech absence.

error tends to distribute “uniformly” on each direction. Thus the residual error can be treated as white noise and the LP method is further applied to the output of the first step.

### 3.1.2 Speech enhancement with the local projection method

In the past several decades, a variety of speech enhancement algorithms have been proposed, including noise suppression in the frequency domain (e.g., spectral subtraction [75], Wiener filtering [75]) and noise elimination in the linear signal subspace [63, 76]. The signal space, properly reconstructed from noisy speech, can be divided into two orthogonal subspaces: (1) the noise subspace which contains components from the noise process only, and (2) the signal subspace that contains the dominant speech signal, plus a certain amount of noise as well. The components in the noise subspace are deleted and the enhanced speech is estimated from the remaining components in the signal subspace.

The conventional linear acoustical model of speech [75] overlooks the inherent nonlinearity of speech production. Nonlinear analysis of speech signal discloses the chaos-like features in most phonemes, especially the voiced ones, despite the continuous speech possibly being highly non-deterministic and non-stationary [62, 77–80]. These facts call for nonlinear or linear/nonlinear hybrid models to characterize the nonlinearity in speech. The theory of time delay embedding seems a possible framework and various techniques based on it have been applied in speech analysis and processing, for example, synthesis of voiced sounds [81], classification of isolated phonemes [82], and speech enhancement with the LP method [25, 62]. However, the LP method is not so effective for speech contaminated by colored noise. Thus, it is desirable to extend the LP method to the case of speech corrupted by colored noise, not only providing an alternative method to speech enhancement, but also demonstrating a more general application of the technique based on the theory of time delay embedding, and thus possibly promoting new developments of this framework. In this chapter, the two-step extension of the LP method, proposed for chaotic time series, is adapted to enhance speech contaminated by colored noise. This extension assumes that the colored noise is stationary, and thus the covariance matrix of colored noise

can be estimated with speech silence frames.

## 3.2 A two-step extension of the local projection method

For the LP method, the signal subspace  $\mathbf{U}_1 = [\mathbf{u}_1, \dots, \mathbf{u}_M]$  is first estimated by performing eigenvalue decomposition to the covariance matrix of neighborhood, i.e.,  $\hat{\mathbf{C}}_n = \frac{1}{N} \sum_{\mathbf{s}(k) \in \mathcal{N}_n} [\mathbf{s}(k) - \bar{\mathbf{s}}(n)][\mathbf{s}(k) - \bar{\mathbf{s}}(n)]^T$ , where  $\mathbf{u}_i$  is the eigenvector associated with the  $i$ th largest eigenvalue of matrix  $\hat{\mathbf{C}}_n$ . Then the enhanced version of the reference phase point is  $\hat{\mathbf{x}}(n) = \bar{\mathbf{s}}(n) + \mathbf{U}_1 \mathbf{U}_1^T [\mathbf{s}(n) - \bar{\mathbf{s}}(n)]$  (see Sec. 2.2 for more details). To get good performance, the signal subspace should be estimated appropriately. As to be demonstrated below, for the case with white noise, the signal subspace estimated by this way is suitable, but for the case with colored noise, it is no longer appropriate.

Let  $\mathbf{U}_t = [\mathbf{u}_1, \mathbf{u}_2, \dots, \mathbf{u}_{m_t}]$  span a subspace of the local phase space that is to be investigated, where  $m_t$  is the dimension of this subspace. For the reference phase point  $\mathbf{s}(n)$ ,  $\mathbf{s}(n) - \bar{\mathbf{s}}(n)$  can be written as the addition of two parts, i.e.,  $\mathbf{s}(n) - \bar{\mathbf{s}}(n) = [\mathbf{x}(n) - \bar{\mathbf{s}}(n)] + \mathbf{w}(n)$ . Then in the local phase space, i.e., the  $\varepsilon$ -neighborhood  $\mathcal{N}_n$  of  $\mathbf{s}(n)$ ,  $\|\mathbf{u}_i \mathbf{u}_i^T [\mathbf{x}(n) - \bar{\mathbf{s}}(n)]\|^2$  and  $\|\mathbf{u}_i \mathbf{u}_i^T \mathbf{w}(n)\|^2$  can be considered as the energy of signal components and noise components projected onto direction  $\mathbf{u}_i$ , respectively<sup>3</sup>.

Assume the clean signal  $\{x(n)\}$  and the noise  $\{w(n)\}$  are known. Here a sequence (10 000 points) measured from the  $x$  component of the Lorenz system [1]

$$\begin{cases} \dot{x} = \sigma(y - x), \\ \dot{y} = (r - z)x - y, \\ \dot{z} = xy - bz, \end{cases} \quad (3.1)$$

is taken as the clean signal  $\{x(n)\}$ , where  $(\sigma, r, b) = (10, 28, 8/3)$  and sampling interval  $\Delta t = 0.04$ . The white noise  $\{w(n)\}$  is with zero mean and follows

<sup>3</sup>Here we just investigate the energy of the components after removing the geometric center of the  $\varepsilon$ -neighborhood in the local phase space, so  $\|\mathbf{u}_i \mathbf{u}_i^T [\mathbf{x}(n) - \bar{\mathbf{s}}(n)]\|^2$  is not the absolute energy of the clean signal vector on direction  $\mathbf{u}_i$ .

the normal distribution. Then for the noisy Lorenz time series  $\{s(n)\}$ ,  $s(n) = x(n) + w(n)$ , two cases are studied.

Case 1: The subspace  $\mathbf{U}_t$  is estimated by the energy of clean signal, i.e., the covariance matrix is estimated by  $\hat{\mathbf{C}}_n = \frac{1}{N} \sum_{\mathbf{s}(k) \in \mathcal{N}_n} [\mathbf{x}(k) - \bar{\mathbf{x}}(n)][\mathbf{x}(k) - \bar{\mathbf{x}}(n)]^T$ , where  $\bar{\mathbf{x}}(n) = \frac{1}{N} \sum_{\mathbf{s}(k) \in \mathcal{N}_n} \mathbf{x}(k)$ . As Fig. 3.1(a) indicates, the energy of the projections of the clean signal vector on the first several directions, i.e.,  $\|\mathbf{u}_i \mathbf{u}_i^T [\mathbf{x}(n) - \bar{\mathbf{s}}(n)]\|^2$ , is much larger than that of white noise. And the energy of white noise is almost projected onto each direction uniformly.

Case 2: The subspace  $\mathbf{U}_t$  is estimated by the energy of noisy signal, i.e., for the reference phase vector  $\mathbf{s}(n)$ , the covariance matrix is estimated by  $\hat{\mathbf{C}}_n = \frac{1}{N} \sum_{\mathbf{s}(k) \in \mathcal{N}_n} [\mathbf{s}(k) - \bar{\mathbf{s}}(n)][\mathbf{s}(k) - \bar{\mathbf{s}}(n)]^T$ . As Fig. 3.1(b) indicates, the energy of the projections of clean signal vector on the first several directions is larger than that of white noise, which is similar to Case 1. This implies that the LP method can appropriately estimate the signal subspace by the energy of noisy data in the local phase space, because the energy of white noise is almost uniformly distributed on each direction. Moreover, it has been verified by the performance of LP for chaotic data with white noise.

Further, three cases for chaotic time series with colored noise are studied. The colored noise is generated from a third-order autoregressive process [AR(3)],  $w(n) = 0.8w(n-1) - 0.5w(n-2) + 0.6w(n-3) + \epsilon(n)$ , where  $\epsilon(n) \sim N(0, 1)$  follows the normal distribution.

Case 3: The subspace  $\mathbf{U}_t$  is estimated by the energy of clean signal, just as Case 1 does. As Fig. 3.1(c) indicates, the energy of colored noise vector  $\mathbf{w}(n)$  is not uniformly projected onto each direction.

Case 4: The subspace  $\mathbf{U}_t$  is estimated by the energy of colored noise, i.e., the covariance matrix is estimated by  $\hat{\mathbf{C}}_n = \frac{1}{N} \sum_{\mathbf{s}(k) \in \mathcal{N}_n} [\mathbf{w}(k) - \bar{\mathbf{w}}(n)][\mathbf{w}(k) - \bar{\mathbf{w}}(n)]^T$ , where  $\bar{\mathbf{w}}(n) = \frac{1}{N} \sum_{\mathbf{s}(k) \in \mathcal{N}_n} \mathbf{w}(k)$ . As Fig. 3.1(d) indicates, the energy of the colored noise vector  $\mathbf{w}(n)$  is mainly projected onto the first several directions, and only a certain, relatively small, amount of signal components are projected onto these directions, respectively. So a noise

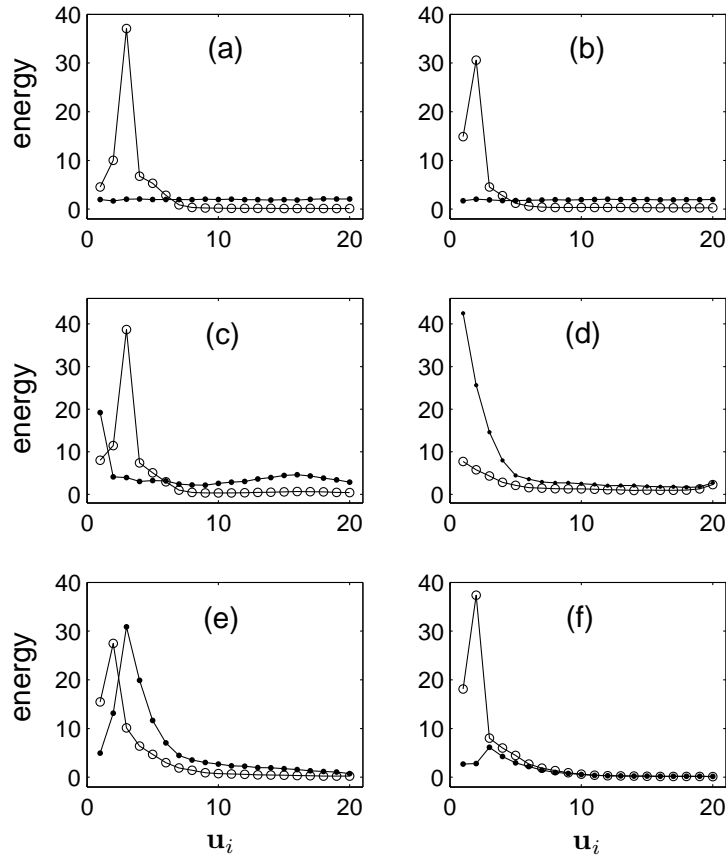


Figure 3.1: Energy of the projection of clean signal vector and noise vector in the local phase space. For each case, the signal-to-noise ratio (SNR) is 15 dB, the 20 nearest neighbors of each reference phase point are utilized, and only the average energy of the components projected onto the first 20 directions is plotted.  $\circ$  —  $E(\|\mathbf{u}_i \mathbf{u}_i^T [\mathbf{x}(n) - \bar{\mathbf{s}}(n)]\|^2)$ ;  $\bullet$  —  $E(\|\mathbf{u}_i \mathbf{u}_i^T \mathbf{w}(n)\|^2)$ , here  $E(\|\mathbf{u}_i \mathbf{u}_i^T \mathbf{w}(n)\|^2)$  denotes the mean of  $\|\mathbf{u}_i \mathbf{u}_i^T \mathbf{w}(n)\|^2$  over  $n = (d-1)\kappa, \dots, L-1$ . (a) Case 1, with white noise; (b) Case 2, with white noise; (c) Case 3, with AR(3) noise; (d) Case 4, with AR(3) noise; (e) Case 5, with AR(3) noise; (f) Case 6, the output of step 1.

dominated subspace can be estimated in this way, and most of noise components can be reduced by eliminating the components projected into this subspace at the price of relatively small signal distortion.

Case 5: The subspace  $\mathbf{U}_t$  is estimated by the energy of noisy signal, as Case 2 does. As Fig. 3.1(e) indicates, a certain, large, amount of noise components are projected into the subspace spanned by the first several directions. The LP method estimates the signal subspace by the energy of the noisy signal,

and thus cannot reduce colored noise effectively by projection, because a large amount of noise components are projected into the so estimated signal subspace.

With the above observations, the first step of the proposed extension follows.

*Step 1.* First, estimate the noise dominated subspace  $\mathbf{U}_{nd}$  by performing eigenvalue decomposition to the covariance matrix  $\hat{\mathbf{C}}_{noise}$  of colored noise. Note that this covariance matrix is estimated from a noise sequence obtained in advance. With the assumption that the noise process is stationary, this covariance matrix can be used to substitute the one in Case 4. Then in each local phase space, i.e., the  $\varepsilon$ -neighborhood, the components projected into the noise dominated subspace are deleted and the enhanced phase vector is reconstructed with the remaining components, i.e.,

$$\hat{\mathbf{x}}(n) = \bar{\mathbf{s}}(n) + (\mathbf{I} - \mathbf{U}_{nd}\mathbf{U}_{nd}^T)[\mathbf{s}(n) - \bar{\mathbf{s}}(n)], \quad (3.2)$$

where  $\mathbf{I}$  is identity matrix.

After step 1, the noise components projected into the noise dominated subspace have been eliminated. The energy of residual error (i.e., the difference between the clean signal and the output of step 1) tends to distribute “uniformly” on each direction. This can be confirmed as follows.

Case 6: The subspace  $\mathbf{U}_t$  is estimated by the energy of the output of step 1, as Case 2 does. As Fig. 3.1(f) indicates, the energy of the projection of clean signal vector on the first several directions is much larger than that of residual error. The energy of residual error is more “uniformly” distributed compared with Case 5, and is similar to Case 2.

With this observation, the second step of the proposed extension follows.

*Step 2.* Treat the residual error after step 1 as white noise, and apply the LP method to the output of step 1.

### 3.3 Applications to noisy chaotic time series

The two-step extension of LP is applied to the Lorenz time series which are contaminated by colored noise. It has been argued that the LP method can obtain better results by over-embedding with time delay  $\kappa = 1$  and an appropriately longer embedding window [25, 57, 62]. While the embedding window cannot be set too long, otherwise there are not enough appropriate neighbors for the reference phase point<sup>4</sup>. Thus a tradeoff of the length of embedding window should be made. Here, parameters are set as  $(d, \kappa) = (80, 1)$ , and the first 20 nearest neighbors are used for each reference phase point. The covariance matrix  $\hat{\mathbf{C}}_{noise}$  of colored noise is estimated with 20 nonoverlapped noise sequences. Each sequence has  $(d-1)\kappa+1$  points, which is equal to the length of embedding window. Note that these noise sequences are not the noise sequences that are added to the Lorenz time series.

With eigenvalue decomposition to  $\hat{\mathbf{C}}_{noise}$ , the noise dominated subspace  $\mathbf{U}_{nd} = [\mathbf{u}_1, \mathbf{u}_2, \dots, \mathbf{u}_{m_w}]$ , spanned by the eigenvectors associated with the  $m_w$  largest eigenvalues, can be obtained, where  $m_w$  is the dimension of the noise dominated subspace and its value is set by numerical study. At the first step, as  $m_w$  decreases below 15, the performance becomes worse, because the energy of the projection of noise on each direction  $\mathbf{u}_i$  ( $1 \leq i \leq 15$ ) is bigger than that of the clean signal, while as  $m_w$  increases above 15, the performance varies little, because the energy of the projection of noise on each direction  $\mathbf{u}_i$  ( $15 < i \leq 20$ ) is almost equal to that of the clean signal. For data with high level noise,  $m_w$  should be set a little bigger. For simplicity, we set  $m_w = 20$  for all cases. The LP method is performed for comparison<sup>5</sup>. The parameters of LP are set

<sup>4</sup>Here ‘‘appropriate neighbors’’ mean that the wave forms of the data segments covered by the neighbors match that of the reference phase point well, see more discussions in Chapter 4.

<sup>5</sup>Note that the linear subspace techniques have suggested a whitening-dewhitening strategy for the signal contaminated by colored noise [63]. With this strategy, chaotic time series with colored noise can be first whitened by multiplying a whitening matrix  $\mathbf{C}_w^{-1/2}$ , where  $\mathbf{C}_w$  is the covariance matrix of the colored noise. Then the whitened data can be processed as the case of white noise. Finally, a dewhitening procedure is performed. The enhanced signal vector can be expressed as

$$\hat{\mathbf{x}}(n) = \bar{\mathbf{s}}(n) + \mathbf{C}_w^{1/2} \mathbf{U}_1 \mathbf{U}_1^T \mathbf{C}_w^{-1/2} [\mathbf{s}(n) - \bar{\mathbf{s}}(n)]. \quad (3.3)$$

However, Eq. (3.3) is difficult to implement, because with 20 segments of noise data and 80 dimensional embedding, the estimated covariance matrix  $\hat{\mathbf{C}}_w$  will be rank-deficient and matrix  $\hat{\mathbf{C}}_w^{-1/2}$  cannot be properly obtained.

as  $(N, d, \kappa, M) = (20, 80, 1, 8)$ , where  $M$  is set a value relatively bigger than the minimum embedding dimension so as to control the introduced signal distortion at a small level. Note that the local subspace method [26] has also been applied to chaotic time series with colored noise, but the results are not better than that of the LP method. The method proposed by Luo *et al.* [64] has been applied as well, but as they had reported, the performance for chaotic time series with colored noise is poor. So we do not present the results of these two methods here.

As Fig. 3.2 indicates, most colored noise is deleted after step 2 and the introduced distortion is much smaller than that induced by the LP method. As Fig. 3.3 indicates, this is more obvious in the reconstructed phase space. A more comprehensive comparison is summarized in Table 3.1. The two-step extension obtains significant SNR gains, outperforming the LP method much for the Lorenz time series which is contaminated by the AR(3) noise.

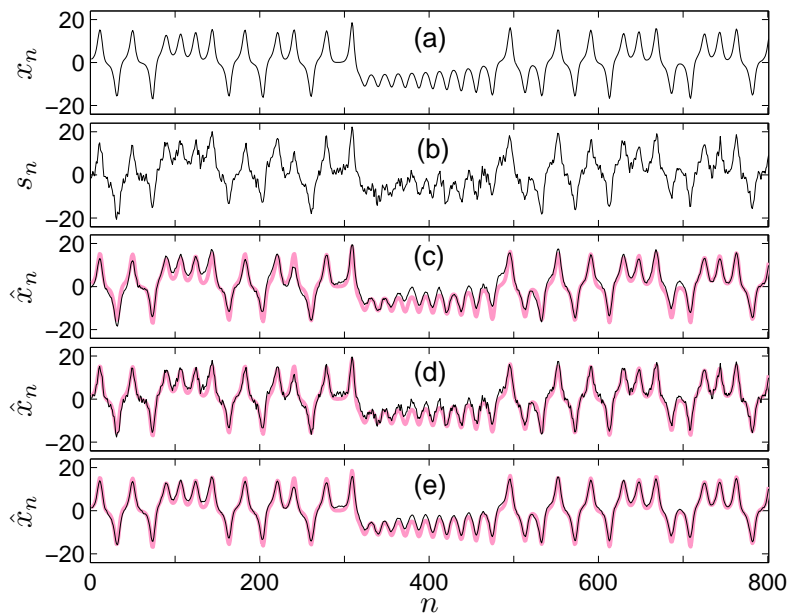


Figure 3.2: Wave forms of (noisy) Lorenz time series. The thin black curves in panels (a), (b), (c), (d), and (e) are the wave forms of the clean Lorenz time series, the noisy time series with 10 dB AR(3) noise, the enhanced data by the LP method, the output of step 1, and the output of step 2 of the extension, respectively. For comparison, the wave form of clean data in panel (a) is plotted with thick curves in panels (c), (d), and (e), respectively.

The two-step extension is further tested with two other typical colored noise.

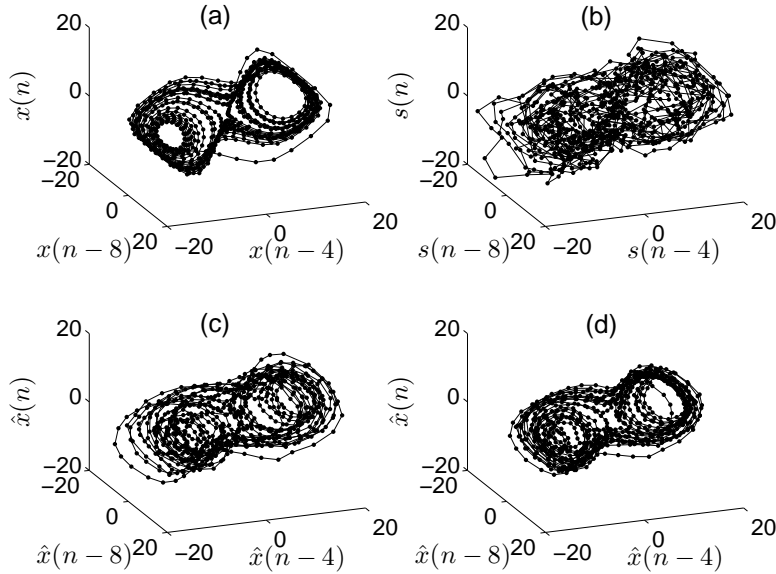


Figure 3.3: The Lorenz attractors reconstructed by time delay embedding with  $\kappa = 4$ . The data used in panels (a), (b), (c), and (d) are the same data that are used in Figs. 3.2(a), 3.2(b), 3.2(c), and 3.2(e), respectively.

Table 3.1: Results of noise reduction for the Lorenz time series contaminated by colored noise generated by AR(3). Ten sequences (each 10 000 points) are measured from the  $x$  components of the Lorenz system with the same parameters but different initial condition. The four columns from left to right are the SNRs of the original noisy data, the output of step 1, the output of step 2, and the enhanced data by the LP method, respectively.

Noisy data (dB)	step-1 (dB)	step-2 (dB)	LP (dB)
15	19.47±0.14	21.91±0.31	16.98±0.46
10	13.86±0.10	16.49±0.57	12.14±0.57
5	7.70±0.10	9.85±0.55	7.15±0.63

One is pink noise, which is generated by a model proposed to explain the physics of  $1/f$  noise [67, 83]. The surrogate data, generated by shuffling the phase of the original Lorenz time series [84], is taken as another noise. The surrogate data has almost the same power spectra of the original time series but do not possess the corresponding deterministic structure of the original data. Note that it is difficult to separate the pink noise and the phase shuffled data, as well as the AR(3) noise, from the Lorenz time series in the frequency domain, because their

spectra extensively overlap in the low frequency region, as Fig. 3.4 indicates. However, the two-step extension works well for the Lorenz time series with pink noise and phase shuffled surrogate data, as Tables 3.2 and 3.3 indicate. For the case with phase shuffled surrogate data, a good result can be obtained even with only the first step of the proposed extension.

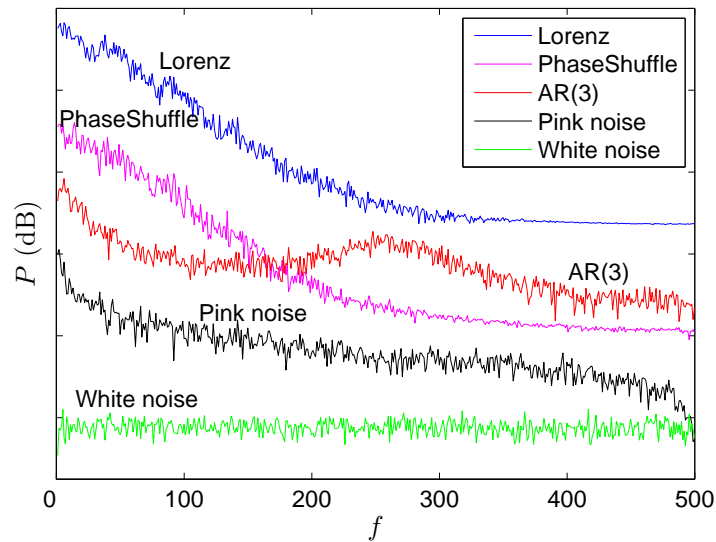


Figure 3.4: The power spectra of a Lorenz time series, phase shuffled surrogate data of the Lorenz times series, AR(3) noise, pink noise, and white Gaussian noise. Each data have 10 000 samples, and their spectra are estimated by the periodogram averaging method [67], that is, the data are divided into 10 blocks (each block has 1000 samples), the spectra of each block are estimated by periodogram, and the average of the spectra of these blocks are taken as the final spectra. The spectra are offset vertically for clarity, and the scale in the vertical axis is therefore arbitrary.

Table 3.2: Results of noise reduction for the Lorenz time series (ten sequences, each 10 000 points) contaminated by pink noise.

Noisy data (dB)	step-1 (dB)	step-2 (dB)	LP (dB)
15	19.40±0.23	20.32±0.30	15.80±0.08
10	13.65±0.18	14.40±0.26	10.85±0.09
5	7.44±0.14	8.03±0.21	5.85±0.97

The proposed extension has also been tested with the contaminated Rössler time series (measured from the  $x$  component of the Rössler system [85] with

Table 3.3: Results of noise reduction for the Lorenz time series (ten sequences, each 10 000 points) contaminated by its phase shuffled surrogate data.

3mm

Noisy data (dB)	step-1 (dB)	step-2 (dB)	LP (dB)
15	20.21±0.45	20.24±0.44	15.24±0.04
10	14.97±0.33	14.97±0.33	10.22±0.04
5	8.23±0.23	8.23±0.23	5.09±0.02

sampling interval  $\Delta t = 0.2$ ), and about 3–5 dB SNR gains can be obtained for different noise levels.

## 3.4 Applications to noisy speech signals

The two-step extension of LP is first tested with noisy vowels, and further adapted to continuous speech signals which are contaminated by environmental noise.

### 3.4.1 Application to vowels

The energy distribution of speech signals and noise measured in running car (from AURORA [86]) in the local phase space is first examined. The speech signal of vowel /a/, recorded with 8 kHz sampling rate, is taken as a example. As that does in Sec. 3.2, the results of six cases are given in Fig. 3.5, respectively.

Case 1: Speech is contaminated by white Gaussian noise, and direction  $\mathbf{u}_i$  is estimated by the clean speech. As Fig. 3.5(a) indicates, the energy of the projection of clean vowel /a/ on the first several directions is much larger than that of white noise, and white noise is almost uniformly distributed on each direction.

Case 2: Speech is contaminated by white Gaussian noise, and direction  $\mathbf{u}_i$  is estimated by the noisy speech. As Fig. 3.5(b) indicates, the energy of the

projection of clean vowel /a/ on the first several directions is much larger than that of white noise, which is similar to Case 1.

- Case 3: Speech is contaminated by car noise, and direction  $\mathbf{u}_i$  is estimated by the clean speech. As Fig. 3.5(c) indicates, both the clean vowel /a/ and car noise are mainly projected on the first several directions.
- Case 4: Speech is contaminated by car noise, and direction  $\mathbf{u}_i$  is estimated by the car noise. As Fig. 3.5(d) indicates, the car noise is mainly projected onto the first several directions, and a certain, relatively small, amount of speech components are projected onto these directions as well. If the components in the *noise dominated subspace* are deleted, then most of the noise components can be reduced at the expense of a relatively small speech distortion.
- Case 5: Speech is contaminated by car noise, and direction  $\mathbf{u}_i$  is estimated by the noisy speech. As Fig. 3.5(e) indicates, a large amount of noise components are projected on the first several directions. The LP method adopts the first several directions, estimated in this way, as the signal subspace, and thus can not reduce the noise effectively.
- Case 6: Speech is contaminated by car noise, and direction  $\mathbf{u}_i$  is estimated by the the output of step 1. That is, the output of step 1,  $\{\hat{s}_n^{(1)}\}$ , is taken as the input of step 2, and direction  $\mathbf{u}_i$  is estimated as Case 2 does. As Fig. 3.5(f) indicates, the energy of clean speech on the first several directions is much larger than that of residual error. The energy of residual error is more “uniformly” distributed compared with Case 5.

With the above observations, the two-step extension, proposed in Sec. 3.2, is expected to be applicable to speech signals which are contaminated by colored noise. This is verified by applying the extension to ten speech sequences added with environmental noise measured in a running car. Five vowels, /a/, /e/, /i/, /o/, and /u/, are articulated at normal speed by one male speaker and one female speaker respectively, and the clean speech sequences are recorded with 8 kHz sampling rate and 16 bits quantization. As the results summarized in Table 3.4, the two-step extension yields better enhancements than the LP method.

Ideally, speech only resides in a low dimensional subspace. However, in practical application, the estimated direction is not a perfect estimate, but just

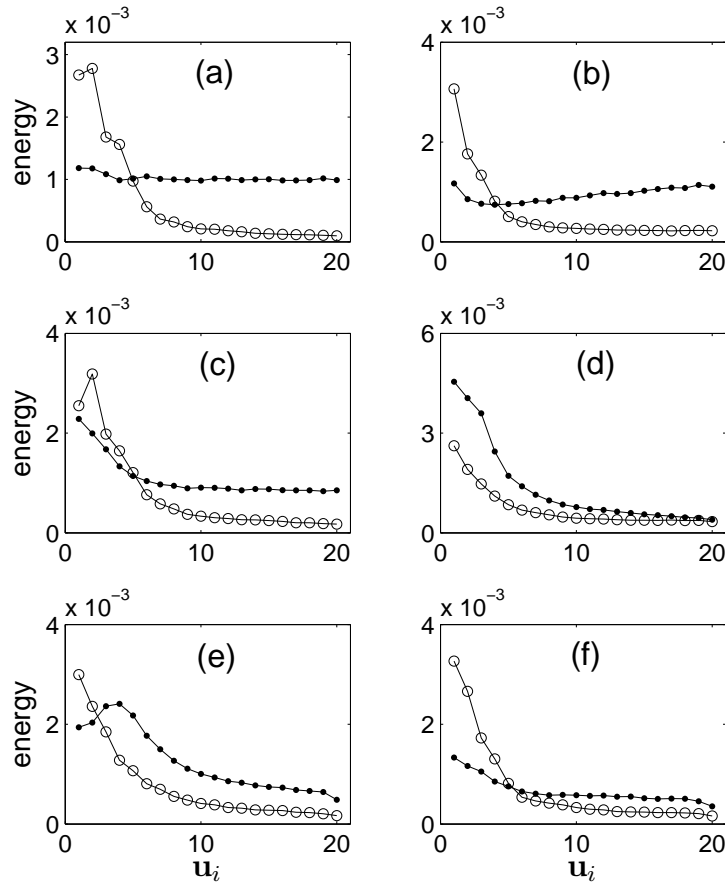


Figure 3.5: Energy distribution of vowel /a/ and car noise (10 dB) in the local phase space. 20 neighbors are utilized, and thus only the energy distribution on the first 20 directions is plotted.  $\circ$  —  $E(\|\mathbf{u}_i \mathbf{u}_i^T [\mathbf{x}(n) - \bar{\mathbf{z}}(n)]\|^2)$ , denotes the mean of  $\|\mathbf{u}_i \mathbf{u}_i^T [\mathbf{x}(n) - \bar{\mathbf{z}}(n)]\|^2$  over  $n = (d-1)\kappa, \dots, L-1$ ;  $\bullet$  —  $E(\|\mathbf{u}_i \mathbf{u}_i^T \mathbf{w}(n)\|^2)$ . (a) Case 1, speech with white noise; (b) Case 2, speech with white noise; (c) Case 3, speech with car noise; (d) Case 4, speech with car noise; (e) Case 5, speech with car noise; and (f) Case 6, the output of step 1 (for this case, the residual error  $[\hat{x}^{(1)}(n) - x(n)]$  is considered as noise).

an approximation to the desired direction. Speech components will extend to all the estimated directions, and thus speech distortion will be introduced both at step 1 and step 2. At step 1, speech distortion is introduced when all the components in the noise dominated subspace, which includes some speech components [Fig. 3.5(d)], are removed; and at step 2, speech distortion is introduced when all those in the noise subspace, which also have some speech components [Fig. 3.5(f)], are eliminated. The proposed method, as well as other methods, is

Table 3.4: Results of noise reduction for the speech corrupted by environmental noise measured in running car.

Noisy data (dB)	step-1 (dB)	step-2 (dB)	LP (dB)
15	18.72±0.80	19.51±1.28	17.92±0.66
10	13.73±0.60	15.80±0.75	13.20±0.58
5	8.10±0.54	10.68±0.97	8.21±0.61

a tradeoff between speech distortion and noise reduction, and is expected to obtain much larger noise reduction than the introduced distortion with appropriate parameter settings.

### 3.4.2 Enhancement of continuous speech

#### 3.4.2.1 The speech database

To investigate the effectiveness of the proposed extension in more general application, it is tested with speech data from the NOIZEUS database [87]<sup>6</sup>, which is designed for comparison of speech enhancement. NOIZEUS includes 30 IEEE sentences [88] articulated by three male and three female speaker (5 sentences/speaker), respectively. The articulation of each sentence is recorded at 25 kHz and further downsampled to 8 kHz. Eight different noise signals [86], recorded in real environments, are added to the clean speech signals to generated noisy speech signals. Ten speech sentences are selected from NOIZEUS for experiment. Three male and three female speakers are involved, and at most two sentences articulated by each speaker are adopted.

#### 3.4.2.2 Implementation

As discussed in Ref. [62], for phase point  $s(n)$ , the most useful information is contained by the phonemes or syllables that  $s(n)$  belongs to, i.e., only intra-phoneme neighbors are needed. In general, the duration of an individual phoneme is less than 100 ms. So an overlap-add strategy is utilized, and speech

<sup>6</sup>Available at: <http://www.utdallas.edu/~loizou/speech/noizeus/>.

is divided into frames of 100 ms with 3/4 overlapping, as Fig. 3.6 indicates. For data recorded with 8 kHz sampling rate, each frame has 800 samples<sup>7</sup>. For each frame, the reference phase points at the beginning and end sections will miss some intra-phoneme neighbors that locate outside of this frame, while the reference phase points at the middle sections can include almost all intra-phoneme neighbors. Each frame can be enhanced separately<sup>8</sup>, and the whole speech can be reconstructed by overlap-adding of the middle section (from 201 to 600) of each enhanced frame with triangular window.

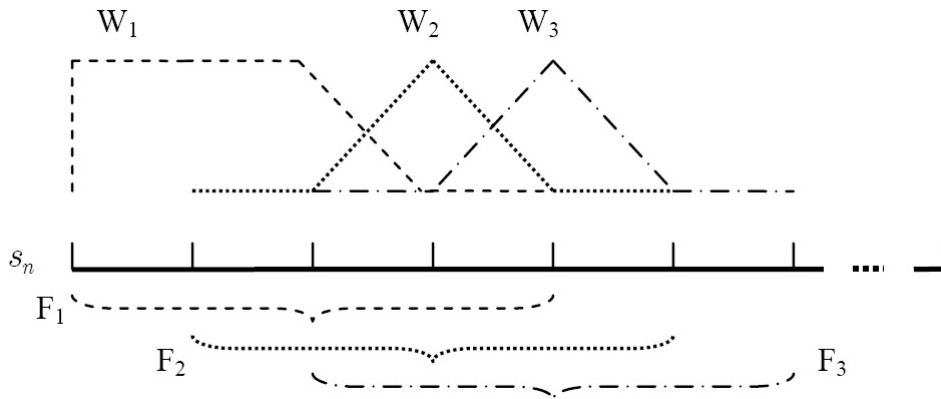


Figure 3.6: Overlap-adding reconstruction of enhanced speech.  $F_1$ ,  $F_2$ , and  $F_3$  denote the first three frames, respectively;  $W_1$ ,  $W_2$ , and  $W_3$  are the windows corresponding to frames  $F_1$ ,  $F_2$ , and  $F_3$ , respectively. For each  $L_f$ -sample frame, only the middle section,  $[\frac{1}{4}L_f + 1, \frac{3}{4}L_f]$ , is used to reconstruct the continuous speech by overlap-adding with triangular window.

The beginning segment (600 samples) of each sentence is speech silence, and is thus taken as noise  $\{w(n)\}$ . The covariance matrix of noise can be estimated as  $\hat{\mathbf{C}}_{noise} = \frac{1}{N} \sum_{k=1}^N \mathbf{w}[(k-1)d\kappa + 1] \mathbf{w}[(k-1)d\kappa + 1]^T$ , where  $\mathbf{w}(n) = [\underline{w}(n), \underline{w}(n + \kappa), \dots, \underline{w}(n + (d-1)\kappa)]^T$ ,  $\underline{w}(n) = w(n) - \bar{w}$ , and  $\bar{w}$  is the average of  $\{w(n)\}$ . Here,  $\hat{\mathbf{C}}_{noise}$  is estimated in an analogous way with the estimation of  $\hat{\mathbf{C}}_n$  in Case 4. Then the noise dominated subspace is spanned by  $\mathbf{U}_{nd} = [\mathbf{u}_1, \mathbf{u}_2, \dots, \mathbf{u}_K]$ , where  $\mathbf{u}_i$  is the eigenvector associated with the  $i$ th largest eigenvalue of  $\hat{\mathbf{C}}_{noise}$ , and  $K$  is the dimension of the noise dominated subspace.

<sup>7</sup>Frame length of 1200 and 1600 samples have also been tried, and the results vary little.

<sup>8</sup>By dividing the continuous speech into frames, neighbors searching can be implemented via an efficient box-assisted approach [11].

For each frame, the data are embedded first. At step 1, the reference point  $\mathbf{s}(n)$  is enhanced via Eq. (3.2), i.e.,  $\hat{\mathbf{x}}^{(1)}(n) = \bar{\mathbf{s}}(n) + (\mathbf{I} - \mathbf{U}_{nd}\mathbf{U}_{nd}^T)[\mathbf{s}(n) - \bar{\mathbf{s}}(n)]$ , where  $\bar{\mathbf{s}}(n) = \frac{1}{N} \sum_{\mathbf{s}(k) \in \mathcal{N}_n} \mathbf{s}(k)$ . As  $s(n)$  occurs as an entry of  $\mathbf{s}(i)$ ,  $i = n, \dots, n + (d - 1)\kappa$ , there are  $d$  enhancements for  $s(n)$ . Let  $\hat{\mathbf{x}}^{(1)}(i; j)$  denote the  $j$ th entry of vector  $\hat{\mathbf{x}}^{(1)}(i)$ , and define set  $\mathcal{X}_n = \{\hat{\mathbf{x}}^{(1)}(i; j) | i - (j - 1)\kappa = n, 1 \leq j \leq d\}$ , which collects those enhancements of  $x(n)$ . Then the average of the elements in set  $\mathcal{X}_n$  is taken as the final enhancement  $\hat{x}^{(1)}(n)$ . The the enhancements of frames are overlap-added into continuous speech  $\{\hat{x}^{(1)}(n)\}$ . At step 2, the output of step 1,  $\{\hat{x}^{(1)}(n)\}$ , is taken as the input, and one iteration of the LP method is applied to it via Eq. (2.9).

### 3.4.2.3 Results

The proposed extension is tested with speech corrupted by different types of environmental noise [86]. The parameters are set as:  $N = 20$ ,  $d = 30$ ,  $\kappa = 1$ ,  $K = 6$ , and  $M = 5$ . Parameter  $d$  is empirically set as  $d = 30$ , which is smaller than that in Ref. [62], because the speech data are recorded with 8 kHz sampling rate, which is smaller than the sampling rate (24 kHz) in Ref. [62]. A typical linear subspace method (linSS) [76] which is designed for colored noise, and a minimum mean-square error method with log-spectral amplitude estimator (logMMSE) [89] are performed for comparison. Signal-to-noise ratio (SNR), segmental SNR (segSNR) [90], and four other objective measures are utilized to evaluate the proposed extension. Recently, several popular objective measures for speech enhancement are evaluated by the correlations between the results of objective measures and the results of subjective tests [91]. The measure PESQ of ITU-T recommendation [92] is shown to be one of the best of the evaluated measures. Further, Ref. [91] analyzes all the results of objective measures by multiple linear regression and proposes three composite measures: (1) the measure  $C_{sig}$  for signal distortion, (2) the measure  $C_{bak}$  for noise distortion, and (3) the measure  $C_{ovl}$  for overall quality. These composite measures have been used to evaluate 13 different speech enhancement algorithms [87]. The results show that linSS is the better of the two evaluated subspace methods, and logMMSE is the best of all the 13 methods.

The results of speech with two typical noise realizations, i.e., noise recorded

in running car and in street, are summarized in Tables 3.5 and 3.6, respectively. The proposed extension can obtain larger SNR gains than the LP method. Comparing with linSS and logMMSE, the proposed extension obtains larger SNR gains for speech with street noise, but smaller SNR gains for speech with car noise. The wave forms and segSNRs of each case are illustrated in Figs. 3.7 and 3.8, respectively. For speech science and some consonant frames, linSS almost removes all components and thus obtains higher SNR, while for sounds with deterministic structure, such as vowels and semivowels, the proposed extension gets better results than both linSS and logMMSE. Fig. 3.9 illustrates the results of four objective measures. In the sense of these measures, the proposed extension is better than logMMSE for the case of street noise, and is inferior to logMMSE for the case of car noise, while it is superior to linSS for the cases of both car noise and street noise. It is surprising that linSS even degrades the quality of speech in the sense of these measures, which may be due to its over-reduction at some frames [Fig. 3.7(d)]. For noisy speech of 10 dB input SNR, the proposed extension is not as effective as the case with high noise level, because the amount of introduced speech distortion is almost comparable to that of the reduced noise when the noise level is low. Note that the proposed extension has also been tested with other noise from AURORA [86], and the results are positive. For noisy speech of 0 dB input SNR, different SNR gains, ranging from 2.4 dB to 5.0 dB, are obtained; for noisy speech of 5 dB input SNR, about 2.1 – 4.3 dB SNR gains are obtained.

Table 3.5: Results of speech enhancement for ten speech sentences corrupted by car noise. The six columns from left to right are the SNRs (mean  $\pm$  standard deviation) (dB) of the original noisy speech, the output of step 1, the output of step 2, the result by LP, by linSS, and by logMMSE, respectively.

noisy speech	step-1	step-2	LP	linSS	logMMSE
10.0	10.7 $\pm$ 0.4	11.3 $\pm$ 1.1	11.2 $\pm$ 0.9	12.4 $\pm$ 0.9	12.4 $\pm$ 0.4
5.0	6.4 $\pm$ 0.2	8.6 $\pm$ 0.7	7.1 $\pm$ 0.6	9.3 $\pm$ 0.6	9.4 $\pm$ 0.5
0.0	1.5 $\pm$ 0.3	4.4 $\pm$ 0.6	2.3 $\pm$ 0.7	5.1 $\pm$ 1.3	5.8 $\pm$ 0.8

Table 3.6: Results of speech enhancement for ten speech sentences corrupted by street noise. The results are evaluated with SNR (dB).

noisy speech	step-1	step-2	LP	linSS	logMMSE
10.0	$10.4 \pm 0.3$	$11.2 \pm 0.7$	$11.6 \pm 0.9$	$10.7 \pm 1.6$	$10.8 \pm 0.9$
5.0	$6.0 \pm 0.2$	$8.2 \pm 1.1$	$7.6 \pm 1.1$	$6.7 \pm 0.8$	$7.1 \pm 0.5$
0.0	$1.0 \pm 0.3$	$3.9 \pm 1.2$	$2.9 \pm 1.2$	$2.8 \pm 1.8$	$3.2 \pm 1.8$

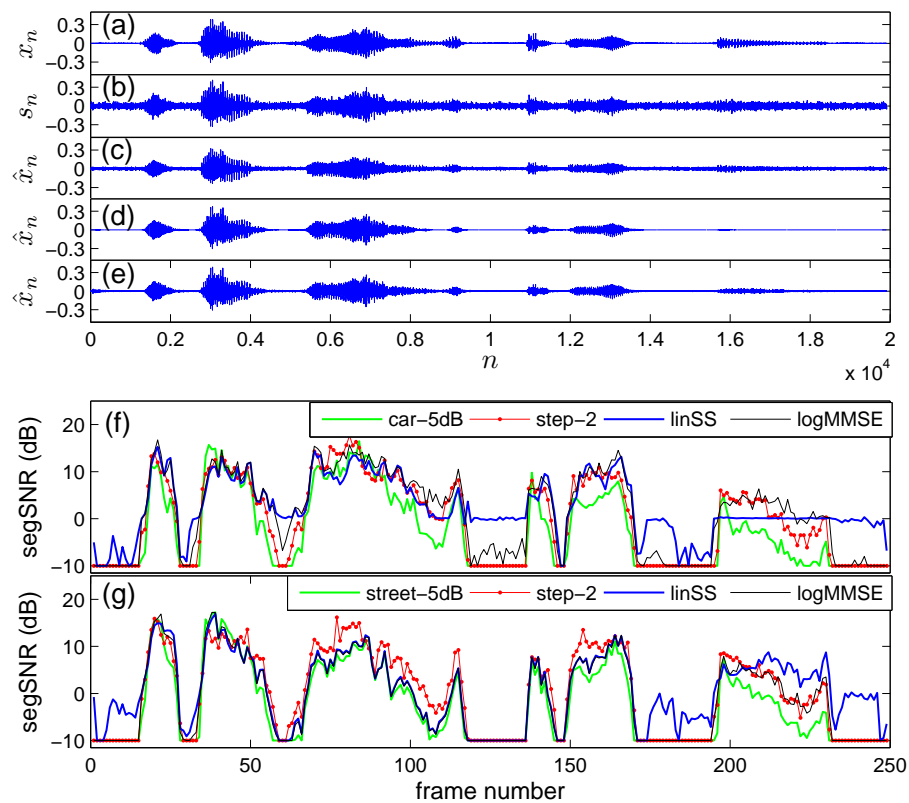


Figure 3.7: The wave forms of clean speech (a), noisy speech with 5 dB car noise (b), the output of step 2 (c), the result of linSS (d), and the result of logMMSE (e). The continuous speech is divided into segments of 80 samples and the SNR of each frame is plotted for the case of speech with 5 dB car noise (f), and the case of speech with 5 dB street noise (g), respectively.

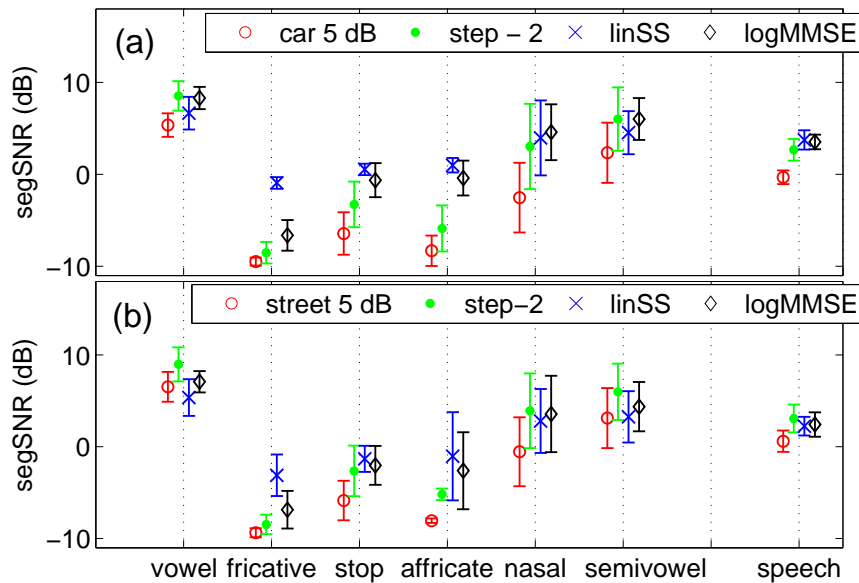


Figure 3.8: The segSNRs (means and standard deviations) of different classes of sounds for speech with 5 dB car noise (a), and with 5 dB street noise (b). The label “speech” denotes the segSNR of the speech present frames. The NOIZEUS [87] database contains phonetic transcription files which indicate the segmentation of six classes of sounds for every speech sentences.

### 3.5 Discussion and conclusion

The energy distribution of Lorenz time series and AR(3) noise in the local phase space is first examined. For chaotic time series contaminated by white noise, it is appropriate to estimate the signal subspace by the energy distribution of noisy data, while for the case with colored noise, the signal subspace estimated by the energy of noisy data may include considerable noise projection, because the energy of colored noise is mainly distributed in a low dimensional subspace. With this observation, a two-step extension of the LP method is devised to reduce colored noise for chaotic time series. At step 1, a noise dominated subspace which contains most of noise components and a certain, small, amount of signal components is estimated by the energy distribution of colored noise. Then for each reference phase point, the components projected into the noise dominated subspace are eliminated and the enhanced phase point is reconstructed with the remaining components. After step 1, the energy of the residual error tends to

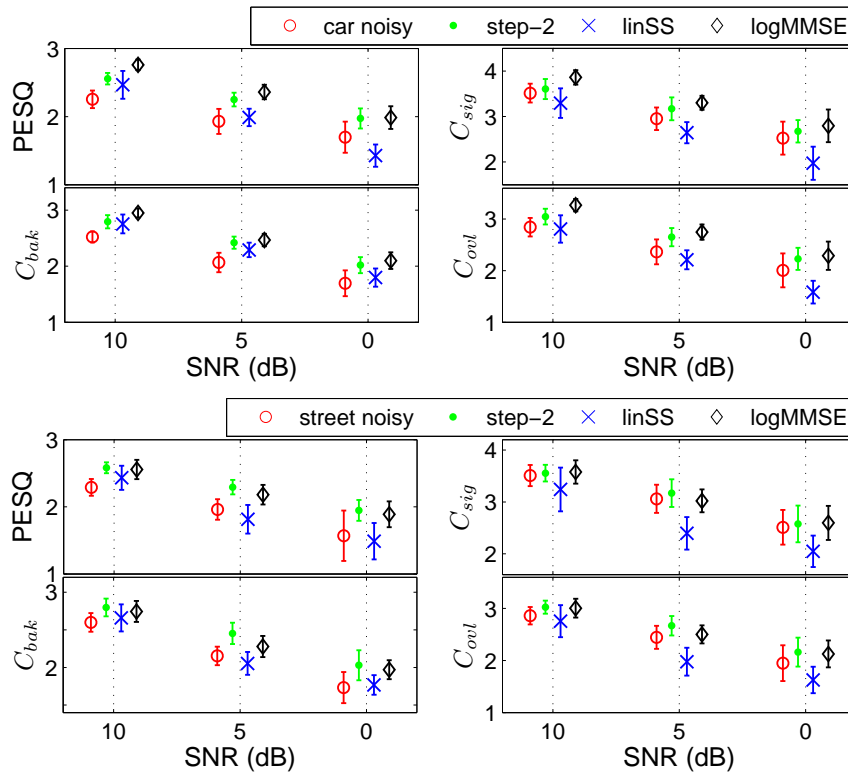


Figure 3.9: Evaluation of speech enhancement with four objective measures, i.e., PESQ,  $C_{sig}$ ,  $C_{bak}$ , and  $C_{ovl}$ , for speech with car noise and with street noise, respectively.

distribute uniformly on each direction. So at step 2, the residual error is treated as white noise and the LP method is applied to the output of step 1.

This two-step extension of LP is applied to the noisy Lorenz time series, and the noisy Rössler time series, which are contaminated by noise generated by an AR(3) process, pink noise, and a phase shuffled surrogate data, respectively. Numerical results show that the proposed extension can reduce colored noise significantly, and is superior to the LP method in reducing colored noise for noisy chaotic time series.

Further, the energy distribution of speech signal and noise recorded in running car in the local phase space is examined. Their energy distribution patterns are similar to that of chaotic Lorenz time series and AR(3) noise in a certain way. This implies that the two-step extension is also applicable to noisy speech sig-

nals. Then the extension is adapted to continuous speech which are contaminated by different environmental noise. Experimental results show that the proposed extension is more effective than the LP method, and is comparable to two typical speech enhancement methods. Adaption of this two-step extension to speech enhancement is of considerable significance in providing real application for the framework of time delay embedding, and thus possibly promoting its development.

Except application to speech signals, the LP method has also been applied to real data observed from other systems. For examples, the LP method can reduce the noise (about 5%) in the data measured from a Taylor-Couette flow experiment to be  $\frac{1}{4}$  of the original noise level [22]. For data observed from a NMR-laser experiment, the LP method can reduce the noise level from  $\frac{1}{64}$  to  $\frac{1}{2^{10}}$  of the attractor size [22]. The ECG signals show dynamical behavior which is neither periodic nor chaotic. It has been reported that the LP method can not only reduce the measurement noise in ECG signals [61] but also extract fetal ECG signals from maternal ECG signals with two round projections [27]. At the first round of LP, both the fetal ECG signals and the measurement noise are considered as noise and thus separated from the maternal ECG signals; after that, one more iteration of LP is applied to separate the fetal ECG signals from the measurement noise. These examples show that the LP method is applicable to data observed from real systems. For all these cases, the LP method assumes the measurement noise is white random noise. The two-step extension is proposed for the case with colored noise. It requires that a segment of noise data can be obtained in advance. However, for some cases (e.g., the extraction of fetal ECG signals), this requirement may be not satisfied, and thus the extension is not applicable.

Generally, time delay embedding can be considered as a transform from time domain to phase space. If the colored noise is mainly distributed in a certain noise subspace, and the signal is mainly distributed in a signal subspace which is orthogonal to the noise subspace, the noise can be reduced by eliminating the components in the noise subspace, just as the frequency domain methods filter the out-band spectra of noise. Some noise components are also, possibly, distributed in the same subspace of signal, and cannot be reduced, just as the frequency domain methods can not eliminate in-band noise effectively. So to say whether the

proposed extension is applicable to a certain contaminated signal, the analysis of energy distribution in the local phase space should be performed first. But the representation of signal in the local phase space is not so obvious as the representation in the frequency domain.



# Chapter 4

## Neighborhood-based time-frequency analysis

In this chapter, time-frequency analysis is performed for chaotic flow with a neighborhood-based spectrum estimator. The relation between the reference phase point and its nearest neighbors is demonstrated. The nearest neighbors, representing the state recurrences in the phase space reconstructed by time delay embedding, actually cover data segments with similar wave forms, but recur with no obvious temporal regularity. To utilize this redundant information presents in state recurrences, a neighborhood-based spectrum estimator is devised. Then time-frequency analysis with this estimator is performed for the Lorenz time series, the Rössler time series, experimental laser data, and colored noise. Features revealed by the spectrogram can be used to distinguish noisy chaotic flow from colored noise.

### 4.1 Introduction

In order to obtain the inherent properties of a dynamical system from the observed time series, a variety of methods have been proposed, such as surrogate tests [84, 93], wavelets [34], Fourier transforms [32, 33], and approaches based on time delay embedding [11]. Among them, the methods based on time delay

embedding may be the most popular and effective tools for chaotic time series. Based on Takens' embedding theory [7, 8], the measures such as Lyapunov exponents [3] and correlation dimension [9] have been proposed to characterize the global features of dynamical systems. However, few studies of the local time pattern of chaotic time series have been reported.

Spectral analysis provides an alternative framework for chaotic time series analysis [29–33]. With methods based on the Fourier transform, the relation between the spectra and the topology as the corresponding dynamical system bifurcates to chaos has been studied. Spectrum bands of some period-doubling bifurcation sequences (e.g., the Rössler time series) merge as the dynamical system bifurcates to chaos [31, 32]. Another typical spectrum of chaotic data (e.g., the Lorenz time series) is broadband and falls off via an exponential law. This spectrum falloff pattern has been utilized to distinguish chaotic sequences from colored noise with power-law spectra [29]. However, other researchers have argued that a chaotic sequence cannot be well distinguished from either colored noise [65] or quasi-periodic motion (with singular power spectra) by its finite-time power spectra [33], especially when the chaotic data are contaminated by noise.

For a chaotic signal with complicated evolution (e.g., for the Lorenz time series, the time interval between peaks and the amplitudes of the sequence both vary with no obvious regularity), the simple frequency domain representation may obscure information related to timing. Spectral analysis usually only adopts the spectral amplitude, while neglects the phase information. Consequently, confusion will occur between any two signals with the same spectral amplitudes. A time-frequency joint analysis is therefore desirable to unveil these features [66]. However, few studies of time-frequency analysis for chaotic time series have been reported. Chandre *et al.* [34] performed a time-frequency analysis of Hamiltonian systems. The ridges<sup>1</sup>, extracted from a wavelet decomposition of a time series measured from the Hamiltonian systems, can reveal the phase-space structures (resonance transitions, trappings, etc.) and give a characterization of weak or strong chaos.

---

<sup>1</sup>For a time-frequency representation  $P(t, f)$ , the time-frequency points  $(t, f)$ , at which the spectrogram  $P(t, f)$  is maximum for each time  $t$ , are called ridges.

State recurrence is one important feature of chaotic systems. In the phase space reconstructed by time delay embedding, the state recurrences of a reference phase point turn out to be its nearest neighbors, which can provide redundant information but recur with no temporal regularity, as we will demonstrate later. Conventional time-frequency analysis methods (e.g., the wavelet transform), utilize only one segment of consecutive data and neglect temporally isolated state recurrences, resulting in poor performance. So a time-frequency analysis which can utilize all state recurrences is desirable.

This chapter focuses on: (i) demonstrating that the nearest neighbors cover segments of data with similar wave forms to that of the reference phase point and thus can provide redundant information for chaotic signal analysis and processing, (ii) proposing a spectrum estimator which can utilize all the neighbors, and (iii) performing a time-frequency analysis to (noisy) chaotic flow with the proposed spectrum estimator and extracting some features that can be used to distinguish the (noisy) chaotic data from colored noise. In order to utilize state recurrences, the nearest neighbors must be grouped according to their Euclidean distances to the reference point in phase space. As presented in Chapter 3, the LP method and its extension utilize state recurrences and obtain positive results. Analogously, a neighborhood-based spectrum estimator (NSE) is proposed to estimate the power spectra of the reference phase point. NSE first performs eigenvalue decomposition to the covariance matrix of the neighbors, and then estimates the power spectra of the reference phase point by applying the Blackman-Tukey (BT) estimator [68]. Thus, NSE utilizes the long-term state recurrence of chaotic systems, and bridges the theory of time delay embedding to the frequency domain.

## 4.2 Neighborhood-based spectrum estimation

### 4.2.1 State recurrences and nearest neighbors

As introduced in Sec. 2.1, the  $\varepsilon$ -neighborhood of reference phase point  $\mathbf{s}(n)$  is defined as  $\mathcal{N}_n \triangleq \{\mathbf{s}(k) : \|\mathbf{s}(k) - \mathbf{s}(n)\| < \varepsilon\}$  [see Eq. (2.2)] and further arranged as  $\mathcal{N}_n = \{\mathbf{s}(k_1), \mathbf{s}(k_2), \dots, \mathbf{s}(k_N)\}, k_1 < k_2 < \dots < k_N$ . For refer-

ence phase point  $\mathbf{s}(n)$ , its recurrence time is defined as  $T_n(i) = k_{i+1} - k_i$ ,  $i = 1, \dots, N - 1$ .

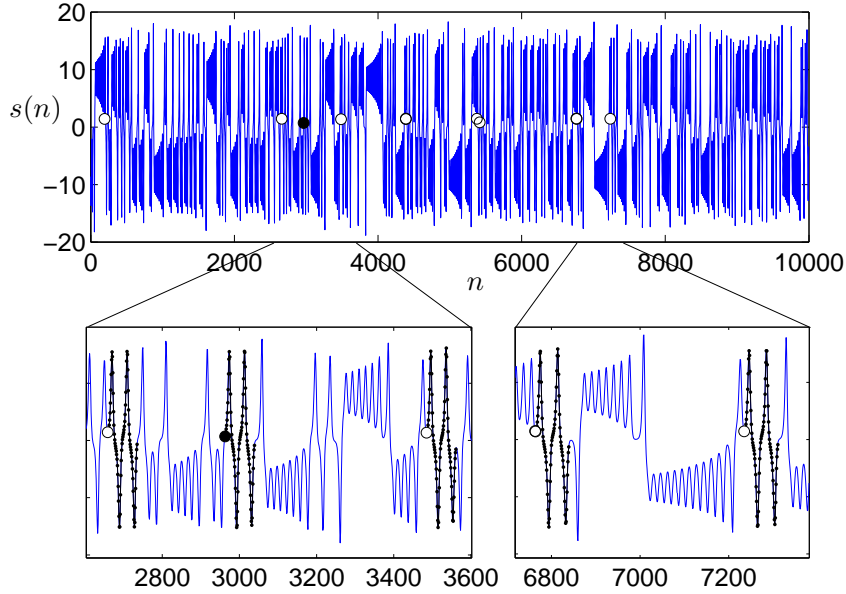


Figure 4.1: The Lorenz time series, and the first ten nearest neighbors of the reference phase point  $\mathbf{s}(2963)$ .  $\bullet$  — the sample  $s(2963)$ ;  $\circ$  — the sample  $s(k)$ , where  $s(k)$  is one of the first ten nearest neighbors of  $\mathbf{s}(2963)$ . The bottom panels are enlargements of short segments. Each segment marked with small dots corresponds to one neighbor in phase space.

Take a chaotic time series measured from the Lorenz system [Eq. (3.1)] as example. Note that all the Lorenz time series used in this chapter are 10 000 points sampled from the  $x$  component of the Lorenz time series with sampling interval  $\Delta t = 0.04$ , unless stated otherwise. Fig. 4.1 demonstrates the relationship between the reference phase point  $\mathbf{s}(2963)$  (randomly selected) and its first ten nearest neighbors with index  $k = 192, 2659, 3485, 4387, 4388, 5376, 5415, 6763, 6764, 7235$ . The reference phase point  $\mathbf{s}(n)$  covers a segment of time series  $[s(n - (d - 1)\kappa), s(n - (d - 1)\kappa + 1), \dots, s(n - 1), s(n)]^T$  with the length of embedding window  $L_w = (d - 1)\kappa + 1$ . For clarity, let  $\mathfrak{s}(n)$  denote this sequence<sup>2</sup>. It can be observed that the wave forms covered by the neighbors are similar to that of the reference phase point, but these neighbors recur with no obvious regularity.

<sup>2</sup>Note that  $\mathfrak{s}(n) = [s(n - (d - 1)\kappa), s(n - (d - 2)\kappa), \dots, s(n - \kappa), s(n)]^T$  denotes a phase point which is a  $d \times 1$  vector [see Eq. (2.1)], while  $\mathfrak{s}(n) = [s(n - (d - 1)\kappa), s(n - (d - 1)\kappa + 1), \dots, s(n - 1), s(n)]^T$  is a  $[(d - 1)\kappa + 1] \times 1$  vector which is associated with  $\mathbf{s}(n)$ . If  $\kappa = 1$ ,  $\mathfrak{s}(n)$  is the same as  $\mathbf{s}(n)$ .

From the viewpoint of signal processing, these similar wave-form segments contain much redundant information relative to the reference one. There are some neighbors that are adjacent in time, for example  $s(4387)$  and  $s(4388)$ . The adjacent neighbors that lie on the same recurrence trajectory provide only one new sample; primarily they serve to increase the weight of the corresponding state recurrence within the neighborhood.

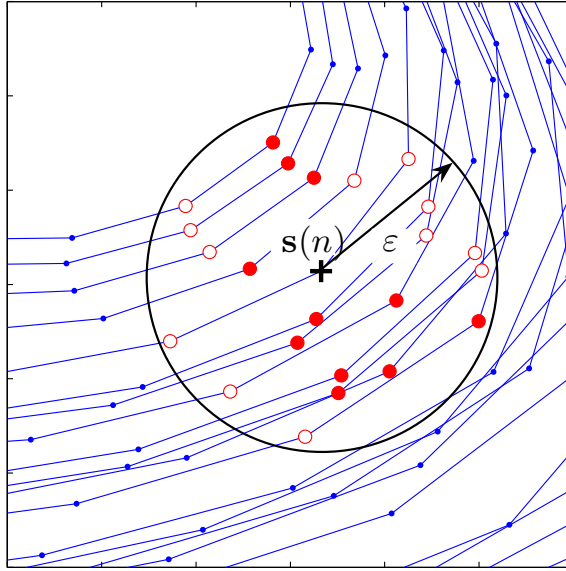


Figure 4.2: Schematic diagram of the neighborhood of type-II. For reference phase point  $s(n)$ , the points, denoted by both  $\bullet$  and  $\circ$ , in the circle of radius  $\varepsilon$  are all its neighbors in the  $\varepsilon$ -neighborhood  $\mathcal{N}_n$ . Some trajectories has more than one point that belongs to the  $\varepsilon$ -neighborhood  $\mathcal{N}_n$ . Only the nearest one ( $\bullet$ ) of the neighbors on each trajectory is selected to form the neighborhood of type-II. The points marked by  $\circ$  are not included by the neighborhood of type-II.

To investigate the recurrence time of state recurrence trajectory, a neighborhood of type-II is defined by selecting only one point from each recurrence trajectory. As Fig. 4.2 illustrates, only the nearest one among the neighbors on each recurrence trajectory is selected to form the neighborhood of type-II. A histogram of the recurrence times of the neighbors in all neighborhoods of type-II is shown in Fig. 4.3. It indicates that: (i) the recurrence time varies over a large range; and, (ii) the state recurrence seems to appear more frequently after some constant time periods that correspond to the peaks of the histogram. Note that a similar neighborhood of type-II has been defined by excluding the so-called

“sojourn points” and the statistics of recurrence time for chaotic time series was found to obey a scaling law [6]<sup>3</sup>. Moreover, the recurrence time statistics has been applied to detect nonstationarity and state transitions [59].

The conventional linear techniques (e.g., classical Fourier transform) neglect some scattered state recurrences and just utilize one segment of consecutive data. As a result, these techniques usually fail in analyzing chaotic time series. In contrast, the methods based on time delay embedding, such as the LP method, utilize the redundant information possessed by neighbors and thus frequently achieve better results for chaotic time series.

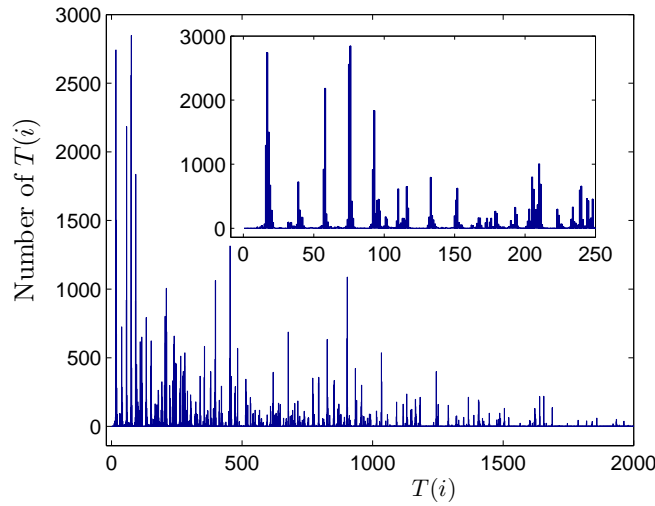


Figure 4.3: Histogram of the recurrence times of the first ten nearest neighbors of type-II. The small panel is an local enlargement of the main figure.

## 4.2.2 A neighborhood-based spectrum estimator

For the  $\varepsilon$ -neighborhood  $\mathcal{N}_n$ , an  $L_w \times N$  neighborhood matrix is defined as

$$\mathbf{D}_n = [\underline{\mathfrak{s}}(k_1) \quad \underline{\mathfrak{s}}(k_2) \quad \cdots \quad \underline{\mathfrak{s}}(k_N)],$$

where  $\underline{\mathfrak{s}}(k_i) = \mathfrak{s}(k_i) - \bar{\mathfrak{s}}(n)$  and  $\bar{\mathfrak{s}}(n) = \frac{1}{N} \sum_{\mathfrak{s}(k_i) \in \mathcal{N}_n} \mathfrak{s}(k_i)$ . First, eigenvalue decomposition to the covariance matrix, i.e.,  $\hat{\mathbf{C}}_n = \frac{1}{N} \mathbf{D}_n \mathbf{D}_n^T$ , of the  $\varepsilon$ -neighborhood

<sup>3</sup>Note that the recurrence time statistics in Ref. [6] is related to the radius of neighborhood, while the histogram in Fig. 4.3 is related to the first 10 nearest neighbors of type-II. Due to this difference in statistics, Fig. 4.3 does not show the scaling law revealed in Ref. [6].

$\mathcal{N}_n$  is performed,

$$\hat{\mathbf{C}}_n \mathbf{u}_i - \lambda_i \mathbf{u}_i = 0, \quad (4.2)$$

where  $\mathbf{u}_i = [u_i(1), u_i(2), \dots, u_i(L_w)]^T$  is the eigenvector associated with the  $i$ th largest eigenvalue  $\lambda_i$ . Then with the discrete-time Fourier transform of eigenvector  $\mathbf{u}_i$ ,

$$V_i(\omega) = \sum_{l=1}^{L_w} u_i(l) e^{-j\omega l}, \quad (4.3)$$

a neighborhood-based spectrum estimator (NSE) is devised as

$$P_{NSE}(\omega) = \frac{1}{L_w} \sum_{i=1}^{L_w} \lambda_i |V_i(\omega)|^2. \quad (4.4)$$

NSE is derived from the BT spectrum estimator [68], which has been reviewed in Sec. 2.3.1. For the BT estimator, the covariance matrix is estimated from only one segment of consecutive data [see Eqs. (2.14) and (2.19)]; while for NSE, the covariance matrix is estimated from the data segments covered by the temporally scattered neighbors. By this means, NSE can capture the long-time state recurrence of chaotic time series. If the neighborhood contains only the reference phase point, NSE reduces to the BT estimator.

For noisy chaotic time series, the local phase space can be divided into a signal subspace and a noise subspace which are orthogonal to each other. The signal subspace, constructed with  $[\mathbf{u}_1, \dots, \mathbf{u}_M]$ , contains most of the clean signal and a certain, small, amount of noise [25]; while the noise subspace, spanned by  $[\mathbf{u}_{M+1}, \dots, \mathbf{u}_{L_w}]$ , contains most of the components of noise and a small amount of signal components, where  $M$  is the minimum embedding dimension of the dynamical system [58]. With those components in the signal subspace, a principal component version of NSE is devised as

$$P_{PC-NSE}(\omega) = \frac{1}{L_w} \sum_{i=1}^M \lambda_i |V_i(\omega)|^2. \quad (4.5)$$

Obviously, the principal component version of NSE has the ability to suppress the effect of measurement noise for spectrum estimation of contaminated chaotic time series.

Furthermore, for each reference phase point, the *main frequency*  $\omega_m$  is defined as

$$P(\omega_m) = \max P(\omega_l), \omega_m \in \{\omega_l\}, \quad (4.6)$$

where  $\omega_l$  is the frequencies with local maximum power amplitude, i.e.

$$\left. \frac{dP(\omega)}{d\omega} \right|_{\omega=\omega_l} = 0, \quad \left. \frac{d^2P(\omega)}{d\omega^2} \right|_{\omega=\omega_l} < 0. \quad (4.7)$$

For each reference phase point, a power spectra can be estimated by NSE. A time-frequency distribution (also called *spectrogram*) can then be obtained as the reference phase point evolves along the phase trajectory. At the same time, the *main frequency* will form a *main ridge*. As to be shown below, this main ridge shows different characteristic patterns for data of different types.

### 4.3 Applications to chaotic time series

In this section, time-frequency analysis with NSE is presented for the Lorenz time series, the Rössler time series, and experimental laser data.

The Lorenz system is a typical chaotic system with two scrolls. As Fig. 4.4 indicates, the periodogram spectra [94] of the  $x$  and  $y$  components of the Lorenz system are broadband and similar to each other, while the periodogram spectra of the  $z$  component of the Lorenz systems have a peak. This spectral peak, which is marked by  $\downarrow F_1$  in Fig. 4.4(c) and named the *hidden frequency* in Refs. [95, 96], can reveal the frequency related to the principal oscillation of the Lorenz system. Note that this frequency is not a particular case of this sequence. The spectral peak universally exists with small deviation (1.305~1.330 Hz with 95% confidence), as Fig. 4.5(a) indicates. Though this oscillation exists in the  $x$  and  $y$  components simultaneously as the dynamical system evolves, the periodogram spectra of  $x$  and  $y$  fail to reveal it. The time interval between peaks and the amplitudes of the  $x$  and  $y$  sequences both vary with the phase state switching between the two scrolls with no obvious regularity, and thus can be considered as frequency modulation and amplitude modulation, respectively. The periodogram spectra cannot capture this complicated modulation and therefore fail to reveal

the principal oscillation.

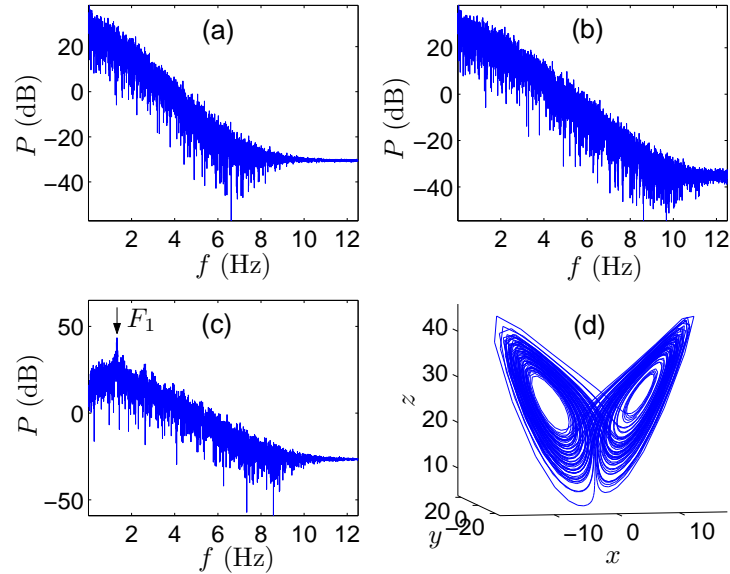


Figure 4.4: (a), (b), and (c) are the periodogram spectra of the time series measured from the  $x$ ,  $y$ , and  $z$  components of the Lorenz system, respectively; (d) the strange attractor of the Lorenz system. The  $y$ -axis label  $P$  denotes the power spectra.

In contrast, time-frequency analysis with NSE can reveal the principal oscillation. The Lorenz time series of the  $x$  component is over-embedded with time delay  $\kappa = 4$ <sup>4</sup> and embedding dimension  $d = 20$ , and the first 20 nearest neighbors are used in NSE. The spectrograms of the clean Lorenz time series and its noisy version are illustrated in Fig. 4.6, respectively. It can be observed that (i) the spectra are broadband and the energy is primarily distributed in the low frequency region, and (ii) the main ridge is formed by many short disjointed curves (even for the Lorenz time series contaminated by 5 dB white noise), which vary slowly around a frequency related to the principal oscillation. The bottom panel is the average of the spectrogram over time, which can be considered as the energy distribution versus frequency. The frequency corresponding to the maximum peak of this curve, labeled by  $\uparrow F_2$ , is approximately equal to the hidden frequency indicated by  $\downarrow F_1$  in Fig 4.4(c). Histograms of the main frequencies in Fig. 4.6 are shown in Figs. 4.5(b) and 4.5(c), respectively. The hidden frequency is located at the center of the main frequencies. This implies that the main frequencies contain

<sup>4</sup>Determined by the first minimum of mutual information [97].

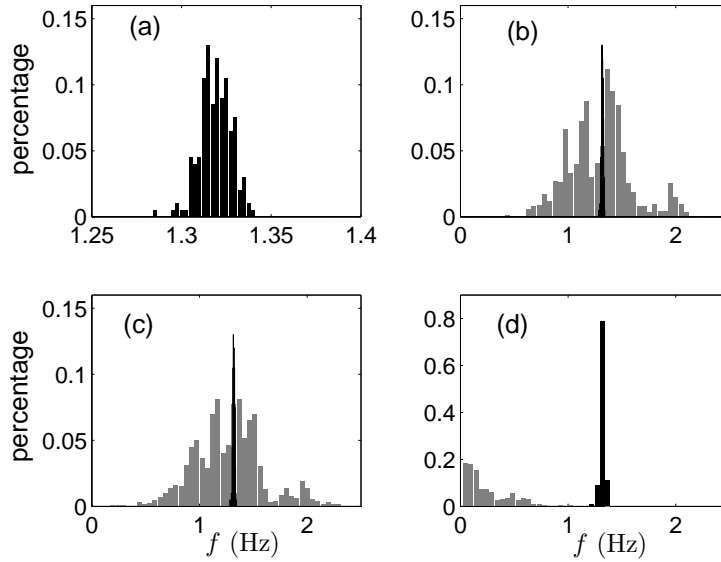


Figure 4.5: (a) The histogram of the spectral peaks [as  $\downarrow F_1$  in Fig. 4.4(c)] of 200 Lorenz sequences (10 000 points each sequence) measured from the  $z$  component with different initials; (b) the gray bars denote the histogram of the main frequencies in Fig. 4.6(a), and the black bars are the histogram in (a), which is plotted here for comparison; (c) the gray bars denote the histogram of the main frequencies in Fig. 4.6(b), and the black bars are the histogram in (a); (d) the histogram of the spectral peaks of 200 Lorenz sequences (500 points each sequence) estimated by periodogram; the gray and the black bars, respectively, denote the histograms of the spectral peaks of sequences measured from the  $x$  and  $z$  components simultaneously.

information related to the principal oscillation of chaotic system. Similar results can also be obtained with data measured from the  $y$  component of the Lorenz system.

The similar wave forms, covered by the neighbors, can enhance their common structure, i.e., the principal oscillation, while they may simultaneously “average” out the sub-structures and noise as well. Thus, even for the noisy Lorenz time series with 5 dB white noise, the principal oscillation can be extracted. Time-frequency analysis with the short-time periodogram [66] has also been performed of sequences simultaneously measured from the  $x$  and  $z$  components. As Fig. 4.5(d) indicates, the spectral peaks of sequences measured from the  $z$  component are located at the center region of the histogram in Figs. 4.5(b) and 4.5(c), while the spectral peaks of sequences measured from the  $x$  component are close to zero frequency. Note that a different window length has been adopted for the

short-time periodogram, but the pattern of the main frequencies is similar to that shown in Fig. 4.5(d).

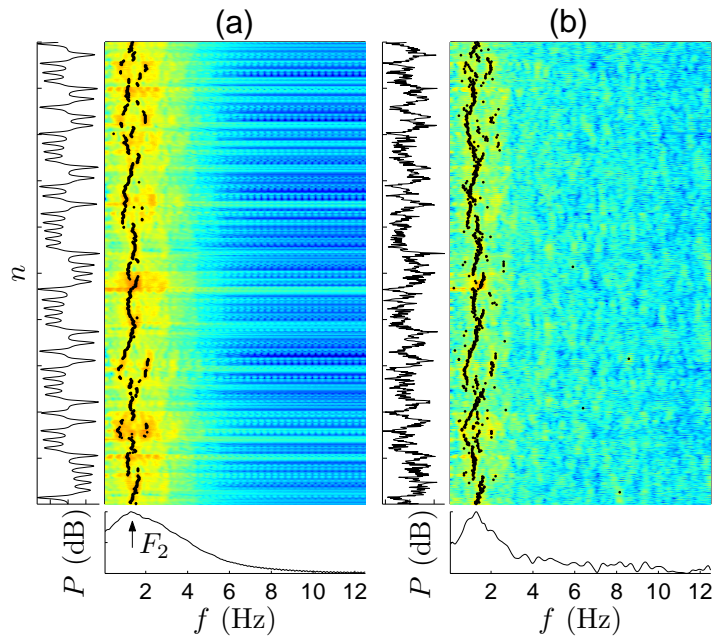


Figure 4.6: Spectrogram of a clean Lorenz time series measured from the  $x$  component with parameter  $r = 28$  (a), and its noisy version with 5 dB additive white noise (b) by NSE, respectively. For each case, only a 1000-sample segment of the spectrogram is plotted. For each sub-figure, the left panel is the time series, the big panel is the corresponding spectrogram estimated by NSE, and the bottom panel is the average of the spectrogram over time. The black points indicate the main frequencies. This layout is followed in all following spectrogram figures, unless otherwise stated.

The Lorenz system with different values of the parameter  $r$  has been widely studied and rich dynamics has been revealed [98]. We further apply NSE to (noisy) Lorenz time series generated with different values of the parameter  $r$  while fixing the other two parameters  $(\sigma, b) = (10, 8/3)$ . When the Lorenz system is chaotic (e.g.,  $r = 33$  and  $38$ ), the main ridge is formed with unconnected short curves, which is similar to the case of  $r = 28$  (see Fig. 4.6). While when the Lorenz system is non-chaotic (e.g.,  $r = 18$  and  $148$ ), the system is almost periodic and the main frequencies are approximately constant. As Fig. 4.7 indicates, the hidden frequencies can be detected by NSE even when the Lorenz time series is contaminated by 5 dB additive white noise (only one mismatch for the

case of noisy data with 5 dB noise). For the cases of  $r = 28, 33, 38, 43, 48, 53$ ,  $d$  is set as  $d = 20$ , and for the cases of  $r = 58, 63, 68, 73$ ,  $d$  is set as  $d = 10$ . This is because as the hidden frequency increases with  $r$ , the period of oscillation becomes smaller and thus the reference phase point will cover more cycles, which leads to fewer well-matched neighbors. With only few appropriate neighbors, the reliability of NSE will reduce.

The length of the embedding window,  $L_w = (d - 1)\kappa + 1$ , is a tradeoff between the reliability and the frequency resolution. On the one hand, to get a better reliability,  $L_w$  should be set relatively shorter to ensure more appropriate neighbors. On the other hand, to obtain a spectra with higher frequency resolution,  $L_w$  should be set relatively longer. With sampling time interval  $\Delta t = 0.04$  and  $L_w = 77$  ( $d = 20, \kappa = 4$ ), the physical resolution of the spectra estimated by periodogram is  $\frac{1}{\Delta t L_w} \approx 0.32$  Hz. This resolution can not provide an accurate detection of the hidden frequency (about 1.32 Hz when  $r = 28$ ). Padding zeros at the end of data is a common strategy adopted in implementation of the

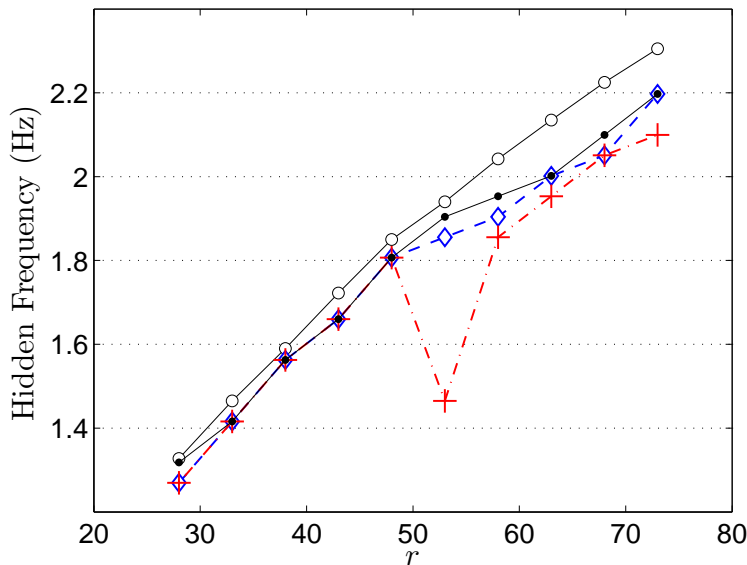


Figure 4.7: Hidden frequency of the Lorenz time series.  $\circ$  — by periodogram with a clean Lorenz time series measured from the  $z$  component,  $\bullet$  — by NSE with a clean series measured from the  $x$  component,  $\diamond$  — by NSE with a noisy version of the clean time series of the  $x$  component (10 dB additive white noise),  $+$  — by NSE with a noisy version of the clean time series of the  $x$  component (5 dB additive white noise).

discrete Fourier transform, so as to obtain a higher computational resolution, i.e., smaller frequency interval between the calculated bins. In this chapter,  $(512 - L_w)$  zeros are padded to the end of  $\mathbf{u}_i$  and Eq. (4.3) is implemented by 512-point fast Fourier transform (FFT). With this strategy, the computational resolution is  $\frac{1}{0.04 \times 512} \approx 0.05$  Hz, which can be considered as an appropriate result of interpolation. But padding zeros to individual realization does not increase the physical resolution of the estimated spectra, and the location of the spectral peak may depart from the hidden frequency [67, 68].

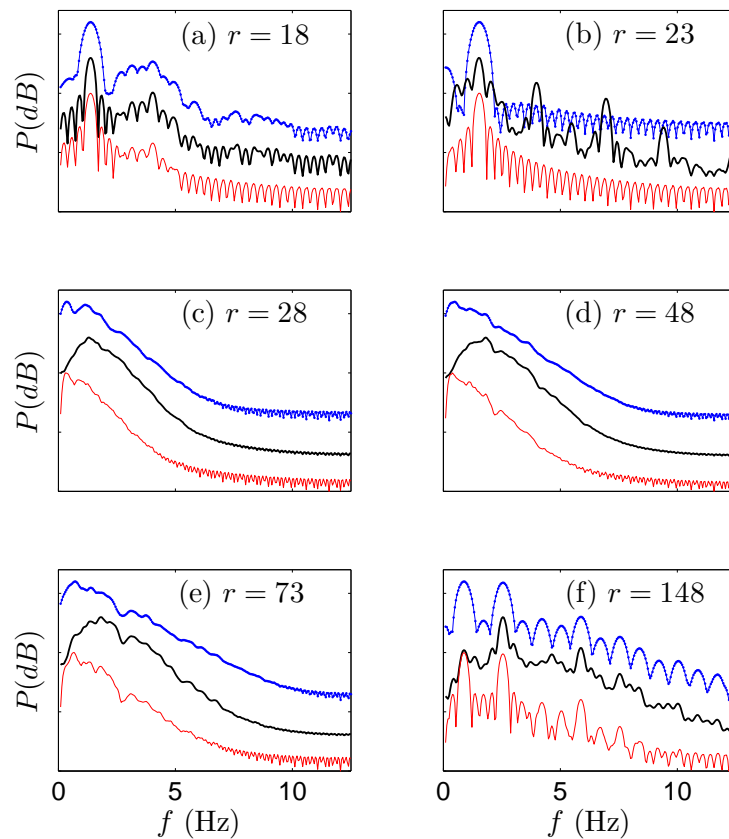


Figure 4.8: Energy distribution versus frequency of the Lorenz time series measured from the  $x$  component. The maximum Lyapunov exponents corresponding to (a) – (f) are  $-0.23$ ,  $-0.05$ ,  $0.90$ ,  $1.24$ ,  $1.53$ , and  $0.00$ , respectively. In each panel, the three curves correspond to the normalized average of the spectrogram by the short-time periodogram, NSE, and the BT estimator from up to down. Each curve is offset vertically for clarity, and the scale in the vertical axis is therefore arbitrary.

Figure 4.8 shows the energy distribution versus frequency for the Lorenz

time series. When the system has non-positive maximum Lyapunov exponent [Figs. 4.8(a), 4.8(b), and 4.8(f)], the time series seems pseudo-periodic. NSE can detect a fundamental frequency as well as the short-time periodogram and the BT estimator, though some harmonics are different, while for the Lorenz system with positive maximum Lyapunov exponent [Figs. 4.8(c), 4.8(d), and 4.8(e)], only NSE can reveal the frequency (i.e., the hidden frequency) related to the principal oscillation, which has been verified in Fig. 4.7.

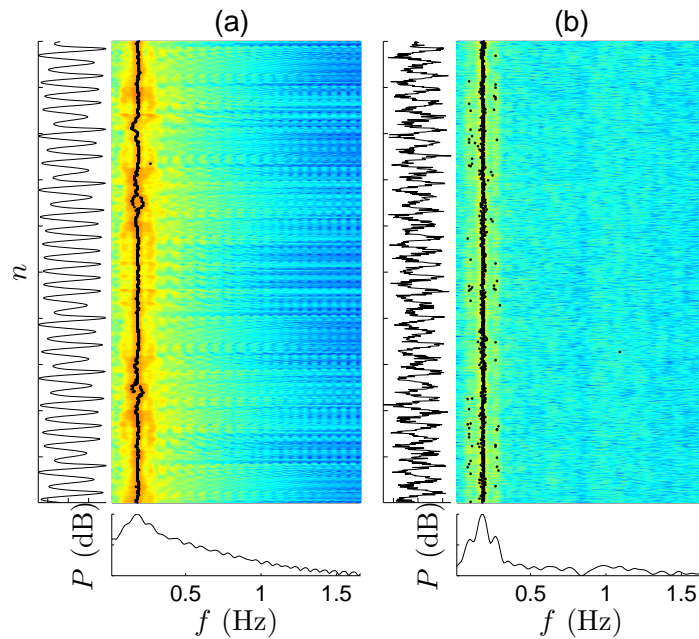


Figure 4.9: Spectrogram of a clean Rössler time series (a) measured from the  $x$  component and its noisy version (b) with 5 dB additive white noise by NSE, respectively.  $\tau = 7$ ,  $d = 12$ , and the sampling interval is  $\Delta t = 0.2$ .

The Rössler system,

$$\begin{cases} \dot{x} = -(y + z), \\ \dot{y} = x + 0.2y, \\ \dot{z} = 0.2 + xz - Cz, \end{cases} \quad (4.8)$$

is another typical chaotic system with periodic motion superimposed on chaotic behavior [85]. When  $C = 4.6$ , the Rössler system is chaotic [32]. Its power spectra contain almost periodic  $\delta$ -function peaks and broad background components.

The sharp peaks are due to periodic motion, and the broad components are the result of amplitude modulation.

As Fig. 4.9(a) indicates, the Rössler time series is something like a pseudo-periodic one with amplitude fluctuation and the main frequency varies very little with time. The peak of the curve of the energy distribution corresponds to the fundamental frequency of the Rössler system. For the noisy Rössler time series [Fig. 4.9(b)], the main ridge is obvious and “stationary” with only a few scattered points.

NSE is further applied to an experimental laser time series [99], which can be obtained from the Santa Fe time series competition data<sup>5</sup>. To better match the neighbors, the  $\varepsilon$ -neighborhood is formed with  $\kappa = 1$ , and  $d = 80$ . As Fig. 4.10 indicates, the main frequency decreases little during the pulse boosting and jumps back as the oscillation collapses.

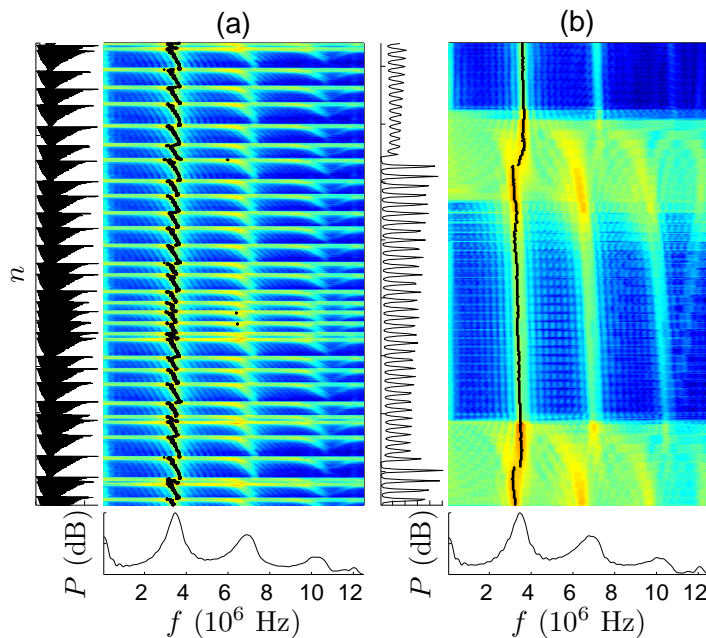


Figure 4.10: Spectrogram of a laser time series (10 000 samples) by NSE. (a) 10 000-point data and their spectrogram; (b) an enlargement of (a) from point 2921 to point 3320.

<sup>5</sup><http://www-psych.stanford.edu/~andreas/Time-Series/SantaFe.html>

For one more example, NSE is applied to data measured from Chua's circuit [100]. Results show that the principal oscillation of Chua's circuit can be revealed clearly by its main ridge pattern even when the data are corrupted by additive noise. For high dimensional chaotic flow such as Mackey-Glass system [101], NSE may also be applicable. For this case, the recurrence of state may be less frequent. Then a longer duration of data are required so as to provide enough well-matched neighbors for NSE.

For comparison, time-frequency analysis with the short-time periodogram and the BT estimator are performed for the (noisy) Rössler time series, laser data, and Chua's circuit data. For Rössler time series and laser data, it is shown that both methods get similar main ridge patterns, respectively. While for Chua's circuit data, time-frequency analysis with the short-time periodogram fails to reveal the intrinsic oscillation.

## 4.4 Distinguishing noisy chaotic flow from colored noise

It has been reported that (noisy) chaotic data is difficult to be distinguished from colored noise by their spectral falloff patterns [65]. Chaotic flow has scattered state recurrences, while colored noise does not possess this deterministic feature. From this point, time-frequency analysis with NSE is expected to reveal this difference and thus provides an alternative method to distinguish them.

A pink noise and a surrogate sequence are taken as examples. The pink noise (10 000 points) is generated by a first-order autoregressive process [AR(1)],  $w(n+1) = \beta w(n) + (1-\beta)\epsilon(n)$ , where  $\beta = 0.69$  and  $\epsilon(n) \sim N(0,1)$  is a Gaussian process [102, 103]. As Fig. 4.11 indicates, the spectra of the clean Lorenz time series measured from the  $x$  component have a long exponential-law scaling region (marked by A). As the Lorenz time series is contaminated by additive noise, the exponential-law region (as that labeled by B and C for the cases with 10 dB and 5 dB white noise, respectively) becomes less obvious and difficult to be distinguished from that of pink noise (marked by E), while the time-frequency analysis with NSE is sensitive to this difference. As Fig. 4.12(a)

indicates, the main frequency of pink noise varies along time with no regularity, while the main ridge pattern of the chaotic Lorenz time series with 5 dB white noise [Fig. 4.6(b)] exhibits obvious temporal structures.

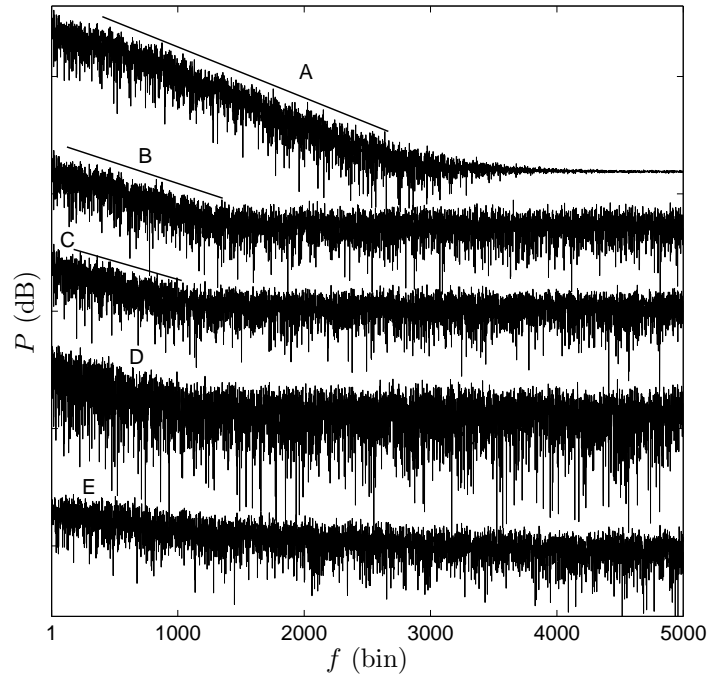


Figure 4.11: Power spectra estimated by periodogram. From the top down, the spectra, marked by A, B, C, D, and E, correspond to the clean Lorenz time series [the one used in Fig. 4.6(a)], the noisy Lorenz time series with 10 dB white noise, the noisy Lorenz time series with 5 dB white noise [i.e., the one used in Fig. 4.6(b)], the phase shuffled surrogate data of the noisy Lorenz time series, and the pink noise generated by AR(1), respectively. Each time series has 10 000 points. The three black lines indicate the exponential-law scaling regions of the corresponding spectra. Here, the calculated frequency bins are not scaled to the real frequency with units of Hz.

Surrogate tests are often used to detect nonlinearity in time series [93]. Here, the surrogate data are generated by shuffling the phase of the original noisy Lorenz time series [the one used in Fig. 4.6(b)] [84]. The power spectra of the surrogate data (marked by D in Fig. 4.11) are similar to those of the original data (marked by C). However, due to the phase shuffling, the surrogate data do not possess the deterministic features of the original noisy Lorenz time series, and their main ridge patterns are therefore clearly distinct [Fig. 4.12(b) vs. Fig. 4.6(b)]. As discussed in Sec. 4.1, time-frequency joint analysis can reveal some

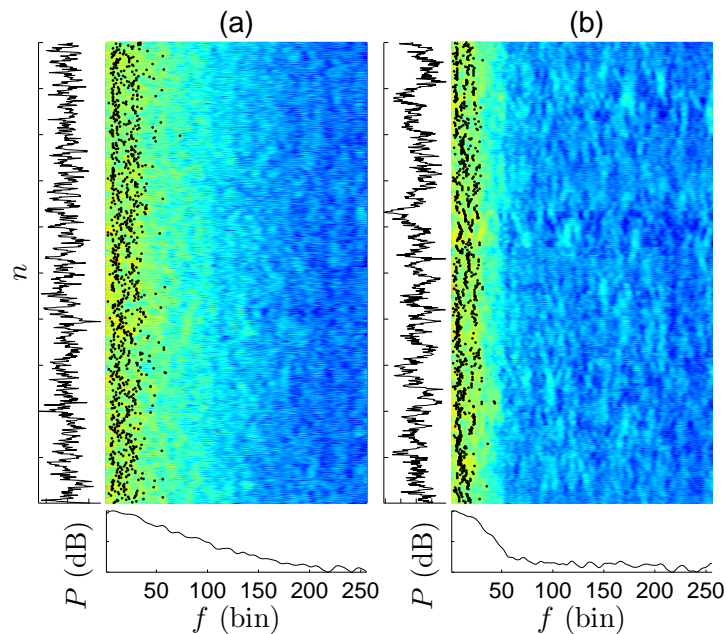


Figure 4.12: The spectrogram of pink noise (a) and the surrogate data (b) by NSE, respectively. The frequency bins calculated by FFT are not scaled to the real frequency with units of Hz.

information that is obscured by just a single finite-time frequency representation.

The histograms of the main frequencies related to Fig. 4.12 are illustrated in Fig. 4.13. Comparing with Fig. 4.5, the main frequencies of both the pink noise and the surrogate data are mainly distributed in a region near zero frequency, while the main frequencies of (noisy) chaotic time series are located in a region relatively far from zero frequency.

In summary, for the chaotic Lorenz time series, the main ridge has many short unconnected curves, which vary around the hidden frequency. We believe that this main ridge pattern is a characteristic of chaotic flow. For the chaotic Rössler time series, the wave-form is pseudo-periodic, yielding a main ridge that varies smoothly and slowly. In the time domain, the wave-form variation of the Lorenz time series (switching between two scrolls) seems more “complex” than that of the Rössler time series (evolving around one focus). Therefore, the main ridge of the Rössler time series is more “regular”. For noisy chaotic flow, the

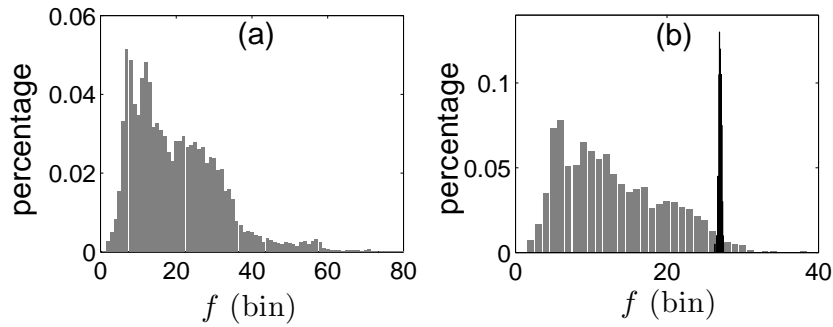


Figure 4.13: (a) Histogram of the main frequencies in Fig. 4.12(a). (b) The gray bars denote the histogram of the main frequencies in Fig. 4.12(b), and for comparison, the histogram in Fig. 4.5(a) is plotted by black bars.

principal oscillation can be detected by NSE, and the main ridge reserves some characteristics of the corresponding clean data, while for the pink noise and surrogate data, there is no deterministic feature, and thus the main ridge is irregular, which is distinct from that of (noisy) chaotic flow. This difference in main ridge pattern can be used to distinguish them. NSE is designed to investigate (noisy) chaotic flow based on its state recurrence. Note that various methods from other viewpoints, such as the 0-1 test [104, 105] and method based on scale-dependent Lyapunov exponent [106], have been developed to investigate whether a nonlinear time series is deterministically chaotic or stochastic. Nevertheless, these are beyond the focus of this thesis.

## 4.5 Conclusion

In this chapter, time-frequency analysis for chaotic flow is performed. First, chaotic data are over-embedded, and the relation between the reference phase point and its nearest neighbors is demonstrated. Neighbors represent the state recurrences of the reference phase point and cover data segments with similar wave forms to each other, but recur with no obvious temporal regularity. To apply these state recurrences, a neighborhood-based spectrum estimator (NSE) is devised for chaotic flow, bridging the theory of time delay embedding and the frequency domain. Then time-frequency analysis with NSE is performed for (noisy) Lorenz time series. It is found that NSE can reveal the frequency

related to the principal oscillation of the Lorenz system, which, however, cannot be detected by the periodogram method. Further, time-frequency analysis with NSE is applied to the Rössler time series and experimental laser data. It is shown that their main frequencies have similar characteristics: they vary slowly around a frequency related to the principal oscillation of the dynamical system. After that, NSE is applied to pink noise and phase shuffled surrogate data. The results show that their main ridge patterns are distinct from that of (noisy) chaotic flow, thus providing an alternative method to distinguish them, though for some real or more chaotic systems, a distinction may not be that easy.

On the one hand, NSE can reveal some meaningful features that classical methods fail to uncover; on the other hand, NSE also may “average” out some sub-structures. So NSE can be adopted together with other methods to make a comprehensive understanding of the dynamical system.

# Chapter 5

## Neighborhood-based phase synchronization detection

Two schemes are proposed to detect phase synchronization from noisy chaotic data. The first is a neighborhood-based method which links time delay embedding with instantaneous phase (IP) estimation. The second adopts the local projection (LP) method as a preprocessing filter to noisy data. Both schemes are based on the theory of time delay embedding and utilize the state recurrences of chaotic data. The proposed schemes are applied to data measured from two typical chaotic systems, i.e., the coupled Rössler systems and the coupled Lorenz systems, respectively. Simulation results show that phase synchronization (PS), which may be buried by noise, is detected even when the noise level is high. Moreover, the proposed schemes can avoid the overestimation of the degree of PS, which may be introduced by the Hilbert transform combined with a traditional linear bandpass filter to noisy data.

### 5.1 Introduction

As introduced in Chapters 1 and 2, synchronization exists ubiquitously in both natural and engineering systems, and has been studied extensively for its numerous applications (for a review, cf. [35]). PS, as a weak form of synchro-

nization, has been observed in various systems, such as coupled chaotic oscillators [38,44], chaotic laser array [41], biomedical signals [39], and neuronal oscillations [52,53]. Various IP definitions have been introduced. One class of them is based on particular transforms, such as the Hilbert transform [38], the wavelet transform [40], and a generalized transform with a Gaussian filter [41], to the observed data. Another class of IPs is defined as the angle of evolving trajectory, which is reconstructed from the two-dimensional projection of the system [35,42] or the time derivative of the projection [43,44], around a fixed point.

For particular data (e.g., data from coherent Rössler systems), IP can be directly estimated with the Hilbert transform [38]. If the data are contaminated by measurement noise, the IP so estimated will involve artificial phase slips, i.e., the discontinuous “jumps” of the unwrapped phase, which do not imply any intrinsic oscillation but are due to noise. For this case, a linear filter with narrow bandwidth is usually first applied to the noisy data, and then IP is estimated from the output of the filter. However, on the one hand, the linear filter with narrow bandwidth may lead to a spurious overestimation of the actual degree of PS [56]; on the other hand, the linear filter with broad bandwidth will leave a certain amount of intraband noise, and thus can not suppress the effect of noise effectively. Recently, a data-driven filter has been proposed [107]. It is argued that this filter can reduce the noise-induced susceptibility of the estimated IP.

Some other methods have also been proposed to detect (phase) synchronization in noisy data. For example, surrogate methods are applied to provide significance tests of PS in noisy data [45], where both the noisy data and their surrogate data are passed through a linear filter first. However, it is reported that weak synchronization may be artificially detected even from two independent and identically distributed (i.i.d.) Gaussian noise series after narrow bandwidth filtering [56]. Nonlinear interdependence is proposed to characterize generalized synchronization, utilizing the mutual neighbors and the feature that similar initials lead to similar successors in the evolving chaotic system [46–48]. The performances of various synchronization measures, including nonlinear interdependence, mutual information, and PS indexes based on both the Hilbert transform and wavelet transform, are compared with real EEG data. It shows that these measures can indicate a similar tendency in the degree of synchronization [49].

Further, these measures are tested with data (from typical coupled chaotic systems) which are contaminated by measurement noise. Results show that these measures work effectively when the noise level is low, but can be greatly degraded when the noise level is relatively high [50]. It is difficult to say which measure is the best in general. Recently, a statistical measure of recurrences is proposed to detect PS, and is robust for noise [44]. After that, a general framework is proposed to detect PS through localized sets rather than by defining IP directly [51]. This framework can be applied to oscillators with multiple time scales (e.g., spiking and/or bursting neurons). However, whether it is robust to noise or not is (as far as we are aware) not reported yet. Moreover, these two methods can only quantify the degree of synchronization in the mean.

To overcome the limitations discussed above, two schemes are proposed to estimate IP for noisy chaotic data from the viewpoint of time delay embedding. In phase space reconstructed by time delay embedding [7], the state recurrences of a reference vector<sup>1</sup> turn out to be its nearest neighbors. As demonstrated in Sec. 4.2.1, these neighbors can provide redundant information [13]. This feature has been successfully utilized in chaotic time series analysis and processing, such as nonlinear prediction [15], time-frequency analysis [13], detection of state transitions [6], and noise reduction (the LP method presented in Chapter 3) [11, 18, 22, 62, 108, 109].

The first scheme is a method of neighborhood-based phase estimation (NPE). The reference vector and its nearest neighbors (i.e., state recurrences) cover segments of data with a similar wave form [13]. This implies that the analytical trajectories (constructed with the Hilbert transform [38]) corresponding to the reference vector and its neighbors are close to each other in the Hilbert plane, as will be illustrated later. With this observation, the IP of noisy data is estimated by a certain averaging of the corresponding IPs of the neighbors. The second scheme uses the local LP method, instead of the traditional linear bandpass filter, as a preprocessing filter to noisy data. After noise reduction, the IP can be estimated with the Hilbert transform. Simulation results show that the IP estimated by the proposed schemes suffers much less from the artificial phase slips, and thus PS (both in local time and in whole time), which may otherwise be buried

---

<sup>1</sup>In this chapter, the reference phase point is called reference vector, so as to avoid confusion of the word “phase” in both *phase point* and *instantaneous phase*.

by measurement noise, is reliably detected.

## 5.2 Neighborhood-based phase estimation

The most popular definition of IP is based on the Hilbert transform. Given a signal  $s(t)$ , its analytic signal is defined as

$$s^{(a)}(t) = s(t) + j\tilde{s}(t) = A(t)e^{j\phi(t)}, \quad (5.1)$$

where

$$\tilde{s}(t) = \mathcal{H}[s(t)] = \frac{1}{\pi} \text{P.V.} \int_{-\infty}^{\infty} \frac{s(\tau)}{t - \tau} d\tau \quad (5.2)$$

is the Hilbert transform of  $s(t)$ . Then the IP of signal  $s(t)$  is

$$\phi(t) = \arctan \frac{\tilde{s}(t)}{s(t)}. \quad (5.3)$$

To illustrate the method of neighborhood-based phase estimation (NPE), the coupled Rössler systems  $\Sigma_{1,2}$  [39]

$$\begin{aligned} \dot{x}_{1,2} &= -\varpi_{1,2}y_{1,2} - z_{1,2} + \zeta_{1,2} + \xi(x_{2,1} - x_{1,2}), \\ \dot{y}_{1,2} &= \varpi_{1,2}x_{1,2} + \alpha y_{1,2}, \\ \dot{z}_{1,2} &= \beta + z_{1,2}(x_{1,2} - \gamma), \end{aligned} \quad (5.4)$$

are taken as an example, where  $\varpi_{1,2} = 1 \pm 0.015$ ,  $\xi$  is the coupling strength,  $\zeta_{1,2} \sim N(0, \sigma_\zeta^2)$ , and  $\sigma_\zeta$  is the standard deviation of the dynamical noise. Data are integrated from variables  $x_{1,2}$  using the fourth-order Runge-Kutta method (Matlab function *ode45*) with sampling interval  $\Delta t = 0.2$ . The initials are set randomly, and 10 000 samples are adopted after the transient state. The measured time series is denoted as  $s_{1,2}(n\Delta t) = x_{1,2}(n\Delta t) + w_{1,2}(n\Delta t)$ , where  $w_{1,2}$  is measurement noise, and assumed to be Gaussian white noise  $w_{1,2} \sim N(0, \sigma_{w_{1,2}}^2)$ . To simplify notation,  $\Delta t$  is omitted and  $s_{1,2}(n\Delta t)$  is written as  $s_{1,2}(n)$  from now on.

Given the time series  $\{s(n)\}_{n=0}^{L-1}$  with  $L = 10\,000$  samples, the time delay

vectors can be reconstructed by time delay embedding [7], i.e.,  $\{\mathbf{s}(n)\}_{n=(d-1)\kappa}^{L-1}$ ,

$$\mathbf{s}(n) = [s(n - (d - 1)\kappa), s(n - (d - 2)\kappa), \dots, s(n - \kappa), s(n)]^T.$$

The  $\varepsilon$ -neighborhood of the reference vector  $\mathbf{s}(n)$  is defined as

$$\mathcal{N}_n \triangleq \{\mathbf{s}(k) : \|\mathbf{s}(k) - \mathbf{s}(n)\| < \varepsilon\}.$$

Let  $\{\tilde{s}(n)\}$  denote the Hilbert transform of the observed time series  $\{s(n)\}$ . Corresponding to time delay vector  $\mathbf{s}(n)$ , the time delay vector of  $\{\tilde{s}(n)\}$  is

$$\tilde{\mathbf{s}}(n) = [\tilde{s}(n - (d - 1)\kappa), \tilde{s}(n - (d - 2)\kappa), \dots, \tilde{s}(n - \kappa), \tilde{s}(n)]^T, \quad (5.5)$$

and the analytical trajectory associated with  $\mathbf{s}(n)$  is defined as

$$\mathbf{s}^{(a)}(n) = \mathbf{s}(n) + j\tilde{\mathbf{s}}(n). \quad (5.6)$$

Note that  $\tilde{\mathbf{s}}(n)$  is not calculated from  $\mathbf{s}(n)$ , but is formed from  $\{\tilde{s}(n)\}$  by time delay embedding, and  $\{\tilde{s}(n)\}$  is integrated in the whole time domain [Eq. (5.2)], while  $\tilde{\mathbf{s}}(n)$  is mainly contributed by the vicinity of  $\mathbf{s}(n)$  in time.

Figure 5.1 illustrates the relation between the reference vector and its neighbors in the time domain and in the  $(s, \tilde{s})$ -plane. It shows that the reference vector and its neighbors cover segments of data with similar wave-form [Fig. 5.1(a)], and their associated analytical trajectories of clean data are thus close to each other [Fig. 5.1(b)]. However, the related trajectories of noisy data appear irregularly [Fig. 5.1(c)], which will yield artificial phase slips. To deal with this problem, NPE is proposed as follows.

For reference vector  $\mathbf{s}(n)$ , the average of its neighbors is

$$\bar{\mathbf{s}}(n) = \frac{1}{N} \sum_{\mathbf{s}(k) \in \mathcal{N}_n} \mathbf{s}(k), \quad (5.7)$$

and the average of the related neighbors of  $\tilde{\mathbf{s}}(n)$  is

$$\bar{\tilde{\mathbf{s}}}(n) = \frac{1}{N} \sum_{\tilde{\mathbf{s}}(k) : \mathbf{s}(k) \in \mathcal{N}_n} \tilde{\mathbf{s}}(k), \quad (5.8)$$

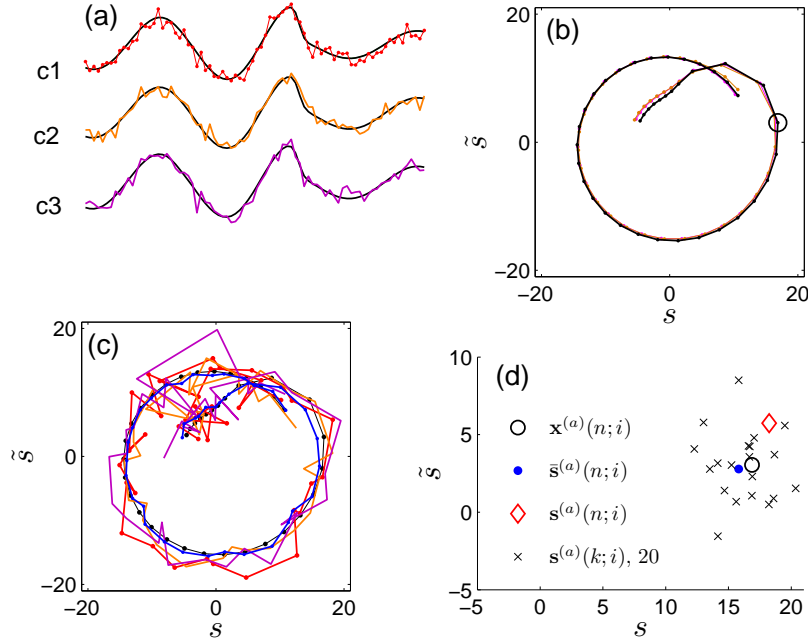


Figure 5.1: The relation between the reference vector and its neighbors in the time domain (a) and in the  $(s, \tilde{s})$ -plane [(b), (c), and (d)]. In this figure, the data are measured from variable  $x_1$  of the coherent Rössler systems [Eq. (6.24)], with parameters  $\xi = 0.035$ ,  $\alpha = 0.15$ ,  $\beta = 0.2$ ,  $\gamma = 10$ ,  $\sigma_{\zeta_{1,2}} = 0$ ,  $\sigma_{w_{1,2}} = 0.3\sigma_{x_{1,2}}$ ,  $\kappa = 1$ , and  $d = 80$ . Curve c1 is the segment covered by the reference vector  $s(n)$ , and curves c2 and c3 are the segments covered by two neighbors [ $s(k_1)$  and  $s(k_2)$ ] of the reference vector, respectively. Note that the neighbors are searched from noisy data, and the smooth curves [i.e.,  $x(n)$ ,  $x(k_1)$ , and  $x(k_2)$ ] are the clean versions of the coarse curves, respectively. The analytical trajectories [i.e.,  $x^{(a)}(n)$ ,  $x^{(a)}(k_1)$ , and  $x^{(a)}(k_2)$ ] constructed from clean data are very close to each other (b), while the corresponding trajectories [ $s^{(a)}(n)$ ,  $s^{(a)}(k_1)$ , and  $s^{(a)}(k_2)$ ] of the noisy version seem pell-mell (c). The blue (dark gray) trajectory in (c), estimated by NPE, is close to the corresponding trajectory [black, in (b)] of clean data. For clarity, only the trajectories corresponding to the mid-half segments of the curves in (a) are plotted in (b) and (c), respectively. A particular entry  $s^{(a)}(n; i)$  ( $\diamond$ ) of  $s^{(a)}(n)$ , its clean version  $x^{(a)}(n; i)$  [ $\circ$  in (b) and (d)], its first 20 noisy neighbors  $s^{(a)}(k; i)$  ( $\times$ ), and the average  $\bar{s}^{(a)}(n; i)$  of these 20 neighbors ( $\bullet$ ) are illustrated in (d).

where  $N = |\mathcal{N}_n|$  is the number of neighbors. Let  $\bar{s}^{(a)}(n) = \bar{s}(n) + j\bar{\tilde{s}}(n)$  denote the estimate of the analytical trajectory of  $x(n)$ , and  $s(n; i)$  denote the  $i$ th entry of  $s(n)$ . Then  $\bar{s}^{(a)}(n; i)$  is an estimate of the analytical signal at instant  $[n - (d - i)\kappa]\Delta t$ . As  $s(n)$  appears as an entry of  $s(l)$ ,  $l = n, \dots, n + (d - 1)\kappa$ , there are  $d$  estimates of  $\bar{s}^{(a)}(n)$  at instant  $n\Delta t$ . It is difficult to say which estimate is

the best, so the average of the estimates at the same instant is taken as the final estimate of the analytical signal at this instant, yielding the estimated analytical signal  $\{\bar{s}^{(a)}(n)\}$ , where  $\bar{s}^{(a)}(n) = \bar{s}(n) + \bar{\tilde{s}}(n)$ . Then IP is estimated as

$$\hat{\phi}(n) = \arctan \frac{\bar{\tilde{s}}(n)}{\bar{s}(n)}. \quad (5.9)$$

As that presented in Sec. 2.2 and Chapter 3, the LP method has been studied extensively [11, 18, 22, 62, 108, 109]. The second scheme just uses the LP method, instead of the traditional linear bandpass filter, as a preprocessing filter to noisy data. After noise reduction, IP can be obtained from  $\{\hat{x}(n)\}$  with the Hilbert transform. In this chapter, this scheme is denoted by P-LP. It has been reported that the LP method is more powerful than the linear bandpass method in reducing noise for chaotic data [11, 18, 22].

### 5.3 Phase synchronization of coupled Rössler systems

First, the proposed schemes are applied to data measured from coupled coherent Rössler systems  $\Sigma_{1,2}$  [Eq. (6.24)] with no dynamical noise. The parameters are set as  $\alpha = 0.15$ ,  $\beta = 0.2$ ,  $\gamma = 10$ ,  $\sigma_{\zeta_{1,2}} = 0$ , and  $\sigma_{w_{1,2}} = \eta\sigma_{x_{1,2}}$ , where  $\eta$  is the level of measurement noise.

Figure 5.2 illustrates the detection of PS by the proposed schemes. Let P-HT denote the method that IP is obtained by applying the Hilbert transform directly to (noisy) data. When there is measurement noise, the IP difference  $(\phi_1 - \phi_2)$  of the coupled systems  $\Sigma_{1,2}$  [Eq. (6.24)], estimated by P-HT, fluctuates irregularly [Fig. 5.2(a), “P-HT,  $\eta = 0.5$ ” and “P-HT,  $\eta = 0.7$ ”], and the wrapped phase difference  $\varphi = (\phi_1 - \phi_2) \bmod(2\pi)$  exhibits a much broader distribution compared with that of the corresponding clean data [Figs. 5.2(c) and 5.2(d) vs Fig. 5.2(b)]. It may appear that the coupled oscillators are non-synchronous or weakly synchronous, though the intrinsic oscillations are synchronous [Fig. 5.2(a), “P-HT,  $\eta = 0$ ”]. This misclassification can be avoided by NPE and P-LP. The unwrapped phase difference [Fig. 5.2(a), “NPE,  $\eta = 0.7$ ”]

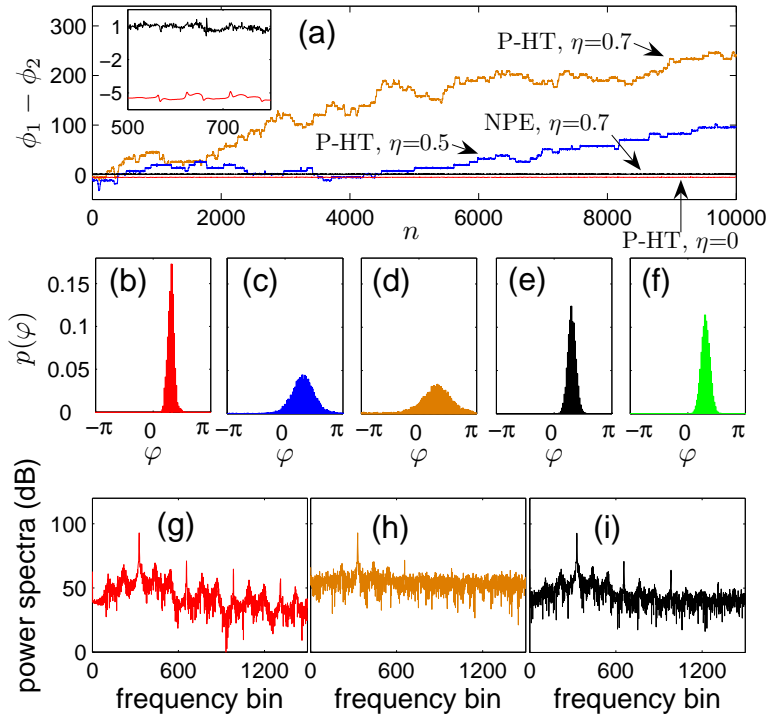


Figure 5.2: Phase synchronization of synchronous Rössler systems ( $\xi = 0.035$ ). (a) The unwrapped phase difference of the coupled systems. (b) – (d) are the distributions  $p(\varphi)$  of the wrapped phase difference of the cases  $\eta = 0$  (i.e., clean),  $\eta = 0.5$ , and  $\eta = 0.7$  by P-HT, respectively. (e) and (f) are the results of noisy data ( $\eta = 0.7$ ) by NPE and P-LP ( $\kappa = 1$ ,  $d = 80$ ,  $N = 20$ , and  $M = 5$ ), respectively. (g) – (i) are the power spectra of the clean data, noisy data ( $\eta = 0.7$ ), and the real part  $\{\bar{s}(n)\}$  of the estimated analytical signal  $\{\bar{s}^{(a)}(n)\}$  by NPE, respectively. Note that only the low frequency region of the power spectra is plotted. The power spectra of the data after noise reduction by LP are similar to that in (i), and are not plotted.

estimated by the proposed schemes is bounded around a constant which implies PS occurs in the coupled systems  $\Sigma_{1,2}$ , and the corresponding distribution  $p(\varphi)$  of the wrapped phase difference is almost as sharp as that of the clean data [Figs. 5.2(e) and 5.2(f) vs Fig. 5.2(b)]. The power spectra are also plotted for comparison. It shows that the subharmonics and subtle structures are buried by measurement noise [Fig. 5.2(g) vs Fig. 5.2(h)], while NPE and LP can recover most of them [Fig. 5.2(g) vs Fig. 5.2(i)]. If the narrow bandpass filter is applied to noisy data, all the out-band structures will be removed.

In this chapter, the synchronization index (SI) based on entropy [39,56] (see

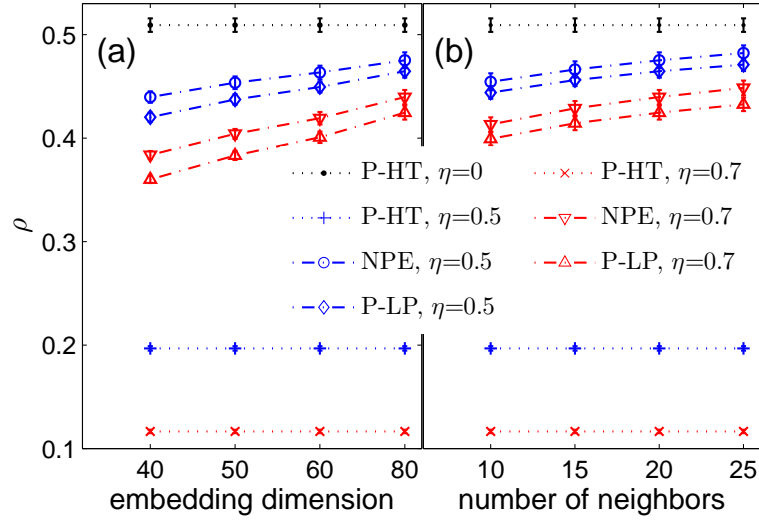


Figure 5.3: The estimated synchronization index  $\rho$  with respect to embedding dimension [(a),  $N = 20$ ] and the number of neighbors [(b),  $d = 80$ ] for synchronous Rössler systems ( $\xi = 0.035$ ). Ten realizations of each case are calculated, and their means and standard deviations are plotted. Note that similar simulations to the nonsynchronous Rössler systems ( $\xi = 0.01$ ) show that  $\rho$  increases very slowly with the increase of the value of parameters  $d$  and  $N$  (these results are not included in this thesis for brevity).

introduction of this index in Sec. 2.4.2) is used to quantify the degree of PS. It is reported that overembedding (i.e., an embedding of excessively high dimension) [57] may yield better result of noise reduction by LP [62]. For NPE and P-LP, an embedding of relatively higher dimension leads to a closer estimate of SI to that calculated from clean data [Fig. 5.3(a)], and relatively more neighbors also yield a higher estimate of SI [Fig. 5.3(b)]. For data with higher noise level, a few more neighbors may yield a little better results. For P-LP, simulation results also show that the SI decreases slowly (less than 6.2% for  $M$  from 3 to 10, when  $\eta = 0.7$ ) with respect to the increase of dimension  $M$  of the signal subspace space. Considering that the performances of the proposed schemes are not very sensitive to the values of parameters after they reach particular values, the parameters are simply set as follows:  $\kappa = 1$ ,  $d = 80$ ,  $N = 20$ , and  $M = 5$ , unless stated otherwise. More discussions on these parameters can be found in Refs. [11, 13, 62, 108].

Figure 5.4 shows the results of the proposed schemes to data with different noise levels. For both the synchronous [Fig. 5.4(a),  $\xi = 0.035$ ] and the nearly

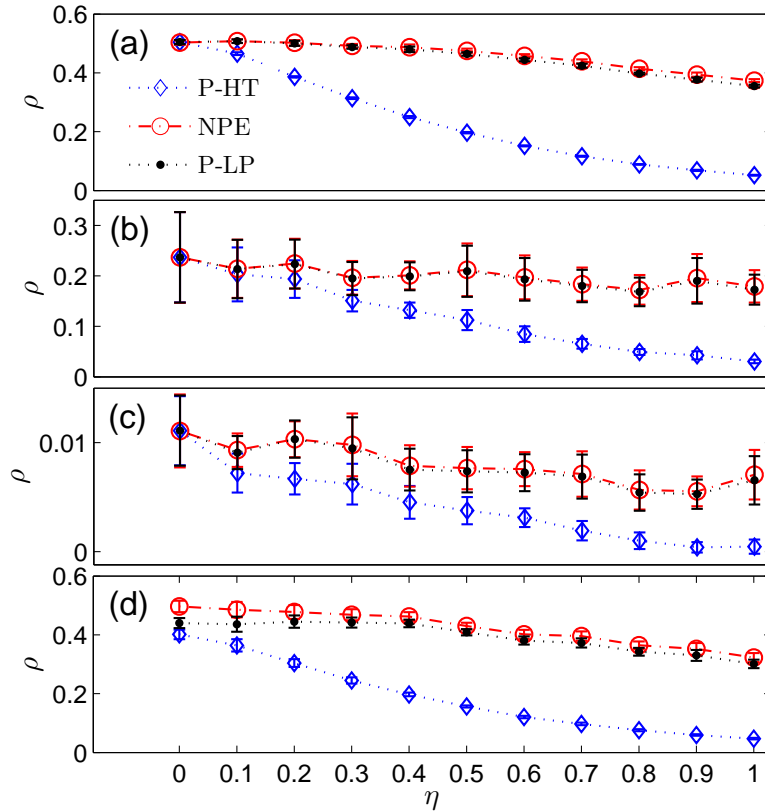


Figure 5.4: The estimated synchronization index  $\rho$  with respect to the level of measurement noise for the cases of synchronous [(a),  $\xi = 0.035$ ], nearly synchronous [(b),  $\xi = 0.027$ ], and nonsynchronous [(c),  $\xi = 0.01$ ] states, which are with only measurement noise, and the case that is also with dynamical noise [(d),  $\xi = 0.2, \sigma_{\zeta_{1,2}} = 0.1$ ]. Ten realizations of each case are calculated.

synchronous [Fig. 5.4(b),  $\xi = 0.027$ ] Rössler systems, the SIs estimated by P-HT descend quickly as the noise level increases, which may mislead that the coupled systems are nonsynchronous or weakly synchronous even though they are actually synchronous. The SIs estimated with the proposed schemes are more robust to noise, and are very close to those estimated from clean data ( $\eta = 0$ ), when the noise level is not so high [Fig. 5.4(a),  $\eta < 0.5$ ]. For the nonsynchronous systems [Fig. 5.4(c),  $\xi = 0.01$ ], the SIs estimated by the proposed schemes are also close to that calculated from clean data. For these three cases, the proposed schemes do not yield overestimation of the degree of synchronization, and thus overcome the problem of overestimation that may arise from the linear bandpass filter [56]. Note that the coupling strength of these three cases are adopted from that used in Ref. [39].

Furthermore, the proposed schemes are applied to data measured from coupled Rössler systems with dynamical noise. As Fig. 5.4(d) indicates, the SIs estimated by P-HT decrease quickly as the level of measurement noise increases. Moreover, when the level of measurement noise is not so high ( $\eta \leq 0.6$ ), the indexes are overestimated by NPE and P-LP, compared with the result of the case with no measurement noise ( $\eta = 0$ ) by P-HT. This is because the integrated data from systems with dynamical noise are not smooth, and appear to be noisy even with no measurement noise. Both NPE and P-LP can reduce the effect of coarseness in data, and thus overestimate the degree of PS. The overestimation tends to fade off as the level of dynamical noise decreases. One way to deal with data with dynamical noise is the method of *shadowing* [17], which yields a smooth shadowing trajectory that is close to the coarse trajectory. We conjecture that the SI estimated by P-HT from the shadowing trajectory may be close to the indexes estimated by NPE or P-LP from the coarse data with only dynamical noise ( $\eta = 0$ ). Here, we do not discuss shadowing in detail because it is not the focus of this thesis.

For the data measured from noncoherent systems (e.g., the funnel Rössler systems), the IP definition with the Hilbert transform is not immediately applicable, because the so estimated IP does not increase monotonically. One way to deal with this problem is to define the IP based on the concept of curvature of an arbitrary curve [43, 44]. For any two-dimensional curve  $\mathcal{C}_1 = (x, y)$  whose curvature is positive, the curve  $\mathcal{C}_2 = (\dot{x}, \dot{y})$  cycles monotonically around a fixed point, and the IP can be always defined as

$$\phi = \arctan \frac{\dot{y}}{\dot{x}}. \quad (5.10)$$

The coupled funnel Rössler systems [Eq. (6.24),  $\alpha = 0.25$ ,  $\beta = 0.2$ ,  $\gamma = 10$ , and  $\sigma_{\zeta_{1,2}} = 0$ ] are studied with this IP definition. A smaller sampling interval  $\Delta t = 0.05$  is used, so that more smooth derivatives [Eq. (5.10)] can be obtained, and 40 000 samples are measured after the transient state. Data measured from variables  $x_{1,2}$  and  $y_{1,2}$  are all added with measurement noise, i.e.,  $s_{1,2} = x_{1,2} + w_{1,2}$  and  $s_{3,4} = y_{1,2} + w_{3,4}$ , where  $w_{1,2} \sim N(0, \eta^2 \sigma_{x_{1,2}}^2)$ ,  $w_{3,4} \sim N(0, \eta^2 \sigma_{y_{3,4}}^2)$ , and  $\eta$  is the relative level of measurement noise. The LP

method <sup>2</sup> is applied to all the noisy data  $\{s_{1,2,3,4}\}$  separately, yielding the estimation of  $\{x_{1,2}\}$  and  $\{y_{1,2}\}$ , i.e.,  $\{\hat{x}_{1,2}\}$  and  $\{\hat{y}_{1,2}\}$ , respectively. Then the IPs of systems  $\Sigma_{1,2}$  are estimated via Eq. (5.10) with  $\{\hat{x}_{1,2}\}$  and  $\{\hat{y}_{1,2}\}$ , respectively. Simulation results show that some degree of PS can be detected from data (actually synchronous) when the level of measurement noise is small ( $\eta < 0.1$ ). This is because the derivative [Eq. (5.10)] is very sensitive to noise. So Eq. (5.10) seems not a robust IP definition in detecting PS of noisy data. One possible method is statistical measure of recurrences introduced recently [44]; but this method can not indicate the degree of synchronization in local time. To address this problem, PS of noncoherent coupled chaotic systems is further studied from the viewpoint of signal processing, as is presented in Chapter 6.

## 5.4 Phase synchronization of coupled Lorenz systems

In this section, the LP method is applied as a preprocessing tool in detecting PS of the data from the coupled Lorenz systems,

$$\begin{aligned}\dot{x}_{1,2} &= 10(y_{1,2} - x_{1,2}) + \xi(x_{2,1} - x_{1,2}), \\ \dot{y}_{1,2} &= (r_{1,2} - z_{1,2})x_{1,2} - y_{1,2}, \\ \dot{z}_{1,2} &= x_{1,2}y_{1,2} - \frac{8}{3}z_{1,2},\end{aligned}\tag{5.11}$$

where  $r_1 = 28$ ,  $r_2 = 28.02$ , and  $\xi = 3.8$  is the coupling strength. Ten-thousand samples are measured with sampling interval  $\Delta t = 0.04$ . In the  $(x, y)$ -plane, the Lorenz attractor has two centers of rotation [Fig. 5.5(a)], and the definition of IP with the Hilbert transform is not applicable. Considering the symmetry of the Lorenz attractor, the IP of the Lorenz oscillator can be defined with its projection on the  $(u, z)$ -plane,

$$\phi = \arctan \frac{z - z_0}{u - u_0},\tag{5.12}$$

where  $u = \sqrt{x^2 + y^2}$ ,  $u_0 = 12$ , and  $z_0 = 27$  [42].

<sup>2</sup>The parameters are set as  $N = 20$ ,  $M = 5$ ,  $\kappa = 4$ , and  $d = 80$ , so that the length of the embedding window  $(d - 1)\kappa\Delta t$  is almost equal to that used for the case of coherent Rössler systems.

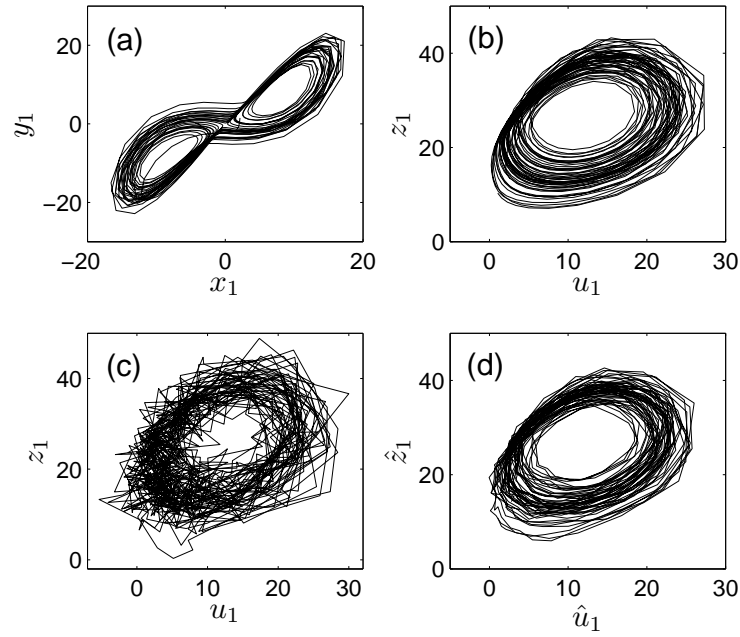


Figure 5.5: Attractors of the Lorenz system reconstructed with (a) clean Lorenz time series in the  $(x, y)$ -plane, (b) clean Lorenz time series ( $\eta = 0$ ) in the  $(u, z)$ -plane, (c) noisy Lorenz time series ( $\eta = 0.3$ ) in the  $(u, z)$ -plane, and (d) the corresponding enhanced Lorenz time series in the  $(u, z)$ -plane, respectively.

In the  $(u, z)$ -plane, the attractor constructed with clean data [Fig. 5.5(b)] rotates around one center  $(u_0, z_0)$ . Measurement noise,  $w_{1,2} \sim N(0, \eta^2 \sigma_{u_{1,2}}^2)$ ,  $w_{3,4} \sim N(0, \eta^2 \sigma_{z_{1,2}}^2)$ , are added to  $u_{1,2}$  and  $z_{1,2}$ , respectively. It can be observed that the attractor, distorted by noise [Fig. 5.5(c)], is almost recovered [Fig. 5.5(d)] after noise reduction by the LP method ( $N = 20$ ,  $M = 5$ ,  $\kappa = 1$ , and  $d = 80$ ). Note that the unwrapped phase difference fluctuates intensely [Fig. 5.6(a), “P-PP,  $\eta = 0.5$ ” and “P-PP,  $\eta = 0.7$ ”] due to measurement noise, though the coupled systems are intrinsically synchronous [Fig. 5.6(a), “P-PP,  $\eta = 0$ ”]. These fluctuations can be greatly reduced by applying the LP method, resulting in long epochs of phase locking [Fig. 5.6(a), “P-LP,  $\eta = 0.5$ ” and “P-LP,  $\eta = 0.7$ ”]. Thus PS can be detected reliably from noisy data, which is more clearly demonstrated as the results summarized in Fig. 5.6(b).

In comparison with the LP method, the effect of the bandpass filter in detecting PS is studied. The Gaussian envelop filter, introduced in Ref. [110], is applied to noisy data  $u_{1,2}$  and  $z_{1,2}$ , respectively, and the IPs are computed via Eq. (5.12) with the outputs of the filter. As Fig. 5.7 illustrates, this scheme, denoted as P-BP,

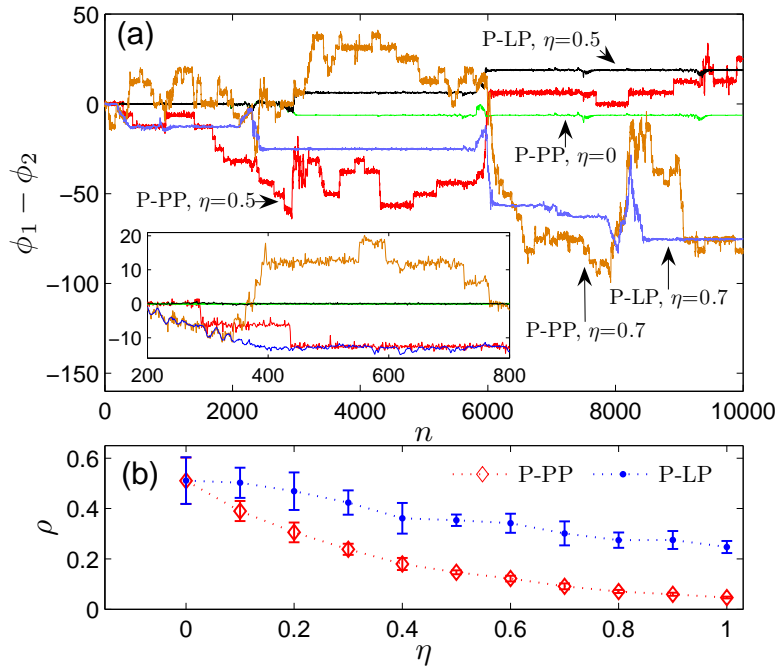


Figure 5.6: (a) The unwrapped phase difference of coupled Lorenz systems, and (b) their synchronization index  $\rho$  (ten realizations of each case) with respect to the level of measurement noise. P-PP denotes the results that the IP is defined in the projection plane [Eq. (5.12)] with no filtering to noisy data.

is sensitive to the band-width ( $\Delta f$ ) of the filter, and may overestimate the degree of synchronization even when the data is clean (P-PP,  $\eta = 0$ ).

## 5.5 Discussion and conclusion

Two schemes are proposed to detect phase synchronization (PS) from noisy chaotic data. One is the method of neighborhood-based phase estimation (NPE), the other adopts the local projection (LP) method as a preprocessing filter for noisy data. They are applied to data measured from two typical chaotic systems, i.e., the coupled Rössler systems and the coupled Lorenz systems. Simulation results show that the estimated instantaneous phase (IP) suffers much less from artificial phase slips caused by noise, and thus the degree of PS can be reliably detected even when the noise level is relatively high, avoiding the overestimation that may be introduced by the traditional linear bandpass filter. For the data

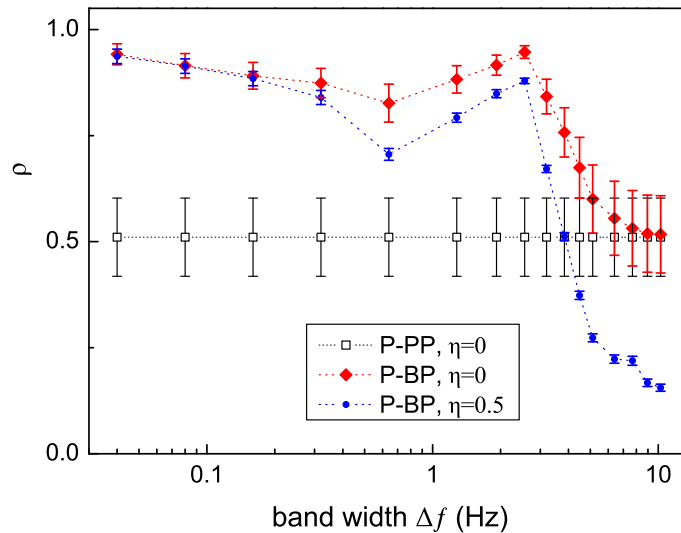


Figure 5.7: The synchronization index  $\rho$  (ten realizations of each case) with respect to the band width  $\Delta f$  of the linear bandpass filter. The center frequency of the filter is set as 1.321 Hz, where the most energetic spectra of the Lorenz time series are located around. Other details about the filter can be found in Ref. [110].

with dynamical noise as well, overestimation may be introduced when the measurement noise level is not so high because the data measured from systems with dynamical noise are coarse even when there is no measurement noise. This overestimation tends to decrease as the level of dynamical noise decreases.

State recurrence is one important feature of chaotic systems. As discussed in previous chapters, it has been utilized in analyzing and processing various theoretical and experimental systems. Actually, nonlinear interdependence [46–48] and the statistical measure of recurrences [44] both utilize the idea of state recurrence. For the framework of PS detection via localized sets [51], the typical events defined in localized sets can also be considered as generalized “recurrences”. The difference is that these “recurrences” are defined in a more generic way (e.g., by the intersection of the trajectory with a local plane) rather than by the spatial nearness of vectors in the phase space reconstructed by time delay embedding.

Both schemes proposed in this chapter utilize the redundant information of state recurrences of chaotic data. The difference is that NPE estimates IP directly

by averaging the analytical trajectories of neighbors, bridging time delay embedding to IP estimation; while the scheme incorporating LP estimates IP from data after noise reduction. In the proposed schemes, state recurrences (i.e., neighbors) are defined in the over-embedded phase space. Thus, on the one hand, the recurrences collected from noisy data are more likely to be true recurrences (the recurrences collected from clean data are considered as true recurrences here); on the other hand, the proposed schemes may not be suitable for spiking and/or bursting neurons, because spikes will dominate in collecting recurrences. It is difficult to design a method which is both robust to noise and applicable to various data. Usually, methods focus on just one point, the proposed schemes in this chapter focus on robustness.

# Chapter 6

## On phase synchronization detection

In this chapter, we examine the definition of instantaneous phase (IP) and the effect of noise in IP estimation and phase synchronization (PS) detection from the viewpoint of signal processing and circular statistics. Several definitions of IP are first revisited and further unified into a framework which defines the analytic signal via a specific bandpass filter. The effect of noise in IP estimation is studied, and the IP error, which is due to noise, is shown to obey a scale mixture of normal distributions (SMN). Further, with the assumption that the SMN of IP error can be approximated by a particular normal distribution, the estimate of mean phase coherence (MPC) is shown to be degraded by a factor which is determined only by the level of in-band noise. After that, a band-weighted synchronization index is proposed for noncoherent time series. At last, simulations are performed to test the theoretical results and the proposed index.

### 6.1 Introduction

As has been discussed in Sec. 2.4 and Chapter 5, synchronization is a cooperative behavior which means that the coupled systems evolve with the same rhythm. It ubiquitously exists in both natural and engineering systems. Examples include coupled chaotic oscillators [38], human brain activities and muscle activities [39], neuronal oscillations [53, 54], chaotic laser array [41], electro-

chemical oscillations [70], and coupled nanomechanical oscillators [71]. This phenomenon can not only reveal the mechanism and function of the coupled systems (e.g., communication during cognitive processing in human brain [54]) but also help to gain new applications such as providing clinical evidence in Parkinson's disease treatments [55]. Therefore, it has drawn increasing attention in recent years (for a review, cf. Ref. [35, 52]). To detect synchronization, various methods have been introduced [49, 51, 111]. However, to gain a reliable detection is not so easy, especially for the case when one has only the observed time series which are noncoherent and unavoidably contaminated by noise [49, 50, 112]. As introduced in Sec. 2.4.1, there are several different type of synchronization, such as complete synchronization (CS), generalized synchronization (GS), and phase synchronization (PS). Note that CS and GS is difficult to be applied to analyze bivariate time series observed from experimental systems. Nevertheless, PS, a weak form of synchronization, is a suitable tool for observed time series and has been extensively applied.

To detect PS from observed time series, an appropriate definition and estimation of instantaneous phase (IP) is very important. As mentioned in Sec. 5.1, various definitions of IP have been introduced. Most of them are based on particular transforms, such as the Hilbert transform [38], the derivative of the Hilbert transform [70], a generalized transform with Gaussian filter [41], and the wavelet transform [40], to the observed data. To the best of our knowledge, although various definitions have been proposed, there are still several key points left to be addressed. The first is how to treat noncoherent data [113]. For noncoherent data, negative instantaneous frequency (IF, defined as the derivative of the IP with respect to time), which is physically meaningless, may be introduced by the Hilbert transform [114, 115]. Usually a narrow bandpass filter is applied as preprocessing. Then the problem becomes what type of filter should be used. The second is how, quantitatively, the noise will affect the detection of PS. For contaminated data, artificial phase slips, introduced by noise, will reduce the reliability of the estimated synchronization index (SI). A bandpass pre-filtering may suppress the effect of noise, but may introduce spurious overestimation of SI as well [56]. Thus, an analytical study on the effect of noise is greatly desired. The third is that how to quantify the degree of PS on the whole. With pre-filtering, only the SI between inband components are considered and the components outside the

passband are neglected, though these neglected components may interplay and make a contribution to the interaction of the systems as a whole.

In Chapter 5, overestimation of the degree of PS has been examined in the phase space reconstructed by time delay embedding. In this chapter, the above problems are treated from the viewpoints of signal processing and circular statistics. Several definitions of IP are unified into a framework which defines IP as the argument of the signal with a specific bandpass filter applied. The role of bandpass filter is examined based on the theory of signal processing. Furthermore, an analytical study of the effect of noise after pre-filtering is given. After that, a band-weighted PS measure is proposed to quantify the degree of PS on the whole. Finally, simulations are performed to verify the analytical study of the effect of noise, and the band-weighted index is robust to noise for the cases studied.

## 6.2 Revisit the definition of instantaneous phase

The most popular definition of IP is based on the Hilbert transform. Given an observable signal  $s(t)$ , its analytic signal is defined as

$$s^{(h)}(t) = s(t) + j\tilde{s}(t) = A^{(h)}(t)e^{j\phi^{(h)}(t)}, \quad (6.1)$$

where  $A^{(h)}(t)$  is the instantaneous amplitude (IA),  $\phi^{(h)}(t)$ , which is given by

$$\phi^{(h)}(t) = \arg [s^{(h)}(t)] = \arctan \frac{\tilde{s}(t)}{s(t)}, \quad (6.2)$$

is the IP, and  $\tilde{s}(t) = \mathcal{H}[s(t)] = \frac{1}{\pi} \text{P.V.} \int_{-\infty}^{\infty} \frac{s(\tau)}{t-\tau} d\tau$  is the Hilbert transform of  $s(t)$ , in which  $\mathcal{H}(\cdot)$  denotes the operator of the Hilbert transform. The analytic signal  $s^{(h)}(t)$  can be written as the convolution of  $s(t)$  with a complex filter, i.e.,  $s^{(h)}(t) = s(t) * b^{(h)}(t)$ , where  $b^{(h)}(t) = \delta(t) + j\frac{1}{\pi t}$ . In the frequency domain,  $s^{(h)}(t)$  is  $S^{(h)}(f) = S(f)B^{(h)}(f)$ , where  $S(f)$  and  $B^{(h)}(f)$  are the Fourier transform of  $s(t)$  and  $b^{(h)}(t)$ , respectively. By definition, the analytic signal can be obtained in the frequency domain by setting the negative frequency components of the signal  $s(t)$  to be zero and doubling the amplitude of the positive frequency

components, that is, the filter  $B^{(h)}(f)$  should be

$$B^{(h)}(f) = \begin{cases} 2, & \text{if } f > 0 \\ 1, & \text{if } f = 0 \\ 0, & \text{if } f < 0. \end{cases} \quad (6.3)$$

For coherent data (i.e., with one dominated frequency component), the so defined IP increases monotonously; while for noncoherent data, the so defined IP may decrease at some instants and thus the corresponding IF may be negative, which is physically meaningless [114, 115]. For this case, IP is not a one-to-one transformation to the analytic trajectory and ambiguity occurs in PS detection [44, 113].

To deal with noncoherent data, some other methods have been proposed. One is based on the derivative of the analytic signal  $s^{(h)}(t)$  [70]. This method defines IP as  $\phi^{(d)}(t) = \arg [s^{(d)}(t)]$ , where  $s^{(d)}(t) = \frac{ds(t)}{dt} + j\frac{d\tilde{s}(t)}{dt}$ . We can write  $s^{(d)}(t)$  as  $s^{(d)}(t) = \frac{ds^{(h)}(t)}{dt} = \frac{d}{dt}[s(t) * (\delta(t) + j\frac{1}{\pi t})] = s(t) * \frac{d}{dt}[\delta(t) + j\frac{1}{\pi t}] = s(t) * b^{(d)}(t)$ , where  $b^{(d)}(t) = \delta'(t) - j\frac{1}{\pi t^2}$ . In the frequency domain,  $s^{(d)}(t)$  is  $S^{(d)}(f) = S(f)B^{(d)}(f)$ , where

$$B^{(d)}(f) = \begin{cases} j4\pi f, & \text{if } f > 0 \\ j2\pi f, & \text{if } f = 0 \\ 0, & \text{if } f < 0 \end{cases} \quad (6.4)$$

is the Fourier transform of  $b^{(d)}(t)$ . Obviously, this filter amplifies the high frequency components. Note that this IP definition is based on the idea of the curvature of an arbitrary curve [116]. If the curvature of curve  $\mathcal{C}_1 = [s(t), \tilde{s}(t)]$ , which is defined in the  $[s(t), \tilde{s}(t)]$  plane, is positive, the curve  $\mathcal{C}_2 = [\frac{ds(t)}{dt}, \frac{d\tilde{s}(t)}{dt}]$  will cycle monotonically around a fixed point, and thus the IP  $\phi^{(d)}(t) = \arg [s^{(d)}(t)]$  will increase monotonically. However, for noncoherent data, the curvature of curve  $\mathcal{C}_1$  is not always positive. For the instants the curvature turns from positive to negative, the corresponding IP will decrease. Thus this definition is not always applicable to arbitrary noncoherent data.

As discussed above, the analytic signal is obtained by apply a specific filter to the real signal  $s(t)$ . With this fact, a generalized definition of IP is proposed by applying a Gaussian filter (its envelope is a Gaussian function and thus named)

$b^{(g)}(t) = \frac{1}{\sqrt{2\pi T}} e^{-t^2/(2T^2)} e^{j2\pi f_n t}$  to  $s(t)$ , i.e.,  $s^{(g)}(t) = s(t) * b^{(g)}(t)$ <sup>1</sup> [41]. In the frequency domain,  $s^{(g)}(t)$  turns out to be  $S^{(g)}(f) = S(f)B^{(g)}(f)$ , where  $B^{(g)}(f) = e^{-2\pi^2 T^2 (f-f_n)^2}$ . Actually,  $b^{(g)}(t)$  is a narrow-band Gaussian filter (i.e.,  $\frac{1}{\sqrt{2\pi T}} e^{-t^2/(2T^2)}$ ) which is shifted by the nominal frequency<sup>2</sup>  $f_n$  in the frequency domain. Then the IP is defined as  $\phi^{(g)}(t) = \arg [s^{(g)}(t)]$ . This definition has been applied successfully in detecting PS of the coupled laser array, which the method based on the Hilbert transform straightforward has failed to reveal [41]. This is because PS only exists between the components in particular frequency band of the laser data. If the components are not extracted by the filter, then PS between them will be submerged by noise and the components in other bands, and thus cannot be detected.

Let us further give some comments on two variations of the generalized IP discussed in Ref. [41].

- The first one is with filter  $B^{(e)}(f) = 1 - j e^{j2\pi f \tau}$ . In the time domain, this filter is  $b^{(e)}(t) = \delta(t) - j\delta(t+\tau)$ , and  $s^{(e)}(t) = s(t) * b^{(e)}(t) = s(t) - js(t+\tau)$ . We can get  $s^{(e)}(t) = s(t) + js(t+\tau)$  if changing the filter a little to be  $b^{(e)}(t) = \delta(t) + j\delta(t+\tau)$ . Now the so defined IP  $\phi^{(e)}(t) = \arg [s^{(e)}(t)]$  can be interpreted as the angle of the reconstructed phase trajectory in the two-dimensional surface of time delay embedding, i.e.,  $[s(t), s(t+\tau)]$ , where  $\tau$  is time delay [11]. For some cases, e.g., the coherent Rössler system which has only one scroll, this definition works. But for signals which have broad spectra, this definition can not work according to the three physical conditions for the definition of IP (see Sec. 2.4.3). The filter  $b^{(e)}(t)$  does not null all negative frequency components, and thus  $s^{(e)}(t)$  is not guaranteed to be an analytic signal.
- The second one is with filter  $B^{(v)}(f) = 1 + 2\mu\pi f$ . In the time domain, this filter is  $b^{(v)}(t) = \delta(t) - j\mu\delta'(t)$ . With  $s^{(v)}(t) = s(t) * b^{(v)}(t) = s(t) - j\mu \frac{ds(t)}{dt}$ , the IP is defined as  $\phi^{(v)}(t) = \arg [s^{(v)}(t)]$ . This definition is similar with the one defined by the Mandelstam's method which is widely used in non-

<sup>1</sup>We note that there are some typographical errors in Ref. [70] on defining the Gaussian filter. The formulas given there are modified slightly to be consistent with other formulas in this chapter.

<sup>2</sup>The nominal frequency denotes the midpoint in the pass band, or the arithmetic mean between high and low cut off frequencies of the filter. It also denotes the desired center frequency of a crystal or oscillator.

linear oscillation theory [74]. The Mandelstam's method defines IP in the plane  $[s(t), -\frac{1}{2\pi f_n} \frac{ds(t)}{dt}]$ , where  $f_n$  is the nominal frequency of the oscillation. When  $\mu = \frac{1}{2\pi f_n}$ , these two definitions are the same. Further more, if  $\mu = 1$ ,  $\phi^{(v)}(t)$  can be interpreted as the angle of the state of displacement versus velocity. However, the negative frequency components of  $B^{(v)}(f)$  does not vanish and  $s^{(v)}(t)$  is thus not guaranteed to be an analytic signal.

One more IP definition is based on the wavelet transform [40]. With the Gabor wavelet  $\psi(t) = g(t)e^{j2\pi\nu t}$ , the wavelet transform of  $s(t)$  is  $s^{(w)}(u, a) = \int_{-\infty}^{\infty} s(t) \frac{1}{\sqrt{a}} \psi^*(\frac{t-u}{a}) dt$ , where  $g(t) = (T^2\pi)^{-1/4} e^{-t^2/(2T^2)}$  is the envelope. Let  $b_a^{(w)}(t) = \frac{1}{\sqrt{a}} \psi^*(\frac{-t}{a})$ , then

$$s^{(w)}(u, a) = \int_{-\infty}^{\infty} s(t) b_a^{(w)}(u-t) dt = s(u) * b_a^{(w)}(u).$$

Further,

$$b_a^{(w)}(u) = \frac{1}{\sqrt{a}} g\left(\frac{-u}{a}\right) e^{j2\pi\nu u/a} = \frac{1}{\sqrt{a}} g\left(\frac{u}{a}\right) e^{j2\pi\nu u/a},$$

because  $g(t)$  is symmetrical. Let  $f_n = \frac{\nu}{a}$  and  $\nu = 1$ . Then  $s^{(w)}(u, a) = s(u) * b^{(w)}(u)$ , where  $b^{(w)}(u) = f_n^{1/2} g(f_n u) e^{j2\pi f_n u}$ . The difference between  $b^{(w)}(t) = f_n^{1/2} (T^2\pi)^{-1/4} e^{-t^2 f_n^2 / (2T^2)} e^{j2\pi f_n t}$  and  $b^{(g)}(t) = \frac{1}{\sqrt{2\pi T}} e^{-t^2 / (2T^2)} e^{j2\pi f_n t}$  is the amplitude and the width of the Gaussian window, that is,  $b^{(w)}(t)$  is scaled by  $f_n$ . In the frequency domain,  $g(t)$  is  $G(f) = (4\pi T^2)^{1/4} e^{-2\pi^2 f^2 T^2}$ , and  $b^{(w)}(t)$  is  $B^{(w)}(f) = f_n^{-1/2} G(\frac{f}{f_n} - 1)$ . Therefore, this method obtains the analytic signal by applying a scaled bandpass filter to the real signal.

## 6.3 A framework for instantaneous phase definition

We can unify the IP definitions discussed above into one common framework: applying a particular filter to the observable signal  $s(t)$  and further defining the IP as the argument of the output of the filter. In this section, we study the role of the filter in defining IP and discuss the relation between IP and the Fourier transform from the viewpoint of signal processing.

In the field of signal processing, IF, which is commonly defined as the derivative of IP, is an important concept and has been widely studied [69, 74, 117, 118]. The filter  $b(t) = g(t)e^{j2\pi f_n t}$ , which has complex response, has been introduced to estimate IP [110], where  $g(t) = \frac{1}{\sqrt{2\pi T}}e^{-t^2/(2T^2)}$  is the envelope of the filter and  $T$  is response duration. In the frequency domain,  $b(t)$  is

$$\begin{aligned} B(f) &= \int_{-\infty}^{\infty} b(t)e^{-j2\pi ft} dt \\ &= \int_{-\infty}^{\infty} g(t)e^{-j2\pi(f-f_n)t} dt \\ &= G(f - f_n), \end{aligned} \quad (6.5)$$

where  $G(f) = e^{-2\pi^2 f^2 T^2}$  is the Fourier transform of  $g(t)$ . When the signal  $s(t)$  is passed through this filter, the output of the filter, i.e.,  $s^{(b)}(t) = s(t) * b(t)$ , is analytic if the band-width of the filter is smaller than  $2f_n$  [110], since its spectra at negative frequencies are eliminated by the bandpass filter<sup>3</sup>. Then IP is defined as  $\phi^{(b)}(t) = \arg[s^{(b)}(t)]$ . If the envelope  $g(t)$  is a Gaussian function, this method is exactly the one based on Gaussian filter which has been introduced in the previous section [41]. Of course, some other windows, such as the Hamming window, can be used as the envelope as well. No matter what filter is used, it is applied to constrain the output of the filter to be coherent, i.e., narrow-band with only one prominent spectral.

The analytic signal  $s^{(b)}(t) = s(t) * b(t)$  can be interpreted as a combination of the Hilbert transform and a real bandpass filter. Let  $s^{(r)}(t) = s(t) * g(t) \cos(2\pi f_n t)$ , where  $g(t) \cos(2\pi f_n t)$  is the real part of  $b(t)$ . In the frequency domain, it is

$$S^{(r)}(f) = S(f) \left[ \frac{1}{2}G(f + f_n) + \frac{1}{2}G(f - f_n) \right].$$

As Eq. (6.3) indicates, the analytic signal of  $s^{(r)}(t)$  can be obtained in the frequency domain by eliminating the negative frequency components of  $s^{(r)}(t)$  but doubling the amplitudes of the positive frequency components. Therefore, the analytic signal of  $s^{(r)}(t)$  can be obtained by the inverse Fourier transform of

---

<sup>3</sup>Note that here we consider the frequency components outside the passband are completely eliminated. In real implementation of filter, the frequency components outside the passband may not be eliminated completely, but suppressed to a very low level. So precisely speaking,  $s^{(b)}(t)$  only approximates to be analytic signal. The approximation error has been discussed in Refs. [119, 120].

$S^{(r)}(f)B^{(h)}(f)$ , i.e.,

$$\begin{aligned}
\mathcal{F}^{-1}[S^{(r)}(f)B^{(h)}(f)] &= \mathcal{F}^{-1}\left\{S(f)\left[\frac{1}{2}G(f+f_n) + \frac{1}{2}G(f-f_n)\right]B^{(h)}(f)\right\} \\
&= \mathcal{F}^{-1}[S(f)G(f-f_n)] \\
&= s(t) * \mathcal{F}^{-1}[G(f-f_n)] \\
&= s(t) * [g(t)e^{j2\pi f_n t}] \\
&= s^{(b)}(t),
\end{aligned} \tag{6.6}$$

where  $\mathcal{F}^{-1}(\cdot)$  denotes the operator of inverse Fourier transform.

As discussed in Sec. 2.4.3, the imaginary counterpart of  $s(t)$  is not obviously available. The Hilbert transform is proven to be a reasonable operator to generate the imaginary counterpart of  $s(t)$  in the sense of three physical conditions proposed for IP definition in Ref. [74]. For coherent signals, the Hilbert transform works well and the so defined IP [Eq. (6.2)] increases monotonically. But for noncoherent signals, the corresponding IP no longer increases monotonically, resulting in negative IF, which is physically meaningless. The problem can be addressed with the Bedrosian theorem [119, 120]. This theorem states that for a low-frequency term  $l(t)$  and a high-frequency term  $h(t)$  which have no spectra overlapping, the relation  $\mathcal{H}[l(t)h(t)] = l(t)\mathcal{H}[h(t)]$  holds, that is, the low-frequency term can be taken out of the Hilbert transform. For a signal of form  $s(t) = A(t) \cos \phi(t)$ ,  $A(t)$  and  $\cos \phi(t)$  are corresponding to the low-frequency term  $l(t)$  and the high-frequency term  $h(t)$ , respectively. Straightforwardly, a complex form of signal  $s(t)$  is defined as  $s_q(t) = A(t)e^{j\phi(t)}$ , which is named the quadrature model of  $s(t)$ . This model is used before the introduction of the concept of analytic signal. It seems natural to take  $\phi(t)$  as IP. However, this model does not tell how to estimate  $A(t)$  and  $\phi(t)$  from only the observable signal  $s(t)$  and thus is difficult to be applied to observed time series. There is a difference between  $s_q(t)$  and the analytic signal  $s^{(h)}(t)$  [Eq. (6.1)] which is estimated with the Hilbert transform. The energy of the difference is twice the energy of the negative frequency components of the quadrature model [120]. This difference tends to vanish as  $A(t)$  and  $\cos \phi(t)$  fulfill the Bedrosian theorem. In the other words, the more noncoherent the signal (i.e., the broader of the spectra of the signal), the bigger the difference. With this consideration, we apply bandpass filter  $b(t)$  to

the noncoherent signal, i.e.,  $s^{(b)} = s(t) * b(t)$ , so that the filtered signal satisfies the Bedrosian theorem. For the filtered signal,  $A^{(b)}(t)$  varies much more slowly than  $\cos \phi^{(b)}(t)$ , which means that the effective frequency band of  $A^{(b)}(t)$  is much lower than that of  $\cos \phi^{(b)}(t)$  [120].

The bandpass filter is used to restrict the signal so that the output of the filter satisfies the Bedrosian theorem. The effective band-width of the filter  $b(t)$  is  $\Delta f = 1/(2\sqrt{2}\pi T)$  [110]. To fulfill the Bedrosian theorem,  $\frac{\Delta f}{2}$  should be less than  $f_n$ , i.e.,  $\frac{\Delta f}{2} < f_n$ , which turns out to be  $T > 1/(4\sqrt{2}\pi f_n)$ . On the other hand, for the observable signal  $s(t)$  of time duration  $T_d$ , its physical frequency resolution of the spectra estimated by the Fourier transform is no less than  $\frac{1}{T_d}$  [67]. Therefore, the band width  $\Delta f$  must satisfy  $\Delta f > \frac{1}{T_d}$ , which turns out to be  $T < \frac{T_d}{2\sqrt{2}\pi}$ . The IF  $\frac{1}{2\pi} \frac{d\phi^{(b)}(t)}{dt}$  of the components in the pass band approaches the nominal frequency  $f_n$  in an asymptotic sense as the pass band of  $b(t)$  becomes narrower to be a delta function, i.e.,  $\delta(f - f_n)$ , in the frequency domain [69]. Note that for the method based on the wavelet transform, a similar theorem gives the condition on estimating the analytic signal  $s^{(w)}(t)$  ([121], p.91–93).

With the assumption that  $g(t)$  is symmetric, the analytic signal  $s^{(b)}(t) = s(t) * b(t)$  can be written as

$$\begin{aligned} s^{(b)}(t) &= \int_{-\infty}^{\infty} s(u)b(t-u)du \\ &= \int_{-\infty}^{\infty} s(u)g(t-u)e^{j2\pi f_n(t-u)}du \\ &= e^{j2\pi f_n t} \int_{-\infty}^{\infty} s(u)g(u-t)e^{-j2\pi f_n u}du \\ &= e^{j2\pi f_n t} S_t(f)|_{f=f_n}, \end{aligned} \quad (6.7)$$

where  $S_t(f) = \int_{-\infty}^{\infty} s(u)g(u-t)e^{-j2\pi f_n u}du$  is the short-time Fourier transform (STFT) of real signal  $s(t)$  with symmetrical Gaussian window  $g(t)$ . Note that  $S_t(f)|_{f=f_n}$  is dependent on both time  $t$  and the nominal frequency  $f_n$ . If the band width of  $S_t(f)$  is much smaller than the nominal frequency  $f_n$ , the amplitude of  $S_t(f)|_{f=f_n}$  can be considered as the amplitude of the band-limited analytic signal  $s^{(b)}(t)$ . In other words,  $s^{(b)}(t)$  can be considered as an amplitude modulated signal

with carrier frequency  $f_n$ . Then the IP can be written as

$$\begin{aligned}\phi^{(b)}(t) &= \arg[s^{(b)}] \\ &= 2\pi f_n t + \arg[S_t(f)|_{f=f_n}].\end{aligned}\quad (6.8)$$

Let us further examine two extreme cases of the bandpass filter  $b(t)$ . The first one is that the filter  $b(t)$  is an all-pass filter, i.e.,  $g(t) = \delta(t)$ . For this case, we have  $b(t) = \delta(t)e^{j2\pi f_n t} = \delta(t)$  and  $s^{(b)}(t) = s(t) * b(t) = s(t)$ . As  $s(t)$  is a real signal,  $\arg[s^{(b)}(t)] = 0$ , which gives no meaningful information of  $s(t)$ . The second extreme case is that the filter is  $b(t) = g(t)e^{j2\pi f_n t}$  with envelope  $g(t) = 1$ . In the frequency domain  $g(t)$  turns out to be  $G(f) = \delta(f)$ , which means that the filter (i.e.,  $b(t) = e^{j2\pi f_n t}$ ) is extremely narrow and let only the component of frequency  $f_n$  pass. Then we have

$$\begin{aligned}S_t(f)|_{f=f_n} &= \int_{-\infty}^{\infty} s(u)g(u-t)e^{-j2\pi f_n u} du \\ &= \int_{-\infty}^{\infty} s(u)e^{-j2\pi f_n u} du \\ &= \mathcal{F}[s(u)](f)|_{f=f_n},\end{aligned}\quad (6.9)$$

where  $\mathcal{F}[s(u)](f)$  denotes the Fourier transform of  $s(u)$ . From Eqs. (6.7) and (6.8), we get  $s^{(b)}(t) = e^{j2\pi f_n t} \mathcal{F}[s(u)](f)|_{f=f_n}$  and  $\phi^{(b)}(t) = 2\pi f_n t + \arg\{\mathcal{F}[s(u)](f)|_{f=f_n}\}$ . For this case,  $\arg\{\mathcal{F}[s(u)](f)|_{f=f_n}\}$  is dependent on  $f_n$  but not dependent on time  $t$ . The IF of the component in the pass band is  $f_b(t) = \frac{1}{2\pi} \frac{d\arg[s^{(b)}]}{dt} = f_n$ , which is actually the nominal frequency of the filter. This is obvious because

$$s^{(b)}(t) = s(t) * b(t) = \int_{-\infty}^{\infty} S(f)\delta(f-f_n)e^{j2\pi ft} df$$

is the component of frequency  $f_n$ , which is extracted from  $s(t)$  by filter  $b(t)$ . As  $g(t) \rightarrow 1$ , the filter  $b(t) \rightarrow e^{j2\pi f_n t}$ , then the analytic signal  $s^{(b)}(t)$  approaches to be  $\int_{-\infty}^{\infty} S(f)\delta(f-f_n)e^{j2\pi ft} df$  in an asymptotic sense.

Note that the relationship of techniques based on the Hilbert transform, the wavelet transform, and the Fourier transform has also been discussed from other angles [49, 122]. In Ref. [122], it is demonstrated that the spectral analysis based on the Hilbert transform, the wavelet transform, and the Fourier transform are “in

fact formally (i.e., mathematically) equivalent when using the class of wavelets that is typically applied in spectral analysis". This is true when the parameters of these three transforms are set in a particular way, and the SIs and spectral analysis based on them turn out to be equivalent to each other. But for other cases, these three transforms have their own features and advantages for specific applications. It is not appropriate to claim that they are arbitrarily equivalent. More details on the relationship between these transforms can be found in Refs. [69, 118, 122].

## 6.4 The effect of noise in phase synchronization detection

In real application, the observable signal is contaminated more or less by noise. It has been reported that the performance of various synchronization indexes, including PS indexes, can be greatly degraded when the noise level is relatively high [50]. Usually, the noisy data is pre-filtered with a bandpass filter. A data-driven optimal filter has been designed for noisy data in IP estimation [107] and some other algorithms have also been proposed to provide robust detection of PS in noisy data [44, 111]. In this section, we perform an analytical study of the effect of noise on IP estimation and PS detection.

Let  $s(t) = x(t) + w(t)$  denote the noisy signal, where  $x(t)$  is the clean signal and  $w(t)$  is the noise term. A bandpass filter  $b(t)$  is first applied to noisy signal  $s(t)$ , and the output can be written as

$$\begin{aligned} s^{(b)}(t) &= s(t) * b(t) \\ &= x(t) * b(t) + w(t) * b(t) \\ &= A_x(t)e^{j\phi_x^{(b)}(t)} + w^{(b)}(t), \end{aligned} \quad (6.10)$$

where  $w^{(b)}(t) = w(t) * b(t)$ . Let  $\hat{\phi}_x^{(b)}(t)$  denote the estimate of  $\phi_x^{(b)}(t)$  from the noisy signal  $s(t)$  and  $\theta(t) = \hat{\phi}_x^{(b)}(t) - \phi_x^{(b)}(t)$  denote the error of IP estimate due to the noise term  $w(t)$ . It has been proved that the distribution of  $\theta(t)$  is

$$p(\theta) = \frac{\exp[-A_x^2/(2\sigma_{w^{(b)}}^2)]}{2\pi} + \frac{A_x \cos \theta}{\sqrt{2\pi}\sigma_{w^{(b)}}} \operatorname{erf}\left[\frac{A_x \cos \theta}{\sigma_{w^{(b)}}}\right] \exp\left[-\frac{A_x^2 \sin^2 \theta}{2\sigma_{w^{(b)}}^2}\right], \quad (6.11)$$

where the error function is defined by  $\text{erf}(x) = \frac{1}{\sqrt{2\pi}} \int_{-\infty}^x e^{-y^2/2} dy$  and  $\sigma_{w^{(b)}}$  denotes the root-mean-square (rms) of the real part of  $w^{(b)}(t)$  [123]. When the instantaneous signal-to-noise ratio (iSNR)  $r^{(b)}(t) = A_x^2(t)/[2\sigma_{w^{(b)}}^2]$  in the pass-band is large [ $r^{(b)}(t) \geq 5$ ], the term  $\exp[-A_x^2/(2\sigma_{w^{(b)}}^2)]/(2\pi)$  in Eq. (6.11) is very small and can be neglected, the error function approximates unity and  $\sin \theta \approx \theta$ ,  $\cos \theta \approx 1$ , because  $|\theta| \ll 1$ . Then Eq. (6.11) is reduced to be a normal distribution, i.e.,  $\theta \sim N(0, \sigma_\theta^2)$ ,

$$p(\theta) = (\sqrt{2\pi}\sigma_\theta)^{-1} e^{-\theta^2/(2\sigma_\theta^2)}, \quad (6.12)$$

where  $\sigma_\theta = \sigma_{w^{(b)}}/A_x(t)$ . Since  $\theta(t)$  is an angle, its distribution can be wrapped into  $(-\pi, \pi]$  and turns out to be the wrapped normal (WN) distribution  $\Theta \sim \tilde{N}(0, \sigma_\theta^2)$ ,

$$p(\Theta) = \frac{1}{\sqrt{2\pi}\sigma_\theta} \sum_{k=-\infty}^{\infty} e^{-(\Theta+2k\pi)^2/(2\sigma_\theta^2)}, \quad (6.13)$$

where  $\Theta$  stands for the wrapped  $\theta$ , i.e.,  $\Theta = \theta \pmod{2\pi}$  [73, 124].

The WN distribution possesses the reproductive property [73]. Specifically, if  $\Theta_1 \sim \tilde{N}(\mu_1, \sigma_{\theta_1}^2)$  and  $\Theta_2 \sim \tilde{N}(\mu_2, \sigma_{\theta_2}^2)$  are independent, the relation  $(\Theta_1 - \Theta_2) \sim \tilde{N}(\mu_1 - \mu_2, \sigma_{\theta_1}^2 + \sigma_{\theta_2}^2)$  holds. Here,  $\mu_1 = 0, \mu_2 = 0$ , and thus  $(\Theta_1 - \Theta_2) \sim \tilde{N}(0, \sigma_{\theta_1}^2 + \sigma_{\theta_2}^2)$ . For the variables  $x_{1,2}(t)$  of the coupled systems [Eq. (6.24)], their IPs, i.e.,  $\hat{\phi}_{x_{1,2}}^{(b)}(t)$ , can be obtained. Let  $\varphi = \hat{\phi}_{x_1}^{(b)} - \hat{\phi}_{x_2}^{(b)}$ ,  $\hat{\varphi} = \hat{\phi}_{x_1}^{(b)} - \hat{\phi}_{x_2}^{(b)}$ ,  $\theta_1 = \hat{\phi}_{x_1}^{(b)} - \phi_{x_1}^{(b)}$ , and  $\theta_2 = \hat{\phi}_{x_2}^{(b)} - \phi_{x_2}^{(b)}$  [for brevity, the variable  $t$  in formulae such as  $\hat{\phi}_{x_1}^{(b)}(t)$  is omitted]. Then

$$\begin{aligned} \hat{\varphi} - \varphi &= [\hat{\phi}_{x_1}^{(b)} - \hat{\phi}_{x_2}^{(b)}] - [\phi_{x_1}^{(b)} - \phi_{x_2}^{(b)}] \\ &= [\hat{\phi}_{x_1}^{(b)} - \phi_{x_1}^{(b)}] - [\hat{\phi}_{x_2}^{(b)} - \phi_{x_2}^{(b)}] \\ &= \theta_1 - \theta_2. \end{aligned} \quad (6.14)$$

It is obvious that  $(\hat{\varphi} - \varphi)$  turns out to be  $(\Theta_1 - \Theta_2)$  when it is wrapped into  $(-\pi, \pi]$ , and thus obeys the WN distribution  $\tilde{N}(0, \sigma_{\theta_1}^2 + \sigma_{\theta_2}^2)$ .

Various PS indices have been proposed [49]. Two popular indices are based on entropy [39, 56] and circular statistics [72, 73], respectively (see Sec. 2.4.2). They both quantify how concentrated the distribution of phase difference is. In

this chapter, we adopt the later one <sup>4</sup>, which is called mean phase coherence (MPC) and defined as  $\rho = \|E[e^{j\varphi}]\|$ . When the observed signal is contaminated by measurement noise, the estimate of MPC is

$$\begin{aligned}\hat{\rho} &= \|E[e^{j\hat{\varphi}}]\| \\ &= \|E[e^{j[(\hat{\varphi}-\varphi)+\varphi]}\| \\ &= \|E[e^{j(\hat{\varphi}-\varphi)}]\| \cdot \|E[e^{j\varphi}]\|.\end{aligned}\tag{6.15}$$

In statistics, the characteristic function (ch.f.) of a variable  $x$  is defined as  $C_x(k) = \int_{-\infty}^{\infty} p(x)e^{jxk}dx$ , where  $p(x)$  is the probability density function (pdf) of variable  $x$ . Actually, ch.f. is the average value of  $e^{jxk}$ , i.e.,  $C_x(k) = E[e^{jxk}]$ . If  $x$  obeys the WN distribution  $x \sim \tilde{N}(\mu, \sigma^2)$ , its ch.f. is  $C_x(k) = e^{j\mu k - \sigma^2 k^2/2}$ , where  $k$  is an integer [73, 125]. As  $(\hat{\varphi} - \varphi)$  obeys the WN distribution  $\tilde{N}(0, \sigma_{\theta_1}^2 + \sigma_{\theta_2}^2)$  when it is wrapped into  $(-\pi, \pi]$ , we can get  $C_{(\hat{\varphi}-\varphi)}(k) = e^{-(\sigma_{\theta_1}^2 + \sigma_{\theta_2}^2)k^2/2}$ . Then

$$\begin{aligned}\hat{\rho} &= \|C_{(\hat{\varphi}-\varphi)}(1)\| \cdot \|E[e^{j\varphi}]\| \\ &= e^{-(\sigma_{\theta_1}^2 + \sigma_{\theta_2}^2)/2} \rho,\end{aligned}\tag{6.16}$$

which implies that the noise introduces a degrading factor, i.e.  $e^{-(\sigma_{\theta_1}^2 + \sigma_{\theta_2}^2)/2}$ , to the true index  $\rho$ , and this factor is determined by only the level of in-band noise.

Note that in Eqs. (6.11) and (6.12),  $A_x$  (as well as  $\sigma_\theta = \sigma_{w^{(b)}}/A_x$ ) is a variable of time  $t$ , i.e.,  $A_x(t)$ , if the amplitude of signal  $s^{(b)}(t)$  is not a constant. So  $\theta$  actually obeys a conditional distribution and Eq. (6.12) turns out to be

$$p(\theta|\sigma_\theta) = (\sqrt{2\pi}\sigma_\theta)^{-1} e^{-\theta^2/(2\sigma_\theta^2)}, \sigma_\theta > 0.\tag{6.17}$$

For the time series  $\{s(n)\}$  sampled from signal  $s(t)$ ,  $\theta(n)$  obeys a normal distribution with variance that varies from one sample to the next. Therefore, the distribution of IP error of the observed time series  $\{s(n)\}$  is a scale mixture of normal distributions (SMN) with different variances [126]. If the pdf of  $\{\sigma_\theta(n)\}$  is known, the empirical distribution of IP error  $\{\theta(n)\}$  for the observed time se-

---

<sup>4</sup>In Chapter 5, we adopted the index based on entropy. While in this chapter, we adopt the index based on circular statistics because it will be convenient for us to deduce the effect of noise analytically. For the index based on entropy, it is difficult, if not impossible, to deduce a analytical result on the effect of noise.

ries  $\{s(n)\}$  can be approximated as

$$p_m(\theta) = \sum_{k=1}^K p(\theta|\sigma_k)\pi_k, \quad (6.18)$$

where  $\{\pi_k\}_{k=1}^K$  is the respective empirical probabilities which are estimated from  $\{A_x(n)\}$  on a finite number of values  $\{\sigma_k\}_{k=1}^K$  [126]. This means that the distribution of  $\{\sigma_\theta(n)\}$  depends on the distribution of  $\{A_x(n)\}$ . Note that  $A_x(n)$  is the instantaneous amplitude (IA) of clean signal. Thus for observed time series  $\{s(n)\}$  which is contaminated by noise, the distribution of  $\{A_x(n)\}$  is difficult, if not impossible, to be obtained analytically. In this chapter, we do not try to find the SMN of the phase error of  $\{s(n)\}$ , but perform simulation by considering  $\sigma_\theta$  as  $\sigma_\theta = \sigma_{w(b)}/\max\{A_x(n)\}$ . In other words, the SMN of the phase error is approximated by a normal distribution with constant standard deviation  $\sigma_{w(b)}/\max\{A_x(n)\}$ . Simulations with this assumption will be performed in Sec. 6.6.1 to verify Eq. (6.16).

With the estimated  $\{\hat{\varphi}(n)\}_{n=0}^{L-1}$ , the MPC is estimated as

$$\hat{\rho} = \left\{ \left[ \frac{1}{L} \sum_{n=0}^{L-1} \cos \hat{\varphi}(n) \right]^2 + \left[ \frac{1}{L} \sum_{n=0}^{L-1} \sin \hat{\varphi}(n) \right]^2 \right\}^{1/2}, \quad (6.19)$$

where  $L$  is the number of samples in  $\{s(n)\}_{n=0}^{L-1}$ .

Note that distribution tests of PS have been investigated from other viewpoints [72, 127]. Empirical distributions of IP difference of coupled Rössler systems have been tested under the assumption that IP obeys specific distributions. But this is applicable only for special cases of PS, because the assumption of the distribution of IP is not generally valid for different systems [127]. Moreover, the IPs of different samples are assumed to be independent, which is not the case for dynamical systems. The statistical properties of MPC are investigated in Ref. [72]. The distribution of the estimated MPC is approximated by a specific distribution which is valid only for time series of a large number of samples. This distribution is dependent on two parameters, i.e., the mean angular velocity and the diffusion constant. As long as the assumptions are fulfilled and the two dependent parameters are reliably estimated, a reasonable significance level can be obtained by this model, providing a test for a non-zero synchronization index.

## 6.5 A band-weighted synchronization index

To examine the components in different frequency bands, we form a bank of bandpass filters with the same band-width  $\Delta f$  but different nominal frequency of the each filter.

Let  $s_{1,i}^{(b)}(t) = s_1(t) * b_i(t)$  denote the component of signal  $s_1(t)$  in the  $i$ th band, where  $b_i(t)$  is the  $i$ th filter with nominal frequency  $f_{n_i} = \frac{i}{2}\Delta f$ . For  $s_{1,i}^{(b)}(t)$  and  $s_{2,i}^{(b)}(t)$ , their MPC is denoted as  $\rho_i$ .

A measure relevant to  $\rho_i$  is the *coherency function*, which is defined as

$$\Gamma(f) \triangleq \frac{S_{s_1 s_2}(f)}{[S_{s_1 s_1}(f)S_{s_2 s_2}(f)]^{1/2}}, \quad (6.20)$$

where  $S_{s_1 s_2}(f)$  is the cross spectral density function

$$S_{s_1 s_2}(f) = \int_{-\infty}^{\infty} R_{s_1 s_2}(\tau) e^{-j2\pi f\tau} d\tau, \quad (6.21)$$

in which  $R_{s_1 s_2} \triangleq E[s_1(t)s_2^*(t-\tau)]$  is the cross-correlation function of  $s_1(t)$  and  $s_2(t)$  [128]. Let  $s_{1,i}(t) = \mathcal{R}[s_{1,i}^{(b)}(t)]$  and  $s_{2,i}(t) = \mathcal{R}[s_{2,i}^{(b)}(t)]$  denote the real part of the components of  $s_1(t)$  and  $s_2(t)$  in the  $i$ th frequency band, respectively, and  $R_{s_{1,i} s_{2,i}} \triangleq E[s_{1,i}(t)s_{2,i}^*(t-\tau)]$  denote the cross-correlation of  $s_{1,i}(t)$  and  $s_{2,i}(t)$ . It has been demonstrated that  $\lim_{\Delta f \rightarrow 0} \frac{1}{\Delta f} R_{s_{1,i} s_{2,i}} = S_{s_1 s_2}(f_{n_i})$ <sup>5</sup>. From this relation and Eq. (6.20), it can be inferred that the coherency function  $\Gamma(f)$  actually measures the normalized cross-correlation of the components of  $s_1$  and  $s_2$  in narrow frequency band [128]. The coherency function  $\Gamma(f)$  has been adopted as SI and is shown to be useful when synchronization occurs in particular frequency band [49].

The MPC  $\rho_i$  quantifies the degree of PS in the  $i$ th frequency band. The difference between measures  $\Gamma(f)$  and  $\rho_i$  is that the later one quantifies the cooperative behavior by only the IP difference of variables, but neglecting the effect of their IA. This is important because for the weakly coupled systems, the IAs of variables may be uncorrelated, though their corresponding IPs can be completely

<sup>5</sup>This relation is deduced with the assumption that the filter is an ideal rectangular bandpass filter.

phase-locked [38]. Actually, the main advantage of PS analysis is to characterize the interplay of the coupled systems of this case. With bandpass filter of different nominal frequency, the degree of PS in any frequency band can be estimated, just as the coherency function can quantify the cross-correlation between the components at any frequency bins.

With bandpass filter, the degree of PS of the components in the pass band can be detected. But sometimes, we may want to know how the whole coupled systems (especially when the systems are noncoherent), but not only the components in one particular frequency band, interact with each other from the viewpoint of PS. With this consideration, a band-weighted index of synchronization is defined as,

$$\tilde{\rho} = \frac{\sum_i \|E_{1,i}E_{2,i}\|^{1/2}\rho_i}{\sum_i \|E_{1,i}E_{2,i}\|^{1/2}}, \quad (6.22)$$

where  $E_{1,i}$  and  $E_{2,i}$  denote the energy of the components of  $s_1(t)$  and  $s_2(t)$  in the  $i$ th pass band, respectively. In the  $i$ th band, its MPC  $\rho_i$  contributes to  $\tilde{\rho}$  with the energy of the components in this band as weight.

## 6.6 Numerical results

### 6.6.1 Effect of noise in phase synchronization detection

In Sec. 6.4, the effect of noise in IP estimation and PS detection has been studied analytically. To validate these deduced results, we perform simulations to two typical examples: sine waves and the coupled Rössler systems.

#### 6.6.1.1 Test with sine waves

We define a simple sine wave and amplitude-modulated sine wave as

$$\begin{aligned} x_1(t) &= 10 \cos(2\pi f_1 t), \\ x_2(t) &= (10 + 4 \sin 2\pi f_a t) \cos(2\pi f_2 t + \frac{\pi}{2}), \end{aligned} \quad (6.23)$$

where  $f_1 = 2$  Hz,  $f_2 = 2$  Hz,  $f_a = 0.2$  Hz. Two 40 000-sample time series are measured from  $x_1(t)$  and  $x_2(t)$  respectively with sampling interval  $\Delta t = 0.05$ . The measured time series are denoted by  $x_{1,2}(n\Delta t)$  and their noisy versions are denoted by  $s_{1,2}(n\Delta t) = x_{1,2}(n\Delta t) + w_{1,2}(n\Delta t)$ , where  $w_{1,2}(n\Delta t)$  are the noise term and assumed to be Gaussian white noise  $w_{1,2} \sim N(0, \sigma_{w_{1,2}}^2)$ . The noise level  $\eta$  is defined as  $\sigma_{x_{1,2}} = \eta\sigma_{w_{1,2}}$ , where  $\sigma_{x_{1,2}}$  are the the variances of  $x_{1,2}$ , and  $\sigma_{w_{1,2}}$  are the variances of  $w_{1,2}$ , respectively. To simplify notation,  $\Delta t$  is omitted and  $s_{1,2}(n\Delta t)$  is written as  $s_{1,2}(n)$  from now on.

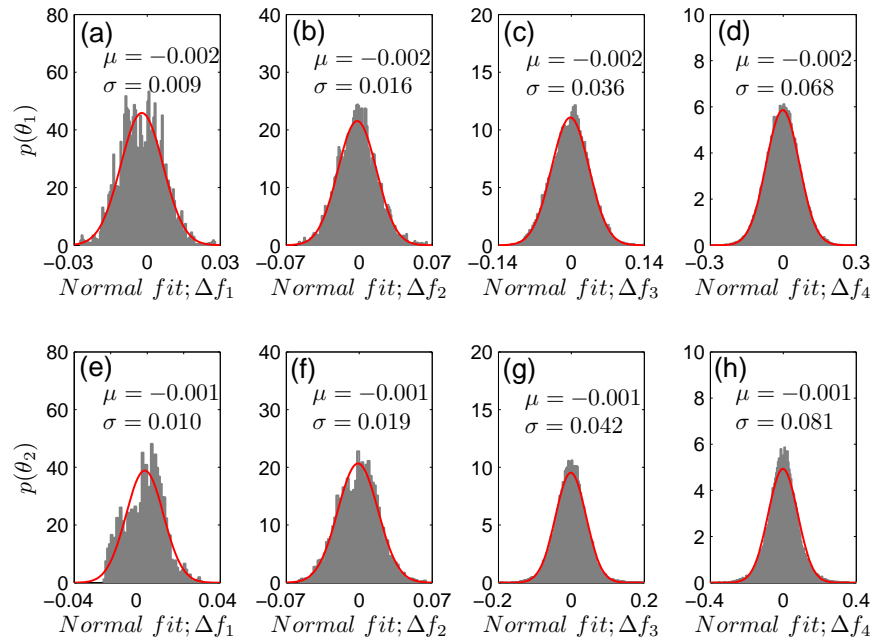


Figure 6.1: The pdf's of phase error for a sine wave and an amplitude-modulated sine wave, respectively. The red curves are the normal distribution fits of the corresponding empirical distributions. These pdf's are calculated from the clean time series  $\{x_{1,2}(n)\}$  and their corresponding noisy versions with noise level  $\eta = 0.2$ . The values of  $\mu$  and  $\sigma$  marked in each panel are the means and the standard deviations of the corresponding normal fits. The filters are with nominal frequency  $f_n = 2$  Hz and band-width: (a) and (e)  $\Delta f_1 = 0.016$  Hz, (b) and (f)  $\Delta f_2 = 0.064$  Hz, (c) and (g)  $\Delta f_3 = 0.256$  Hz, (d) and (h)  $\Delta f_4 = 1.024$  Hz. Details about the filter with Gaussian envelope can be found in Ref. [110].

The distributions of IP error  $\{\theta(n)\}$  due to the added noise are illustrated in Figs. 6.1 and 6.2. For  $x_1(t)$ , its IA is constant, and thus the distribution of IP error  $\{\theta_1(n)\}$  should be a normal distribution according to Eq. (6.13) when noise level is not high. This is verified as the results shown in Figs. 6.1(c), 6.1(d), 6.2(c),

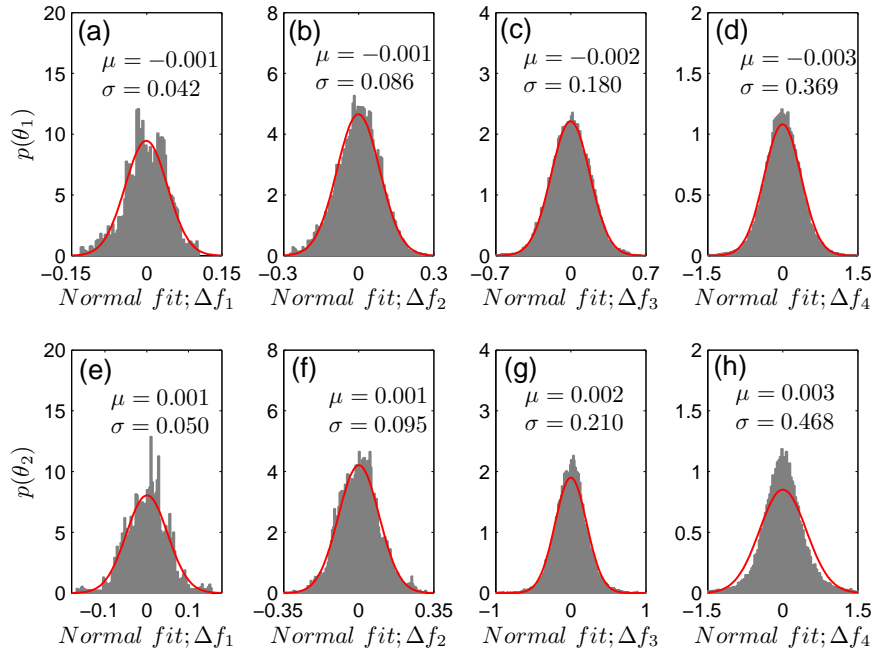


Figure 6.2: The pdf's of phase error for a sine wave and an amplitude-modulated sine wave, respectively.  $f_n = 2$  Hz,  $\Delta f_1 = 0.016$  Hz,  $\Delta f_2 = 0.064$  Hz,  $\Delta f_3 = 0.256$  Hz,  $\Delta f_4 = 1.024$  Hz,  $\eta = 1$ .

and 6.2(d). For  $x_2(t)$ , its amplitude is modulated by a sine wave, and thus its IA is not constant. Then the distribution of IP error  $\{\theta_2(n)\}$  is a SMN [Eq. (6.17)]. This leads that the corresponding empirical distributions cannot be so well fitted by particular normal distributions, as Figs. 6.1(g), 6.1(h), 6.2(g), and 6.2(h). Note that in Figs. 6.1(a), 6.1(e), 6.2(a), and 6.2(e), the empirical distributions of IP error are not a normal distribution when the band-width is very narrow. This may be due to the numerical error in simulations.

### 6.6.1.2 Test with coupled Rössler systems

To illustrate the effect of noise in PS detection and the band-weighted index, the coupled Rössler systems [39]

$$\begin{aligned}
 \dot{x}_{1,2} &= -\varpi_{1,2}y_{1,2} - z_{1,2} + \xi(x_{2,1} - x_{1,2}), \\
 \dot{y}_{1,2} &= \varpi_{1,2}x_{1,2} + \alpha y_{1,2}, \\
 \dot{z}_{1,2} &= \beta + z_{1,2}(x_{1,2} - \gamma),
 \end{aligned} \tag{6.24}$$

are taken as an example, where  $\xi$  is the coupling strength. Data are integrated from variables  $x_{1,2}$ , using the fourth-order Runge-Kutta method with sampling interval  $\Delta t = 0.05$ . The initial values are set randomly, and 40 000 samples are adopted after the transient state. Noise is added to the measured time series to generate their noisy version as that does in Sec. 6.6.1.1. Two cases of the coupled Rössler systems are studied: 1) the coherent systems with parameters  $\alpha = 0.15$ ,  $\beta = 0.2$ ,  $\gamma = 10$ ,  $\varpi_1 = 1.015$ , and  $\varpi_2 = 0.985$ ; and 2) the noncoherent systems with parameters  $\alpha = 0.25$ ,  $\beta = 0.2$ ,  $\gamma = 10$ ,  $\varpi_1 = 1.015$ , and  $\varpi_2 = 0.985$ .

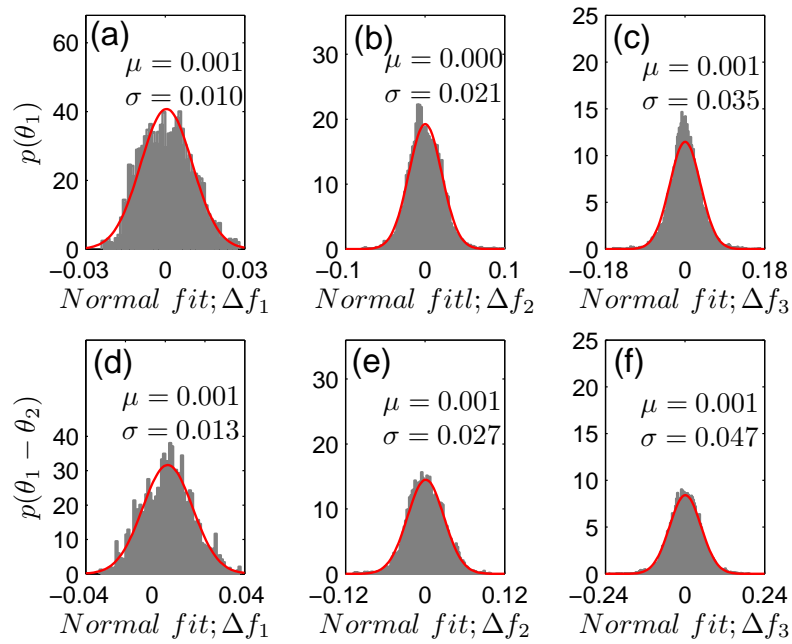


Figure 6.3: The pdf's of phase error and phase error difference for the coherent Rössler time series with bandpass filter.  $f_n = 0.1645$  Hz,  $\Delta f_1 = 0.016$  Hz,  $\Delta f_2 = 0.064$  Hz,  $\Delta f_3 = 0.256$  Hz. These pdf's are calculated from the clean Rössler time series and their corresponding noisy versions with noise level  $\eta = 0.2$ . With coupling strength  $\xi = 0.035$ , the coupled systems are synchronous.

With the coupling strength  $\xi = 0.035$ , the coherent systems are synchronized [38]. The spectral peak of the measured data is located around frequency 0.1645 Hz. So the bandpass filter of nominal frequency  $f_n = 0.1645$  Hz is utilized. Figs. 6.3 and 6.4 illustrate the distributions of phase error for different cases. We can see that in Figs. 6.3(e) and 6.3(f), the empirical distributions can be fitted appropriately by particular normal distributions; while for other figures, the empirical distributions cannot be fitted well by normal distributions. As we have

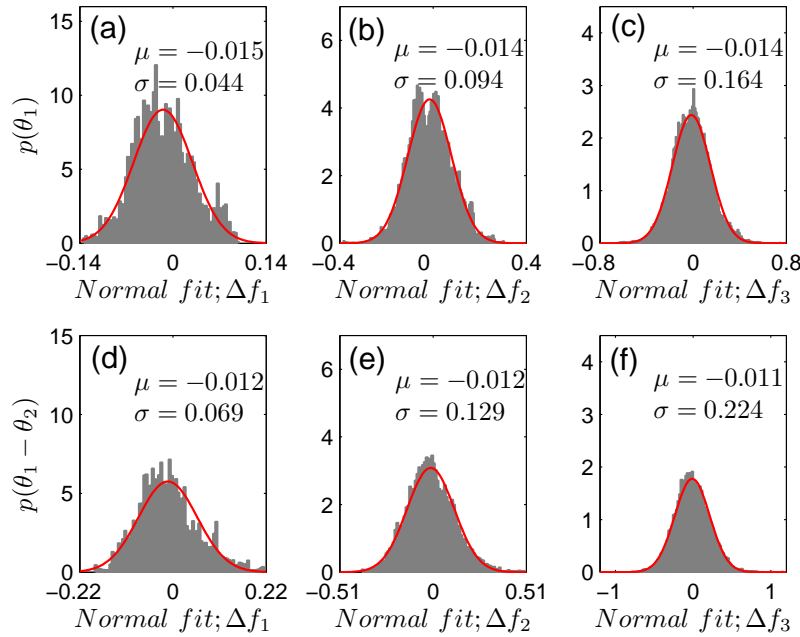


Figure 6.4: The pdf's of phase error and phase error difference for the coherent Rössler time series with bandpass filter.  $f_n = 0.1645$ ,  $\Delta f_1 = 0.016$  Hz,  $\Delta f_2 = 0.064$  Hz,  $\Delta f_3 = 0.256$  Hz,  $\eta = 1$ ,  $\xi = 0.035$ .

discussed in Sec. 6.4, the distribution of phase error is actually a scale mixture of normal distributions (SMN) which is affected by the distribution of IA  $A_x(n)$ . Generally, the distribution of phase error  $p(\theta)$  and the distribution of phase error difference  $p(\theta_1 - \theta_2)$  will not be exact normal distributions.

Figures 6.5 and 6.6 show a segment of IA and instantaneous SNR (iSNR) for different cases. We can observe that for the case with a filter of narrower band-width  $\Delta f_1$ , the fluctuation of  $A_x(n)$  is relatively smaller and slower, and the iSNR  $r^{(b)}(n)$  is bigger, correspondingly. As mentioned in Sec. 6.4, it is difficult to get an analytical form of the SMN of phase error with only an observed time series. So in studying the effect of noise in PS detection, we perform simulations under the assumption that the IA of the time series is a constant, and the SMN of the phase error can be approximated by a nominal distribution. Figs. 6.7, 6.8, 6.9, and 6.10 are the SIs of numerical estimates [i.e., estimated from the IP estimates  $\{\hat{\varphi}(n)\}$ ] and their corresponding theoretical predictions [i.e., via Eq. (6.16)] for the synchronous systems, the weakly synchronous systems, the non-synchronous systems, and the systems with no coupling, respectively. For

these coupled Rössler systems, it is shown that the theoretical predictions consist with the trends of numerical simulations. However, for coupled noncoherent Rössler systems, simulations show that the theoretical predictions are bigger than the numerical estimates, as Fig. 6.11 indicates. This is because the IAs of the case of noncoherent Rössler system are far from a constant, and thus the SMN of the phase error cannot be approximated by a normal distribution.

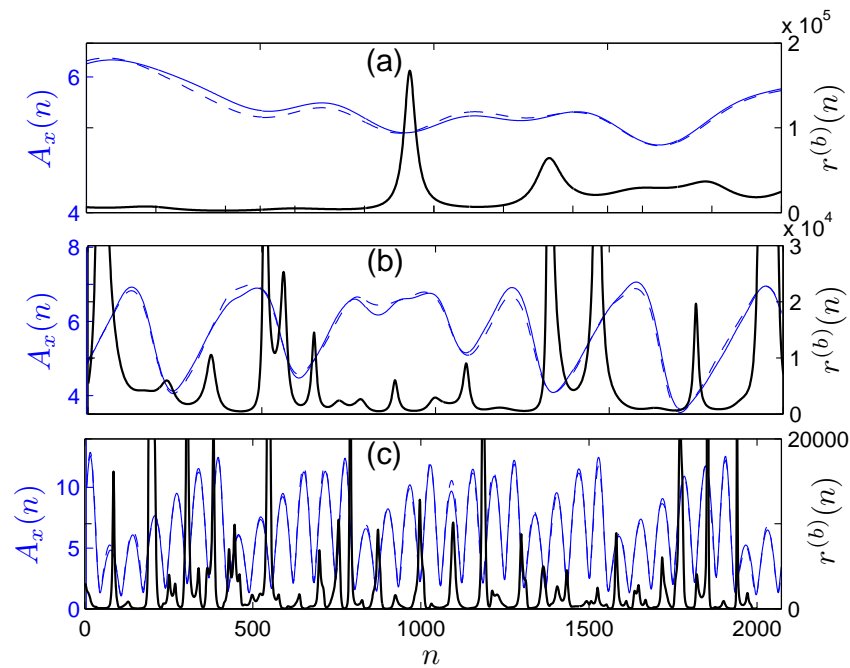


Figure 6.5: The IA  $A_x(n)$  and iSNR  $r^{(b)}(n)$  of the coherent Rössler time series with bandpass filter. The filters are with nominal frequency  $f_n = 0.1645$  Hz and band-width: (a)  $\Delta f_1 = 0.016$  Hz, (b)  $\Delta f_2 = 0.064$  Hz, and (c)  $\Delta f_3 = 0.256$  Hz. In each panel, the solid blue curve is the IA estimated from clean data, and the curve of blue dash is the IA estimated from the noisy version of the clean data, respectively. The thick black curve is the corresponding iSNR. The coupling strength is  $\xi = 0.035$  and the noise level is  $\eta = 0.2$ .

Moreover, Figs. 6.7, 6.8, 6.9, and 6.10 show that with narrower bandpass filter (i.e.,  $\Delta f_1$  and  $\Delta f_2$ ), the estimated SIs, as well as the theoretical predications, are degraded not so much even when the noise level is high. This implies that the bandpass filter is necessary and effective in dealing with data contaminated by additive noise. On the other hand, the narrower the bandpass filter, the larger the estimated SI. This overestimation of synchronization degree is introduced by the filter and has been discussed in Ref. [56]. This can be explained with the second extreme case discussed in Sec. 6.3. When the filter  $b(t)$  becomes extremely nar-

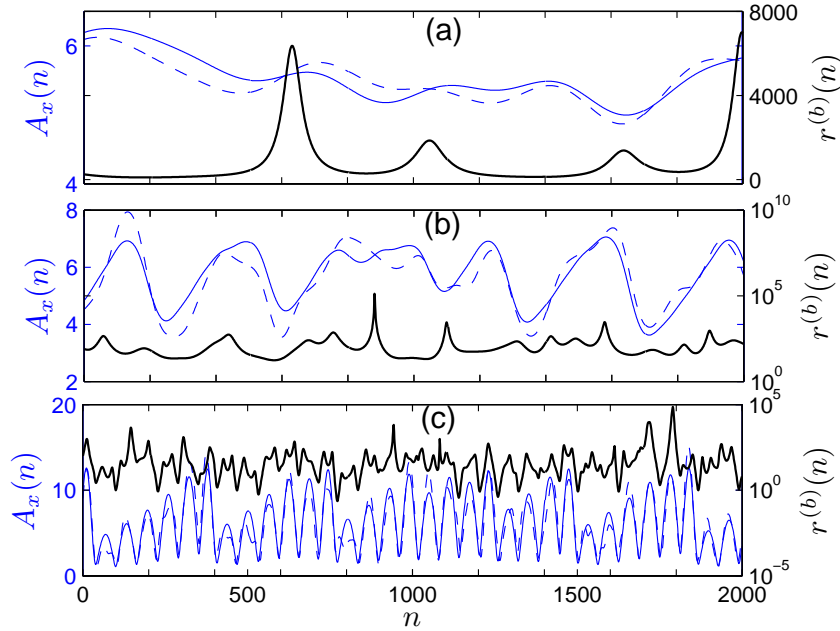


Figure 6.6: The IA  $A_x(n)$  and iSNR  $r^{(b)}(n)$  of the coherent Rössler time series with bandpass filter. The filters are with nominal frequency  $f_n = 0.1645$  Hz and band-width: (a)  $\Delta f_1 = 0.016$  Hz, (b)  $\Delta f_2 = 0.064$  Hz, and (c)  $\Delta f_3 = 0.256$  Hz. The coupling strength is  $\xi = 0.035$  and the noise level is  $\eta = 1$ .

row, i.e., a delta filter in the frequency domain, the components extracted by the filter from signals  $s_1(t)$  and  $s_2(t)$  are just the spectral components of their Fourier transform at the nominal frequency. Then the IP difference between these two components is a constant and the corresponding SI will be unity. Generally, SI is a relative measure to compare the degree of synchronization of coupled systems under different conditions (e.g., with different coupling strength). For these coupled systems, if the same bandpass filter is applied to them, the estimated SIs can indicate which coupled pairs have a higher level of synchronization than others, because the overestimation induced by the same filter is likely to be the same.

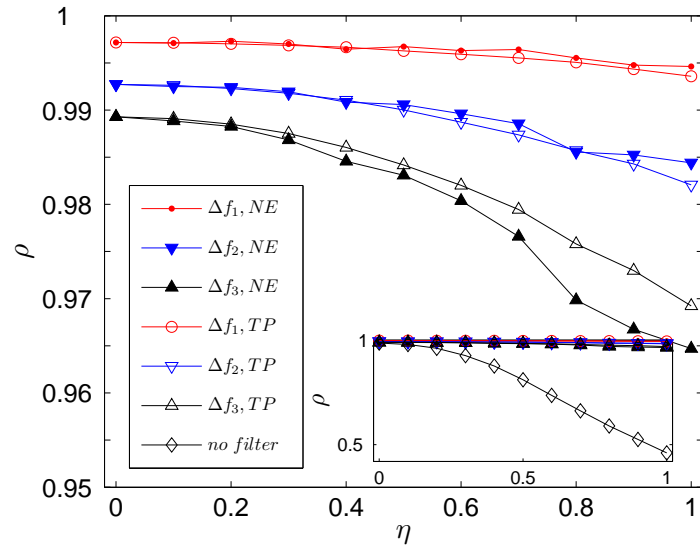


Figure 6.7: The PS index and its corresponding theoretical prediction for the coupled coherent Rössler systems with respect to the noise level  $\eta$ . NS denotes the results of numerical estimates, and TP denotes their corresponding theoretical predictions. Symbol  $\diamond$  denotes the results obtained by the Hilbert transform with no bandpass filter.  $\Delta f_1 = 0.016$  Hz,  $\Delta f_2 = 0.064$  Hz,  $\Delta f_3 = 0.256$  Hz. The coupled systems are synchronous with coupling strength  $\xi = 0.035$ .

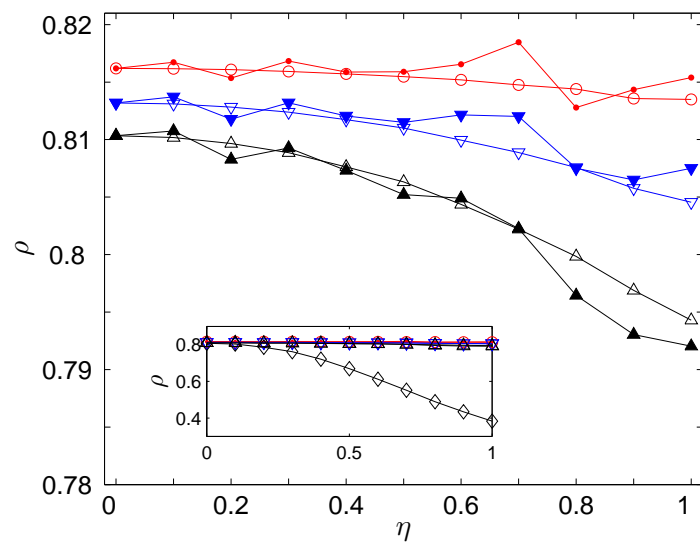


Figure 6.8: The PS index and its corresponding theoretical prediction for the coupled coherent with respect to the noise level  $\eta$ . The coupled systems are weakly synchronous with coupling strength  $\xi = 0.027$ . The denotation of each curve is as that in Fig. 6.7.

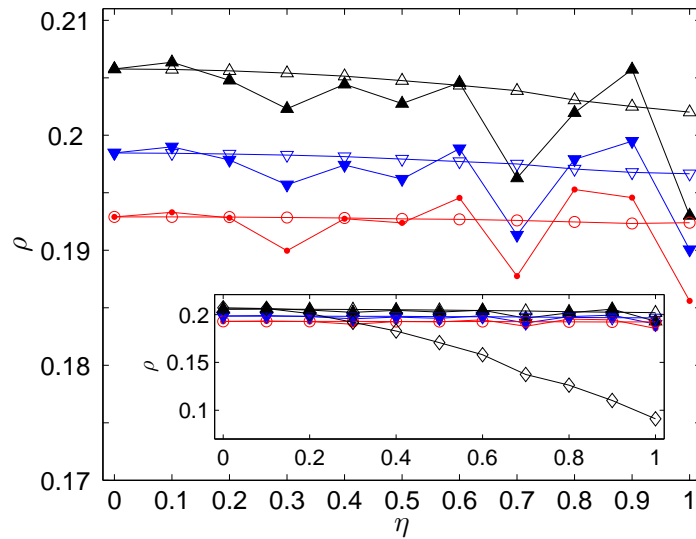


Figure 6.9: The PS index and their corresponding theoretical prediction for the coupled coherent Rössler systems with respect to the noise level  $\eta$ . The coupled systems are nonsynchronous with coupling strength  $\xi = 0.01$ . The denotation of each curve is as that in Fig. 6.7.

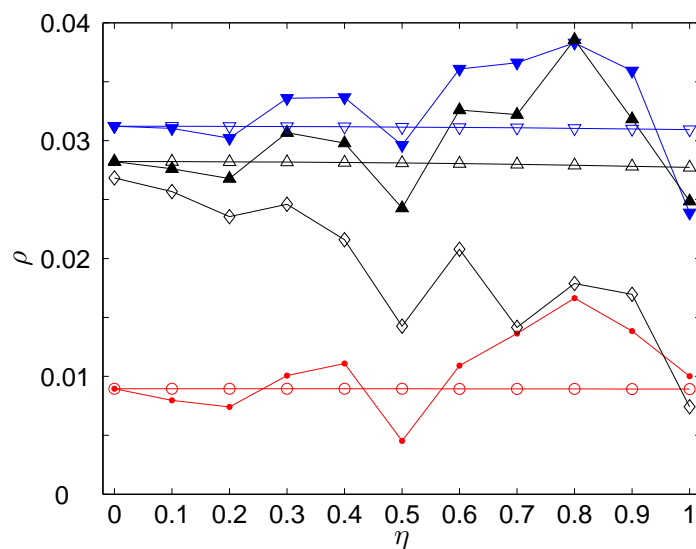


Figure 6.10: The PS index of numerical estimate and its corresponding theoretical prediction with respect to the noise level  $\eta$ . There is no coupling between the two Rössler systems, i.e.,  $\xi = 0$ . The denotation of each curve is as that in Fig. 6.7.

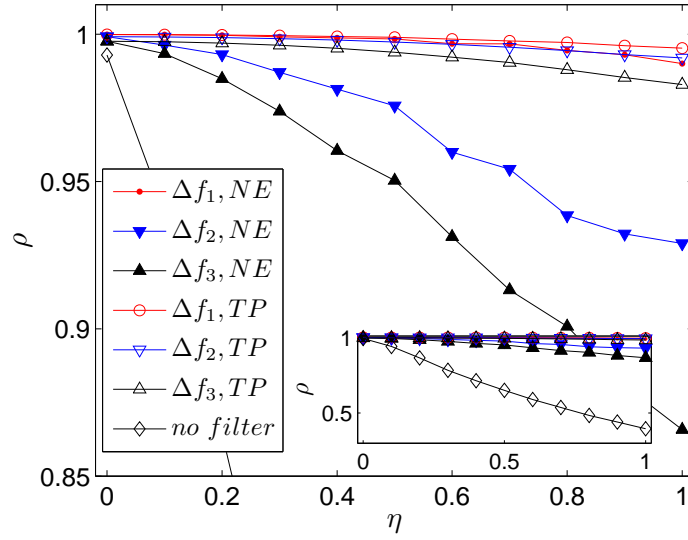


Figure 6.11: The PS index of numerical estimate and its corresponding theoretical prediction for noncoherent Rössler systems ( $\alpha=0.25$ ) with respect to the noise level  $\eta$ . The coupled systems are synchronous with coupling strength  $\xi = 0.2$ . The denotation of each curve is as that in Fig. 6.7.

### 6.6.2 Detecting synchronization with the band-weighted index

In previous sections, we use the filter  $b(t) = g(t)e^{j2\pi f_n t}$  which is with the Gaussian envelope  $g(t) = \frac{1}{\sqrt{2\pi T}}e^{-t^2/(2T^2)}$  [74]. The Bedrosian theorem [119,120] requires that there should be no overlapping spectra between the nominal frequency  $f_n$  and the spectra of  $S_t(f)|_{f=f_n}$  in estimating the analytic signal  $s^{(b)}(t)$  (see discussions in Secs. 6.3 and 6.5). The Gaussian filter can reduce the spectra that are outside the pass band to a very low magnitude but not to zero. Therefore, a certain, small, degree of error may be introduced by the filter when  $f_n$  is not much larger than  $\frac{1}{2}\Delta f$  [120]. To avoid this error and also for simplicity in numerical implementation, we use the rectangular bandpass filter in the following simulations. That is, in the frequency domain, the pass band of the  $i$ th filter  $b_i(t)$  is

$$B_i(f) = \begin{cases} 1, & \text{if } f \in [f_{n_i} - \frac{1}{2}\Delta f, f_{n_i} + \frac{1}{2}\Delta f] \\ 0, & \text{if } f \notin [f_{n_i} - \frac{1}{2}\Delta f, f_{n_i} + \frac{1}{2}\Delta f], \end{cases} \quad (6.25)$$

where  $\Delta f$  is the band-width and  $f_{n_i}$  is the corresponding nominal frequency which fulfills  $f_{n_i} \geq \frac{1}{2}\Delta f$ . Recall the discussions in Sec. 6.5, the rectangular

window is used in deducing the relation between cross-correlation and the coherency function. From this point, it is straightforward for us to use rectangular bandpass filter in detecting PS of the components in each frequency band. Then the analytic signal of the component in the  $i$ th frequency band is

$$\begin{aligned} s^{(b_i)}(t) &= \int_{-\infty}^{\infty} S(f)B_i(f)e^{j2\pi ft}df \\ &= \int_{f_{n_i}-\frac{1}{2}\Delta f}^{f_{n_i}+\frac{1}{2}\Delta f} S(f)e^{j2\pi ft}df. \end{aligned} \quad (6.26)$$

With the rectangular filter  $B_i(f)$ ,  $s^{(b_i)}(t)$  fulfills the Bedrosian theorem. In numerical implementation of Eq. (6.26), the discrete Fourier transform (DFT) is first performed to  $\{s(n)\}$ , then the analytic signal  $s^{(b_i)}(n)$  is obtained by performing inverse DFT to the frequency bins of  $\{s(n)\}$  in the  $i$ th band.

Figures 6.12 and 6.13 show the band-weighted index estimated from coherent and noncoherent Rössler systems, respectively. As Figs. 6.12(a) and 6.13(a) indicate, for the same coupling strength, the band-weighted indexes estimated with different band-width are almost the same, which implies that this index is insensitive to the value of band-width. But for noisy data, the band-weighted index is sensitive to the value of band-width. Fig. 6.12(b) and 6.13(b) give the respective differences of the band-weighted indexes estimated from clean data and their noisy version for coherent and noncoherent Rössler systems, respectively. We can see that the band-weighted index is affected much less by noise when the band-width is small. This implies that the band-weighted index, using small band-width, is robust to noise in detecting synchronization. In Fig. 6.13(a), the indexes, denoted by symbol  $\circ$ , are estimated directly with the Hilbert transform from the noncoherent Rössler time series. They are almost equal to the values of the corresponding band-weighted indexes. But we note that though these indexes do not show significant difference, there are ambiguity in defining IP with the Hilbert transform directly for noncoherent time series, as mentioned in previous sections.

For white noise, its energy distributes uniformly in each frequency band, while for signals  $x_1(t)$  and  $x_2(t)$ , their energy mainly distributes in particular frequency bands. Then in the bands containing most of the signal, the signal-to-noise ratio (SNR)  $r^{(b_i)} = (\text{mean square of } A_x^{(b_i)})/[2\sigma_w^{(b_i)}]$  will be much larger

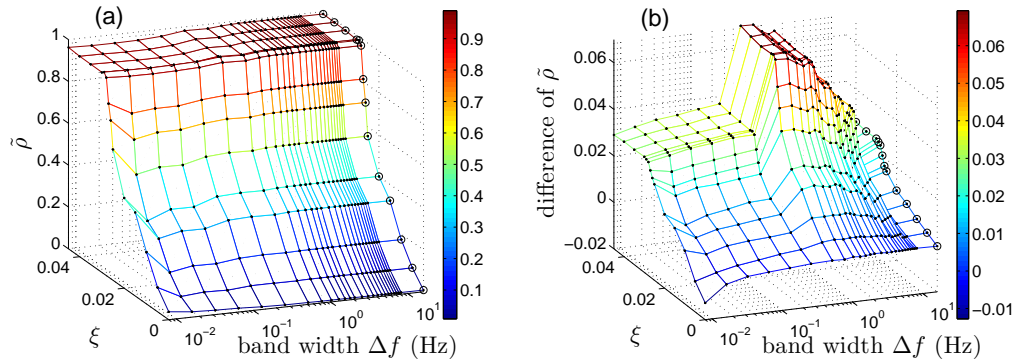


Figure 6.12: (a) The band-weighted synchronization index for coupled coherent Rössler systems ( $\alpha=0.15$ ) with respect to the coupling strength  $\xi$  and the band-width  $\Delta f$  of filter; (b) the respective differences between the indexes estimated from the clean data [i.e., the data used in panel (a)] and their noisy version ( $\eta = 0.2$ ). Symbol  $\circ$  denotes the index estimated by the Hilbert transform without bandpass filter.

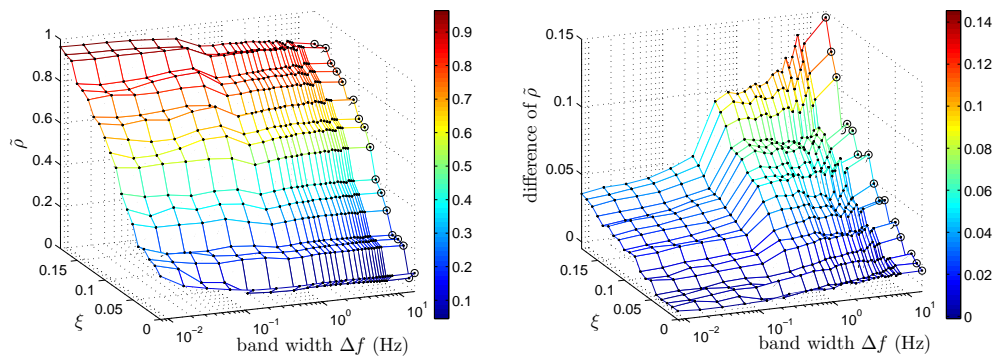


Figure 6.13: (a) The band-weighted synchronization indexes for coupled noncoherent Rössler systems ( $\alpha=0.25$ ) with respect to the coupling strength  $\xi$  and the band-width  $\Delta f$  of filter; (b) the respective differences between the indexes estimated from the clean data and their noisy version ( $\eta = 0.2$ ). Symbol  $\circ$  denotes the index estimated by the Hilbert transform without bandpass filter.

than the SNR  $r_{1,2} = (\text{mean square of } x_{1,2})/\sigma_{w_{1,2}}^2$  in the full frequency range. In these bands, the noise is reduced to a low level and thus the estimated SIs  $\hat{\rho}_i$ 's approximate  $\rho_i$ 's better. This is illustrated by Fig. 6.14. At the bands (around 0.1645 Hz) where the spectral peak locates, the estimated MPCs are affected little by the low level of in-band noise, while in other bands, the index  $\rho_i$  is greatly degraded and almost approaches zero [Fig. 6.14(b)] because of the low SNR in those bands. The bands where spectral peak locates give big weights to the corresponding MPCs which are affected by the in-band noise much less than

the MPCs of other bands in estimating the band-weighted index. As a result, the band-weighted index is robust to noise.

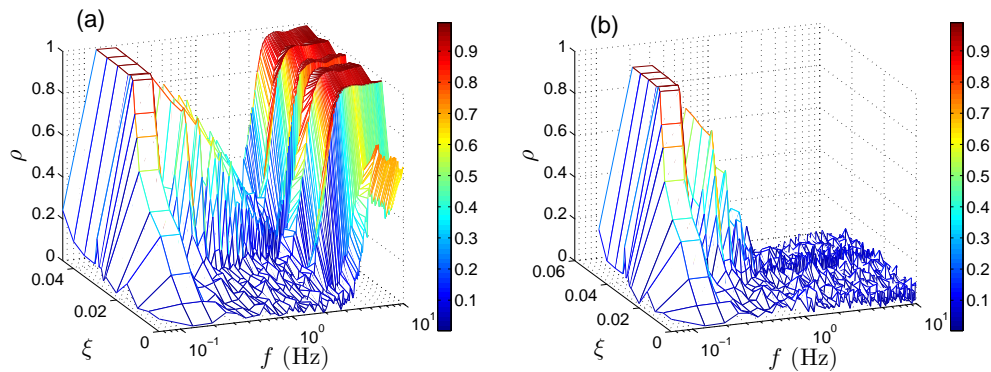


Figure 6.14: The synchronization index  $\rho_i$  for components of clean data (a) and the noisy version of the clean data (b) in each frequency band with band-width  $\Delta f = 0.128$  Hz. The coupled Rössler systems are coherent and the noise level is  $\eta = 0.2$ .

## 6.7 Synchronization in EEG signals

In Ref. [49], several synchronization measures, including linear cross-correlation, coherency function, measures of nonlinear interdependence, mutual information, indexes of PS based on the Hilbert transform and the wavelet transform, have been compared with electroencephalographic (EEG) signals recorded from rats. It is concluded that “all these measures gave a similar tendency in the synchronization levels”. To compare the band-weighted index with these measures, we apply it to the same EEG signals used in Ref. [49]. Their waveforms are plotted in Fig. 6.15. Obviously, these signals are noncoherent and may be noisy as well. These EEG signals recorded from electrodes placed on the left and right frontal cortex of rats with sampling frequency 200 Hz. The duration of each EEG pairs is 5 sec (i.e., 1000 samples).

Figure 6.16 gives the MPCs of the three pairs of EEG signals in difference frequency bands. As Fig. 6.16(a) indicates, with a larger band-width  $\Delta f = 12.8$  Hz, the degree of PS is in the order  $B > A > C$  in the frequency region below 40 Hz. With a smaller band-width  $\Delta f = 3.2$  Hz, the estimated MPCs fluctuate intensively at different frequency bands, as indicates in Fig. 6.16(b). The order

of the synchronization degree (in the frequency region below 30 Hz) indicated by MPC is consistent with that obtained by the coherency function [49].

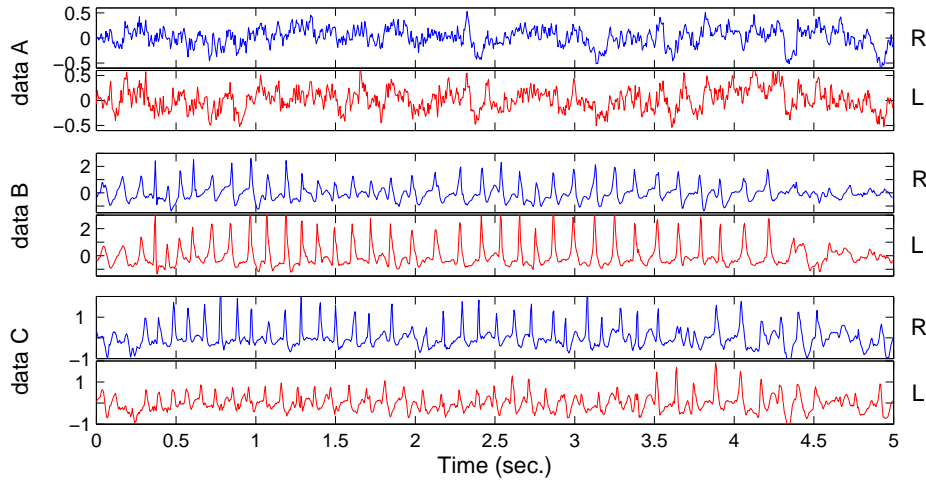


Figure 6.15: Three pairs of rat EEG signals measured from the electrodes placed on the right (R) and the left (L) cortex of rats. Data are from Ref. [49].

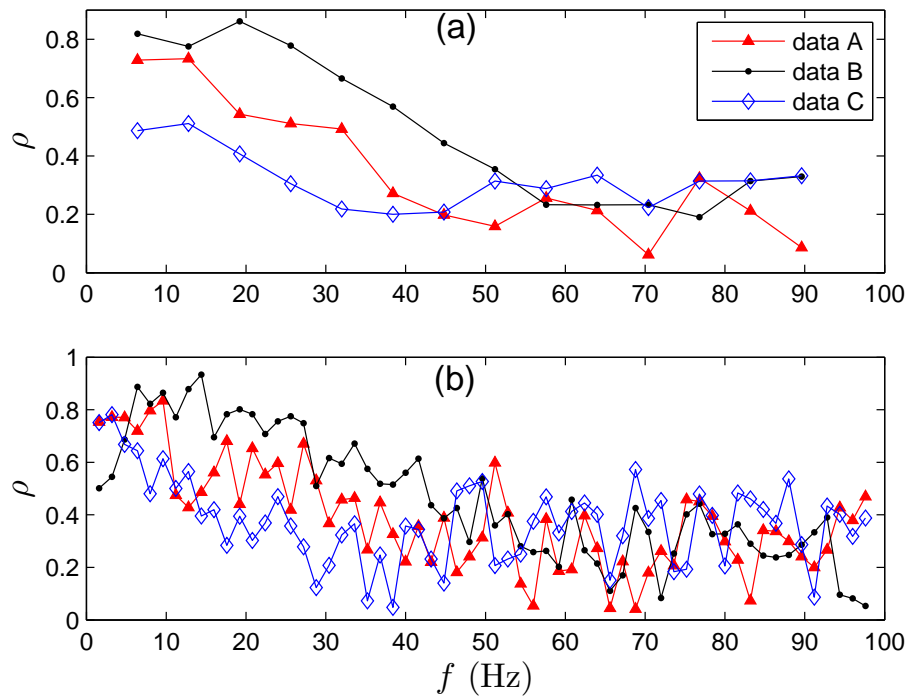


Figure 6.16: Synchronization analysis for EEG signals. (a) and (b) are the synchronization index  $\rho_i$  for components in each frequency band with band-width  $\Delta f = 12.8$  Hz and 3.2 Hz, respectively.

Further, the band-weighted index is applied to the EEG signals. Surrogate method has been applied extensively to provide significance test of the estimated synchronization index [45, 52]. In this chapter, we applied the phase shuffled surrogate method which generates surrogate data by shuffling the phase of the original data but keeping the amplitude unchanged [84]. The surrogate data have similar power spectra with that of the original data. As Figs. 6.17(a), 6.17(b), and 6.17(c) indicate, the band-weighted indexes of the three EEG pairs are much larger than that of their surrogate data. Fig. 6.17(d) gives a comparison of the degree of synchronization of the three EEG pairs which is in order  $B > A > C$ . This order, consists with that reported by other synchronization measures in Ref. [49], is clearly revealed by the band-weighted index even for the case the EEG signals are contaminated by white noise ( $\eta = 0.2$ ). The differences of the band-weighted indexes estimated from the clean signals and their corresponding noisy version are plotted in Fig. 6.17(e). We can see that as the band-width becomes narrow, the index difference shows a decreasing trend. This implies that the band-weighted index is more robust with narrow band-width. Further, a comparison of the surrogates generated from the three EEG pairs are given in Fig. 6.17(f). The band-weighted indexes of them show similar trend and the difference is small for the same band-width. In the sense of statistics, the band-weighted indexes of the surrogates show the order  $B > A > C$ , which is consistent with the order of synchronization degree of their original EEG pairs.

## 6.8 Discussion and conclusion

In this chapter, we study the definition of instantaneous phase (IP) and the effect of noise in phase synchronization (PS) detection from the viewpoint of signal processing and circular statistics. We show that several definitions of IP can be unified into one framework: applying a specific filter to the time series and defining IP as the argument of the output of the filter. With this framework, the error of the estimated IP, which is due to noise, is shown to obey a scale mixture of normal distributions (SMN). The estimate of mean phase coherence (MPC) is shown to be degraded by a factor which is determined by only the level of in-band noise, under the assumption that the instantaneous amplitude

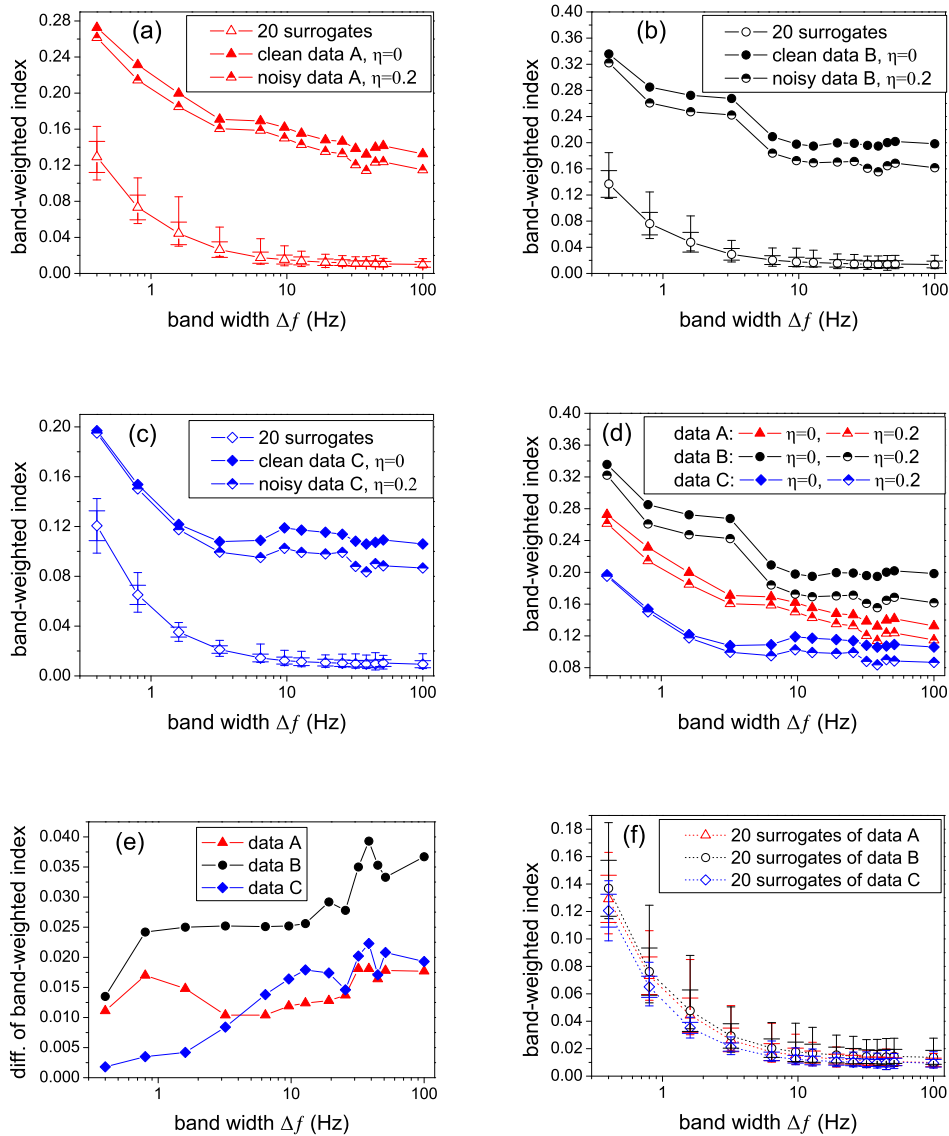


Figure 6.17: Synchronization analysis for EEG signals with the band-weighted index. (a), (b), and (c) are the band-weighted indexes for data A, data B, and data C, respectively. (d) is a comparison of synchronization degree for these three EEG pairs and (e) is the difference of the band-weighted indexes estimated from the original EEG signals and their noisy version ( $\eta = 0.2$ ). (f) is a comparison of the phase shuffled surrogates of the original EEG signals.

(IA) of the observed signal is a constant and thus the SMN of the IP error can be approximated by a normal distribution. These results are further verified by numerical simulations. But for general cases, the SMN of the IP error cannot be approximated by a normal distribution. The empirical distribution is difficult, if

not impossible, to be deduced theoretically. So for real applications, it is difficult to get a good theoretical prediction of synchronization degree. Nevertheless, the deduced analytic results can give an implication (theoretically) on how and by how much the noise affects PS detection.

Furthermore, a band-weighted synchronization index is proposed to quantify the degree of synchronization of noncoherent systems in full frequency scope from the viewpoint of PS. This index is applied to the coupled Rössler systems. Results show that this index is robust for both coherent and noncoherent Rössler time series when they are contaminated by additive white noise. Finally, this index is applied to EEG signals measured from rats. It is shown that this index can detect the degree of PS reliably.

For biomedical signals such as local field potential (LFP), their interplay and the underlying mechanism are often specific to a particular frequency band (e.g., the gamma band [129, 130]). For this case, we expect that the band-weighted index can also be adapted to the specific band and quantify the degree of synchronization of the components in it. In human brain, oscillations play an important role. Certain interaction between oscillations may be related to functional disorder. For example, excessive synchrony appears in patients with Parkinson's disease. One possible treatment for Parkinson's disease is to suppress the synchrony by a high-frequency deep-brain stimulation at both basal ganglia and cortical levels [55]. It has been shown that PS may be a powerful tool in studying the interaction between the oscillations of brain. We expect that the band-weighted synchronization index may provide new insights in examining brain signals (EEG, LFP, etc.). What's more, after the synchronization index is estimated from observed time series, the significance of the index should be tested [52, 72, 127]. In this chapter, we only use a simple surrogate method to test the significance of the estimated index. We note that there are other methods for significance test, and novel surrogate methods are desired to be designed specifically for significance test of synchronization.

# Chapter 7

## Conclusion and future work

In this thesis, we have developed several novel methods for nonlinear time series analysis and processing from the viewpoint of signal processing. State recurrence, an important feature of chaotic systems, is exploited in designing these methods. The effect of noise in PS detection is examined analytically from the viewpoint of signal processing and circular statistics. The proposed methods are first tested with toy models and further applied to various real data, including speech signals and EEG signals. In this chapter, we will summarize the original contributions of this thesis and further discuss future directions of research.

### 7.1 Contributions of the thesis

Our contributions mainly include two parts: 1) development of novel methods based on recurrences for chaotic time series and their applications for real data such as speech; and 2) analytical study on the effect of noise in instantaneous phase (IP) estimation and PS detection from the view point of signal processing. In particular, they are:

- A two-step extension of the local projection (LP) method is proposed for chaotic data which are contaminated by colored noise, exploiting the different pattern of energy distribution of colored noise and clean chaotic data

in local phase space. Further, this extension is successfully adapted to reduce noise for speech corrupted by real environment noise, giving a good example for the application of the theory of time delay embedding to real data (see Chapter 3).

- The reference phase point and its neighbors in the phase space reconstructed by time delay embedding are shown to cover data segments with similar wave form. To exploit the redundant information presents in the neighbors, a novel neighborhood-based spectral estimator is proposed for (noisy) chaotic flow. With this estimator, the relation between the theory of time delay embedding and the frequency domain is established. Time-frequency analysis with this estimator provide an alternative to distinguish noisy chaotic flow from colored noise which has similar spectra (see Chapter 4).
- A neighborhood-based method is proposed to estimate IP for data from coupled chaotic systems. Results show that this method can avoid overestimation of PS degree (see Chapter 5).
- Several definitions of IP are revisited from the viewpoint of signals processing, and further unified into one framework which generates analytic signals by applying a specific bandpass filter to the observed signal. (see Secs. 6.2 and 6.3).
- The effect of noise in estimating IP is examined analytically. The distribution of the noise induced IP error is proven to be a scale mixture of normal distribution (SMN). Under the assumption that the SMN of IP error can be approximated by a normal distribution, the estimate of the mean phase coherence is shown to be degraded by a factor which is determined by only the level of in-band noise (see Secs. 6.4 and 6.6.1).
- A band-weighted synchronization index is proposed from the viewpoint of PS in full frequency scope. It is tested on toy models and further applied to EEG signals, yielding positive results (see Sec. 6.5, 6.6.2, and 6.7).

## 7.2 Future work

Following those presented in previous chapters, some related works can be further extended. Here we give some possible directions we are interested in:

- *Quantitative analysis of the ridge pattern.* In Chapter 4, we have demonstrated that noisy chaotic flow can be distinguished from colored noise by their ridge pattern. If the ridge pattern can be quantified appropriately by a certain measure, time-frequency analysis with the neighborhood-based spectrum estimator will give more straightforward results in analyzing different data.
- *Significance test for synchronization.* It is important to know the degree of synchronization that the estimated index can indicate. Some works on significance test for synchronization have been reported [45, 52, 72, 127, 131]. Most of them are based on surrogate test [45, 52, 131]. However, few surrogate methods are designed for testing synchronization [131]. So comparison of the existing surrogate methods in detecting synchronization will be valuable. Novel surrogate methods designed specifically for synchronization test are in great desire. In Chapter 6, we only apply a simple surrogate test to the estimated band-weighted index. Following that, more works can be done.
- *Causality detection.* There are two aspects in examining the cooperative behavior of dynamical systems. One is that whether coupling is present, and if so, how strong it is. This question can be answered by synchronization analysis. The other is about coupling direction and its corresponding strength. This question is the target of causality detection, which have been a very hot topic recently for its abundant application (e.g., in studying EEG signals and neuronal oscillations). Various methods, including Granger causality [132, 133], a neighborhood-based extension of Granger causality [134], partial phase synchronization [135], partial mutual information [136], approach based on permutation information [137], and the phase-slope index [138], have been proposed to detect causality. Further

works, such as performing analysis on the effect of noise in causality detection and designing robust methods, are needed.

- *Cluster analysis for multivariate time series.* In Chapter 6, we mainly focus on synchronization of bivariate time series. But the methods for bivariate time series appear weak in studying multivariate time series (e.g., multi-channel EEG signals). For multivariate time series or a large populations of oscillators, they may all synchronize with each other or group to be independent clusters with only intra-cluster synchronization. Techniques based on entropy [139] and random matrix theory (RMT) [140] have been applied to quantify the collective behavior of EEG and neuronal populations. Different brain regions are connected in large scale and can be considered as a network [141], then the theory of complex networks can be applied to characterize the dynamics of brain activity [142]. Applications of RMT and complex networks to multivariate time series, especially biomedical signals, seems very interesting and are expected to reveal more inherent information of the underlying dynamics.

# Bibliography

- [1] E. Lorenz. Deterministic nonperiodic flow. *J. Atmos. Sci.*, 20:130–141, 1963.
- [2] E. Benincà, J. Huisman, R. Heerkloss, K. D. Jöhnk, P. Branco, E. H. van Nes, M. Scheffer, and S. P. Ellner. Chaos in a long-term experiment with a plankton community. *Nature*, 451:822–825, Feb 2008.
- [3] A. Wolf, J. B. Swift, H. L. Swinney, and J. A. Vastano. Determining Lyapunov exponents from a time series. *Physica D*, 16(3):285–317, 1985.
- [4] J.-P. Eckmann, S. Oliffson Kamphorst, and D. Ruelle. Recurrence plots of dynamical systems. *Europhys. Lett.*, 4:973–977, Nov 1987.
- [5] N. Marwan, M. Carmen Romano, M. Thiel, and J. Kurths. Recurrence plots for the analysis of complex systems. *Phys. Reports*, 438:237–329, Jan 2007.
- [6] J. B. Gao. Recurrence time statistics for chaotic systems and their applications. *Phys. Rev. Lett.*, 83(16):3178–3181, Oct 1999.
- [7] F. Takens. Detecting strange attractors in turbulence. *Lect. Notes Math.*, 898:366–381, 1981.
- [8] T. Sauer, J. A. Yorke, and M. Casdagli. Embedology. *J. Stat. Phys.*, 65:579–616, Nov 1991.
- [9] J. D. Farmer, E. Ott, and J. A. Yorke. The dimension of chaotic attractors. *Physica D*, 7:153–180, May 1983.

- [10] H. D. I. Abarbanel, R. Brown, J. J. Sidorowich, and Lev Sh. Tsimring. The analysis of observed chaotic data in physical systems. *Rev. Mod. Phys.*, 65(4):1331–1392, Oct 1993.
- [11] H. Kantz and T. Schreiber. *Nonlinear Time Series Analysis*. Cambridge University Press, 2nd edition, 2003.
- [12] A. C. Singer, G. W. Wornell, and A. V. Oppenheim. Nonlinear autoregressive modeling and estimation in the presence of noise. *Digital Signal Process.*, 4(4):207–221, 1994.
- [13] J. Sun, Y. Zhao, T. Nakamura, and M. Small. From phase space to frequency domain: A time-frequency analysis for chaotic time series. *Phys. Rev. E.*, 76(1):016220, 2007.
- [14] P. Grassberger, R. Hegger, H. Kantz, C. Schaffrath, and T. Schreiber. On noise reduction methods for chaotic data. *Chaos*, 3(2):127–141, 1993.
- [15] J. Doyne Farmer and J. J. Sidorowich. Predicting chaotic time series. *Phys. Rev. Lett.*, 59(8):845–848, Aug 1987.
- [16] Henry D. I. Abarbanel, T. A. Carroll, L. M. Pecora, J. J. Sidorowich, and L. S. Tsimring. Predicting physical variables in time-delay embedding. *Phys. Rev. E*, 49(3):1840–1853, Mar 1994.
- [17] J. Doyne Farmer and J. J. Sidorowich. Optimal shadowing and noise reduction. *Physica D*, 47(3):373–392, 1991.
- [18] R. Cawley and G.-H. Hsu. Local-geometric-projection method for noise reduction in chaotic maps and flows. *Phys. Rev. A*, 46(6):3057–3082, Sep 1992.
- [19] T. Sauer. A noise reduction method for signals from nonlinear systems. *Physica D*, 58(1-4):193–201, 1992.
- [20] T. Schreiber and P. Grassberger. A simple noise-reduction method for real data. *Phys. Lett. A*, 160:411–418, Dec 1991.
- [21] E. J. Kostelich and T. Schreiber. Noise reduction in chaotic time-series data: A survey of common methods. *Phys. Rev. E*, 48(3):1752–1763, Sep 1993.

- [22] H. Kantz, T. Schreiber, I. Hoffmann, T. Buzug, G. Pfister, L. G. Flepp, J. Simonet, R. Badii, and E. Brun. Nonlinear noise reduction: A case study on experimental data. *Phys. Rev. E*, 48(2):1529–1538, Aug 1993.
- [23] A. I. Mees and K. Judd. Dangers of geometric filtering. *Physica D*, 68(3-4):427–436, 1993.
- [24] A. Leontitsis, T. Bountis, and J. Pagge. An adaptive way for improving noise reduction using local geometric projection. *Chaos*, 14(1):106–110, 2004.
- [25] R. Hegger, H. Kantz, and L. Matassini. Noise reduction for human speech signals by local projections in embedding spaces. *IEEE Trans. Circuits Syst., I: Fundam. Theory Appl.*, 48(12):1454–1461, Dec 2001.
- [26] M. T. Johnson and R. J. Povinelli. General framework for phase synchronization through localized sets. *Physica D*, 201(3-4):306–317, 2005.
- [27] M. Richter, T. Schreiber, and D.T. Kaplan. Fetal ECG extraction with nonlinear state-space projections. *IEEE Trans. Biomed. Eng.*, 45(1):133–137, Jan 1998.
- [28] R. Hegger, H. Kantz, and L. Matassini. Denoising human speech signals using chaoslike features. *Phys. Rev. Lett.*, 84(14):3197–3200, Apr 2000.
- [29] D. Sigeti and W. Horsthemke. High-frequency power spectra for systems subject to noise. *Phys. Rev. A*, 35(5):2276–2282, Mar 1987.
- [30] V. Brunsten and P. Holmes. Power spectra of strange attractors near homoclinic orbits. *Phys. Rev. Lett.*, 58(17):1699–1702, Apr 1987.
- [31] J. Doyne Farmer. Spectral broadening of period-doubling bifurcation sequences. *Phys. Rev. Lett.*, 47(3):179–182, Jul 1981.
- [32] J. Crutchfield, D. Farmer, N. Packard, R. Shaw, G. Jones, and R. J. Donnelly. Power spectral analysis of a dynamical system. *Phys. Lett. A*, 76:1–4, Mar 1980.
- [33] R. S. Dumont and P. Brumer. Characteristics of power spectra for regular and chaotic systems. *J. Chem. Phys.*, 88(3):1481–1496, 1988.

- [34] C. Chandre, S. Wiggins, and T. Uzer. Time-frequency analysis of chaotic systems. *Physica D*, 181:171–196, Jul 2003.
- [35] A. Pikovsky, M. Rosenblum, and J. Kurths. *Synchronization: A Universal Concept in Nonlinear Sciences*. Cambridge University Press, UK, 2001.
- [36] L. M. Pecora and T. L. Carroll. Synchronization in chaotic systems. *Phys. Rev. Lett.*, 64(8):821–824, Feb 1990.
- [37] M. D. S. Vieira, P. Khoury, A. J. Lichtenberg, M. A. Lieberman, W. Wonchoba, J. Gullicksen, J. Y. Huang, R. Sherman, and M. Steinberg. Numerical and experimental studies of selfsynchronization and synchronized chaos. *Int. J. Bifurc. Chaos*, 2(3):645–657, 1992.
- [38] M. G. Rosenblum, A. S. Pikovsky, and J. Kurths. Phase synchronization of chaotic oscillators. *Phys. Rev. Lett.*, 76(11):1804–1807, Mar 1996.
- [39] P. Tass, M. G. Rosenblum, J. Weule, J. Kurths, A. Pikovsky, J. Volkmann, A. Schnitzler, and H.-J. Freund. Detection of  $n : m$  phase locking from noisy data: Application to magnetoencephalography. *Phys. Rev. Lett.*, 81(15):3291–3294, Oct 1998.
- [40] A. E. Hramov and A. A. Koronovskii. An approach to chaotic synchronization. *Chaos*, 14:603, 2004.
- [41] D. J. DeShazer, R. Breban, E. Ott, and R. Roy. Detecting phase synchronization in a chaotic laser array. *Phys. Rev. Lett.*, 87(4):044101, Jul 2001.
- [42] A. S. Pikovsky, M. G. Rosenblum, G. V. Osipov, and J. Kurths. *Physica D*, 104:219, 1997.
- [43] J. Y. Chen, K. W. Wong, and J. W. Shuai. Properties of phase locking with weak phase-coherent attractors. *Phys. Lett. A*, 285(5-6):312–318, 2001.
- [44] J. Kurths, M. C. Romano, M. Thiel, G. V. Osipov, M. V. Ivanchenko, I. Z. Kiss, and J. L. Hudson. Synchronization analysis of coupled noncoherent oscillators. *Nonlinear Dyn.*, 44:135–149, 2006.
- [45] M. Palus. Detecting phase synchronization in noisy systems. *Phys. Lett. A*, 235:341–351, 1997.

- [46] J. Arnhold, P. Grassberger, K. Lehnertz, and C. E. Elger. *Physica D*, 134:419, 1999.
- [47] X. Hu and V. Nenov. Robust measure for characterizing generalized synchronization. *Phys. Rev. E*, 69(2):026206, 2004.
- [48] M. A. Kramer, E. Edwards, M. Soltani, M. S. Berger, R. T. Knight, and A. J. Szeri. Synchronization measures of bursting data: Application to the electrocorticogram of an auditory event-related experiment. *Phys. Rev. E*, 70(1):011914, Jul 2004.
- [49] R. Quiñero, A. Kraskov, T. Kreuz, and P. Grassberger. Performance of different synchronization measures in real data: A case study on electroencephalographic signals. *Phys. Rev. E*, 65(4):041903, Mar 2002.
- [50] T. Kreuz, F. Mormann, R. G. Andrzejak, A. Kraskov, K. Lehnertz, and P. Grassberger. *Physica D*, 225:29, 2007.
- [51] T. Pereira, M. S. Baptista, and J. Kurths. General framework for phase synchronization through localized sets. *Phys. Rev. E*, 75:026216, Feb 2007.
- [52] J. M. Hurtado, L. L. Rubchinsky, and K. A. Sigvardt. Statistical method for detection of phase-locking episodes in neural oscillations. *J. Neurophysiol.*, 91:1883 – 1898, 2004.
- [53] M. Le Van Quyen and A. Bragin. Analysis of dynamic brain oscillations: methodological advances. *Trends Neurosci.*, 30(7):365–373, Jul 2007.
- [54] R. T. Canolty, E. Edwards, S. S. Dalal, M. Soltani, S. S. Nagarajan, H. E. Kirsch, M. S. Berger, N. M. Barbaro, and R. T. Knight. High gamma power is phase-locked to theta oscillations in human neocortex. *Science*, 313(5793):1626–1628, 2006.
- [55] C. Hammond, H. Bergman, and P. Brown. Pathological synchronization in parkinson’s disease: networks, models and treatments. *Trends Neurosci.*, 30(7):357–364, Jul 2007.
- [56] L. Xu, Z. Chen, K. Hu, H. E. Stanley, and P. Ch. Ivanov. Spurious detection of phase synchronization in coupled nonlinear oscillators. *Phys. Rev. E*, 73(6):065201(R), 2006.

- [57] R. Hegger, H. Kantz, L. Matassini, and T. Schreiber. Coping with non-stationarity by overembedding. *Phys. Rev. Lett.*, 84(18):4092–4095, May 2000.
- [58] M. B. Kennel, R. Brown, and H. D. I. Abarbanel. Determining embedding dimension for phase-space reconstruction using a geometrical construction. *Phys. Rev. A*, 45(6):3403–3411, Mar 1992.
- [59] J. B. Gao. Detecting nonstationarity and state transitions in a time series. *Phys. Rev. E*, 63(6):066202, May 2001.
- [60] M. Little, P. McSharry, S. Roberts, D. Costello, and I. Moroz. Exploiting nonlinear recurrence and fractal scaling properties for voice disorder detection. *Biomed. Eng. Online*, 6(1), 2007.
- [61] T. Schreiber and D. T. Kaplan. Nonlinear noise reduction for electrocardiograms. *Chaos*, 6(1):87–92, 1996.
- [62] J. Sun, N. Zheng, and X. Wang. Enhancement of chinese speech based on nonlinear dynamics. *Signal Process.*, 87(10), 2007.
- [63] Y. Ephraim and H. L. Van Trees. A signal subspace approach for speech enhancement. *IEEE Trans. Speech and Audio Process.*, 3(4):251–266, Jul 1995.
- [64] X. Luo, J. Zhang, and M. Small. Optimal phase-space projection for noise reduction. *Phys. Rev. E*, 72(4):046710, 2005.
- [65] A. A. Tsonis and J. B. Elsner. Nonlinear prediction as a way of distinguishing chaos from random fractal sequences. *Nature*, 358:217–220, Jul 1992.
- [66] B. Boashash, editor. *Time frequency signal analysis and processing: a comprehensive reference*. Elsevier Ltd., 2003.
- [67] S. J. Orfanidis. *Introduction to signal processing*. Prentice Hall, Inc., 1996.
- [68] M. H. Hayes. *Statistical Digital Signal Processing and Modeling*. John Wiley & Sons., Inc., 1996.

- [69] L. Cohen. *Time-Frequency Analysis*. Englewood Cliffs, NJ: Prentice-Hall, 1995.
- [70] I. Z. Kiss, Q. Lv, and J. L. Hudson. Synchronization of non-phase-coherent chaotic electrochemical oscillations. *Phys. Rev. E*, 71:035201(R), 2005.
- [71] S.-B. Shim, M. Imboden, and P. Mohanty. Synchronized oscillation in coupled nanomechanical oscillators. *Science*, 316(5821):95–99, 2007.
- [72] B. Schelter, M. Winterhalder, J. Timmer, and M. Peifer. Testing for phase synchronization. *Phys. Lett. A*, 366:382–390, 2007.
- [73] S. Rao Jammalamadaka and A. SenGupta. *Topics in Circular Statistics*. World Scientific Publishing Co. Pte. Ltd., Singapore, 2001.
- [74] D. Vakman. On the analytic signal, the teager-kaiser energy algorithm, and other methods for defining amplitude and frequency. *IEEE Trans. Signal Process.*, 44(4):791–797, 1996.
- [75] J. S. Lim and A. V. Oppenheim. Enhancement and bandwidth compression of noisy speech. *Proc. IEEE*, 67(12):1586–1604, Dec 1979.
- [76] Y. Hu and P. C. Loizou. A generalized subspace approach for enhancing speech corrupted by colored noise. *IEEE Trans. Speech and Audio Process.*, 11(4):334–341, Jul 2003.
- [77] D. A. Berry, H. Herzel, I. R. Titze, and K. Krischer. Interpretation of biomechanical simulations of normal and chaotic vocal fold oscillations with empirical eigenfunctions. *J. Acoust. Soc. Am.*, 95(6):3595–3604, 1994.
- [78] S. S. Narayanan and A. A. Alwan. A nonlinear dynamical systems analysis of fricative consonants. *J. Acoust. Soc. Am.*, 97(4):2511–2524, 1995.
- [79] I. Steinecke and H. Herzel. Bifurcations in an asymmetric vocal-fold model. *J. Acoust. Soc. Am.*, 97(3):1874–1884, 1995.
- [80] A. Kumar and S. K. Mullick. Nonlinear dynamical analysis of speech. *J. Acoust. Soc. Am.*, 100(1):615–629, 1996.

- [81] M. Banbrook, S. McLaughlin, and I. Mann. Speech characterization and synthesis by nonlinear methods. *IEEE Trans. Speech and Audio Processing*, 7(1):1–17, Jan 1999.
- [82] R. J. Povinelli, M. T. Johnson, A. C. Lindgren, F. M. Roberts, and J. Ye. Statistical models of reconstructed phase spaces for signal classification. *IEEE Trans. Signal Process.*, 54(6):2178–2186, Jun 2006.
- [83] M. Schroeder. *Fractals, Chaos, Power Laws*. W. H. Freeman, New York, 1991.
- [84] J. Theiler, S. Eubank, A. Longtin, B. Galdrikian, and J. Doyné Farmer. Testing for nonlinearity in time series: the method of surrogate data. *Physica D*, 58(1-4):77–94, 1992.
- [85] O. E. RöSSLer. An equation for continuous chaos. *Phys. Lett. A*, 57:397–398, Jul 1976.
- [86] H. Hirsch and D. Pearce. The aurora experimental framework for the performance evaluation of speech recognition systems under noisy conditions. *ISCA ITRW ASR2000, 2000, Paris, France*.
- [87] Y. Hu and P. Loizou. Subjective comparison of speech enhancement algorithms. In *Proceedings of ICASSP*, volume I, pages 153–156, 2006.
- [88] W. Pachtl, G. Urbanek, and E. Rothausser. Preference evaluation of a large set of vocoded speech signals. *IEEE Trans. Audio and Electroacoustics*, 19(3):216–224, Sep 1971.
- [89] Y. Ephraim and D. Malah. Speech enhancement using a minimum mean-square error log-spectral amplitude estimator. *IEEE Trans. Acoustics, Speech, and Signal Proces.*, 33(2):443–445, Apr 1985.
- [90] J. H. L. Hansen and B. Pellom. Subjective comparison of speech enhancement algorithms. In *CSLP-98*, Sydney, Australia, 1998.
- [91] Y. Hu and P. Loizou. Evaluation of objective measures for speech enhancement. In *Proceedings of INTERSPEECH-2006*, Philadelphia, PA, Sep 2006.

- [92] ITU-T P.862. Perceptual evaluation of speech quality (pesq), and objective method for end-to-end speech quality assessment of narrowband telephone networks and speech codecs. *ITU-T Recommendation P.862*, 2000.
- [93] M. Small and C.K. Tse. Detecting determinism in time series: the method of surrogate data. *IEEE Trans. Circuits Syst., I: Fundam. Theory Appl.*, 50(5):663–672, May 2003.
- [94] S. M. Kay. *Modern Spectral Estimation*. Prentice Hall, 1988.
- [95] G. J. Ortega. Invariant measures as lagrangian variables: Their application to time series analysis. *Phys. Rev. Lett.*, 77(2):259–262, Jul 1996.
- [96] J.-L. Chern, J.-Y. Ko, J.-S. Lih, H.-T. Su, and R.-R. Hsu. Recognizing hidden frequencies in a chaotic time series. *Phys. Lett. A*, 238:134–140, Feb 1998.
- [97] A. M. Fraser and H. L. Swinney. Independent coordinates for strange attractors from mutual information. *Phys. Rev. A*, 33(2):1134–1140, Feb 1986.
- [98] C. Sparrow. An introduction to the lorenz equations. *IEEE Trans. Circuits and Syst.*, 30(8):533–542, Aug 1983.
- [99] U. Hübner, N. B. Abraham, and C. O. Weiss. Dimensions and entropies of chaotic intensity pulsations in a single-mode far-infrared NH<sub>3</sub> laser. *Phys. Rev. A*, 40(11):6354–6365, Dec 1989.
- [100] T. Matsumoto, L. Chua, and M. Komuro. The double scroll. *IEEE Trans. Circuits and Syst.*, 32(8):797–818, Aug 1985.
- [101] M. C. Mackey and L. Glass. Oscillation and chaos in physiological control systems. *Science*, 197:287–289, Jul 1977.
- [102] O. Miramontes and P. Rohani. Estimating  $1/f$  scaling exponents from short time-series. *Physica D*, 166:147–154, Jun 2002.
- [103] J. Gao, J. Hu, W.-W. Tung, Y. Cao, N. Sarshar, and V. P. Roychowdhury. Assessment of long-range correlation in time series: How to avoid pitfalls. *Phys. Rev. E*, 73(1):016117, 2006.

- [104] G. A. Gottwald and I. Melbourne. A new test for chaos in deterministic systems. *Proc. R. Soc. London, Ser. A*, 460:603–611, 2004.
- [105] J. Hu, W.-W. Tung, J. Gao, and Y. Cao. Reliability of the 0-1 test for chaos. *Phys. Rev. E*, 72(5):056207, 2005.
- [106] J. B. Gao, J. Hu, W. W. Tung, and Y. H. Cao. Distinguishing chaos from noise by scale-dependent lyapunov exponent. *Phys. Rev. E*, 74(6):066204, 2006.
- [107] A. G. Rossberg, K. Bartholomé, and J. Timmer. Data-driven optimal filtering for phase and frequency of noisy oscillations: Application to vortex flow metering. *Phys. Rev. E*, 69(1):016216, 2004.
- [108] P. Grassberger, R. Hegger, H. Kantz, C. Schaffrath, and T. Schreiber. On noise reduction methods for chaotic data. *CHAOS*, 3:127, 1993.
- [109] J. Sun, Y. Zhao, J. Zhang, X. Luo, and M. Small. Reducing colored noise for chaotic time series in the local phase space. *Phys. Rev. E*, 76(2):026211, 2007.
- [110] D. Vakman. Computer measuring of frequency stability and the analytic signal. *IEEE Trans. Instrum. Meas.*, 43(4):668, 1994.
- [111] J. Sun, J. Zhang, J. Zhou, X. Xu, and M. Small. Detecting phase synchronization in noisy data from coupled chaotic oscillators. *Phys. Rev. E*, 77(4):046213, 2008.
- [112] M. Winterhalder, B. Schelter, J. Kurths, A. Schulze-Bonhage, and J. Timmer. Sensitivity and specificity of coherence and phase synchronization analysis. *Phys. Lett. A*, 356:26–34, Jul 2006.
- [113] T. Pereira, M. S. Baptista, and J. Kurths. Phase and average period of chaotic oscillators. *Phys. Lett. A*, 362:159–165, Feb 2007.
- [114] P. J. Loughlin. Spectrographic measurement of instantaneous frequency and the time-dependent weighted average instantaneous frequency. *J. Acoust. Soc. Am.*, 105(1):264–274, 1999.
- [115] P. M. Oliveira and V. Barroso. Definitions of instantaneous frequency under physical constraints. *J. Franklin Institute*, 337(4):303–316, 2000.

- [116] G. V. Osipov, B. Hu, C. Zhou, M. V. Ivanchenko, and J. Kurths. Three types of transitions to phase synchronization in coupled chaotic oscillators. *Phys. Rev. Lett.*, 91(2):024101, Jul 2003.
- [117] B. Boashash. Estimating and interpreting the instantaneous frequency of a signal. i. fundamentals. *Proc. IEEE*, 80(4):520–538, Apr 1992.
- [118] J. Sun, N. Zheng, and M. Small. On the relationship between instantaneous frequencies and time-frequency analysis. *submitted*, 2008.
- [119] E. Bedrosian. A product theorem for hilbert transform. *Proc. IEEE*, 51:868–869, 1963.
- [120] A. H. Nuttall and E. Bedrosian. On the quadrature approximation to the hilbert transform of modulated signals. *Proc. IEEE*, 54(10):1458–1459, Oct 1966.
- [121] S. Mallat. *A wavelet tour of signal processing*. Academic Press, San Diego, USA, 1998.
- [122] A. Bruns. Fourier-, hilbert- and wavelet-based signal analysis: are they really different approaches? *J. Neurosci. Methods*, 137(2):321–332, 2004.
- [123] N. M. Blachman. A comparison of the informational capacities of amplitude- and phase-modulation communication systems. *Proc. IRE*, 41(6):748–759, Jun 1953.
- [124] B. C. Lovell and R. C. Williamson. The statistical performance of some instantaneous frequency estimators. *IEEE Trans. Signal Process.*, 40(7):1708–1723, Jul 1992.
- [125] W. R. Bennett. Methods of solving noise problems. *Proc. IRE*, 44(5):609–638, May 1956.
- [126] H. Hamdan. Characterizing and approximating infinite scale mixtures of normals. *Communications in Statistics: Theory and Methods*, 35:407, 2006.
- [127] C. Allefeld and J. Kurths. Testing for phase synchronization. *Int. J. Bifurcat. Chaos*, 10(2):405–416, 2004.

- [128] W. A. Gardner. A unifying view of coherence in signal processing. *Signal Process.*, 29(2):113–140, 1992.
- [129] P. Fries, D. Nikolić, and W. Singer. The gamma cycle. *Trends Neurosci.*, 30(7):309–316, July 2007.
- [130] O. Jensen, J. Kaiser, and J.-P. Lachaux. Human gamma-frequency oscillations associated with attention and memory. *Trends Neurosci.*, 30(7):317–324, July 2007.
- [131] M. Thiel, M. C. Romano, J. Kurths, M. Rolfs, and R. Kliegl. Twin surrogates to test for complex synchronisation. *Europhys. Lett.*, 75(4):535–541, Aug 2006.
- [132] M. Kamiski, M. Ding, W. A. Truccolo, and S. L. Bressler. Evaluating causal relations in neural systems: granger causality, directed transfer function and statistical assessment of significance. *Biological Cybernetics*, 85:145–157, 2001.
- [133] M. Dhamala, G. Rangarajan, and M. Ding. Estimating granger causality from fourier and wavelet transforms of time series data. *Phys. Rev. Lett.*, 100(1):018701, 2008.
- [134] Y. Chen, G. Rangarajan, J. Feng, and M. Ding. Analyzing multiple nonlinear time series with extended Granger causality. *Phys. Lett. A*, 324:26–35, Apr 2004.
- [135] B. Schelter, M. Winterhalder, R. Dahlhaus, J. Kurths, and J. Timmer. Partial phase synchronization for multivariate synchronizing systems. *Phys. Rev. Lett.*, 96(20):208103, 2006.
- [136] S. Frenzel and B. Pompe. Partial mutual information for coupling analysis of multivariate time series. *Phys. Rev. Lett.*, 99(20):204101, 2007.
- [137] A. Bahraminasab, F. Ghasemi, A. Stefanovska, P. V. E. McClintock, and H. Kantz. Direction of coupling from phases of interacting oscillators: A permutation information approach. *Phys. Rev. Lett.*, 100(8):084101, 2008.

- [138] G. Nolte, A. Ziehe, V. V. Nikulin, A. Schlögl, N. Krämer, T. Brismar, and K.-R. Müller. Robustly estimating the flow direction of information in complex physical systems. *Phys. Rev. Lett.*, 100(23):234101, 2008.
- [139] C. Carmeli, M. G. Knyazeva, G. M. Innocenti, and O. De Feo. Assessment of eeg synchronization based on state-space analysis. *NeuroImage*, 25(2):339–354, 2005.
- [140] X. Li, D. Cui, P. Jiruska, J. E. Fox, X. Yao, and J. G. R. Jefferys. Synchronization Measurement of Multiple Neuronal Populations. *J. Neurophysiol*, 98(6):3341–3348, 2007.
- [141] F. Varela, J. P. Lachaux, E. Rodriguez, and J. Martinerie. The brainweb: phase synchronization and large-scale integration. *Nat. Rev. Neurosci.*, 2(4):229–239, Apr 2001.
- [142] K. A. Schindler, S. Bialonski, M.-T. Horstmann, C. E. Elger, and K. Lehnertz. Evolving functional network properties and synchronizability during human epileptic seizures. *Chaos*, 18(3):033119, 2008.



# Index

- $\varepsilon$ -neighborhood, 11
  - covariance matrix, 15
  - neighbors, 11
- AR(3), 29
- AURORA, 42
- autocorrelation matrix, 18
  - autocorrelation, 17
- Bedrosian theorem, 90
- BT, Blackman-Tukey spectrum estimator, 16–18
  - principle component BT estimator, 18
- butterfly effect, 1
- ch.f., characteristic function, 95
- coherency function, 97
- correlation dimension, 2, 10
- delay coordinate vectors, *see* phase vectors
- DTFT, discrete-time Fourier transform, 16
- embedding dimension, 10
  - minimum embedding dimension, 10, 14
- evaluated measure, 41
- false-nearest neighbors, 10
- FFT, fast Fourier transform, 59
- Fourier transform, 16
- hidden frequency, 54
- Hilbert transform, 22
- IA, instantaneous amplitude, 21
- instantaneous amplitude, 3
- instantaneous frequency, 4
- IP, instantaneous phase, 3
- iSNR, instantaneous signal-to-noise ratio, 94
- linSS, linear subspace method, 41
- local projection, 13
  - local subspace, 13
- locally linear model, 14
- logMMSE, log-spectral amplitude minimum mean square error estimator, 41
- Lorenz system, 1
- LP, the local projection method, 2, 26
- Lyapunov exponents, 1
- main frequency, 54
- MPC, mean phase coherence, 23, 95
- noise dominate subspace, 30
- noise subspace, 14, 26
- NSE, neighborhood-based phase estimation, 69, 70

- NSE, neighborhood-based spectrum estimator, 53
- P-BP, 79
- P-HT, 73
- P-LP, 73
- P-PP, 80
- pdf, probability density function, 95
- periodogram, 17, 54
- PESQ, 41
- phase points, *see* phase vectors
- phase portrait, 10, 11
- phase slip, 4, 68
- phase vectors, 10
- recurrence plot, 12
  - recurrence quantification analysis, 12
- resolution:computational resolution, 59
- resolution:physical resolution, 58
- ridge pattern, 3
- rms, root-mean-square, 94
- segSNR, segmental SNR, 41
- SI, synchronization index, 74
- signal subspace, 14, 26
- SMN, scale mixture of normal distributions, 95
- SNR, signal-to-noise ratio, 30
- spectral analysis, 3
- spectrogram, 19, 54
- state recurrence, 1, 11
  - Poincaré's recurrence theorem, 11
  - recurrence time, 12
- STFT, short-time Fourier transform, 19
- synchronization
  - chaos synchronization, 3
  - CS, complete synchronization, 20
  - GS, generalized synchronization, 21
  - LS, lag synchronization, 21
  - PS, phase synchronization, 3, 21
    - $l:m$  phase synchronization, 21
  - SI, synchronization index, 4
  - synchronization measure, *see* SI
- synchronization analysis, 3
- Takens' embedding theorem, 10
- time delay, 10
- time delay embedding, 2
  - over-embedding, 10
  - Takens' embedding theorem, 1
- time-frequency analysis, 3
- WN, wrapped normal distribution, 94